

Copyright
by
Navid Ghorashian
2013

The Dissertation Committee for Navid Ghorashian Certifies that this is the approved version of the following dissertation:

Automated Microfluidic Platforms to Facilitate Nerve Degeneration Studies
with *C. elegans*

Committee:

Adela Ben-Yakar, Supervisor

Jonathan T. Pierce-Shimomura

Xiaoqing Zhang

Konstantin V. Sokolov

Andrew K. Dunn

Automated Microfluidic Platforms to Facilitate Nerve Degeneration Studies
with *C. elegans*

by

Navid Ghorashian, B.A.; M.S.E.

DISSERTATION

Presented to the Faculty of the Graduate School of

The University of Texas at Austin

in Partial Fulfillment

of the Requirements

for the Degree of

DOCTOR OF PHILOSOPHY

THE UNIVERSITY OF TEXAS AT AUSTIN

DECEMBER 2013

Acknowledgements

Dr. Adela Ben-Yakar of the University of Texas at Austin has brought me into her group with open arms, and has allowed me pursue a wide breath of my scientific interests in the project described here. Her passion and enthusiasm for multidisciplinary research has been infectious, and I thank her for her continued support and guidance. Dr. Massimo Hilliard of the Queensland Brain Institute and Dr. Jon Pierce-Shimomura at UT Austin have also been very helpful in my understanding of *C. elegans* neurobiology and have been very generous with their time and mentorship. I would also like to thank Dr. Frank Werblin at UC Berkeley for giving me my first research position as an undergrad and allowing me to learn first-hand what rigorous scientific research demands. Dr. Luke P. Lee of UC Berkeley introduced me to microfluidics and gave me the opportunity to develop confidence in my creativity and passion for research. My fellow lab members, past and present, have been instrumental to the progress of this project and are all excellent human beings. My family has been instrumental in my life in ways that cannot be described, and it is apparent to me that I would have never made it to this point without them.

AUTOMATED MICROFLUIDIC PLATFORMS TO FACILITATE
NERVE DEGENERATION STUDIES WITH *C. ELEGANS*

Publication No. _____

Navid Ghorashian, Ph.D.

The University of Texas at Austin, 2013

Supervisor: Adela Ben-Yakar

With its well-characterized genome, simple anatomy, and vast array of uses in molecular biology, the roundworm, *Caenorhabditis elegans* (*C. elegans*) is a well-established model organism in neurobiology. Concurrently, neurodegenerative diseases are some of the most devastating and least understood ailments in modern medicine, making high-throughput approaches to understand their fundamental mechanisms imperative to developing new therapies. The worm's physical length-scales and simple genetics make it an ideal *in vivo* tool for high-throughput screening platforms. Concurrently, microfluidic technology has been used to make devices that manipulate these animals in a multitude of fashions to study various biological phenomena.

With these considerations in mind, we have developed microfluidic platforms to facilitate optical interrogation of neurodegenerative and neuroregenerative phenomena in *C. elegans* for large-scale screens. First we developed a multiwell format device with 16 on-chip reservoirs to house and quickly deliver distinct worm populations to any liquid-format imaging platform. The system achieved unprecedented delivery speeds, avoided any population cross-contamination, and maintained animal viability. We then expanded this platform into a 64-well device that acted as a modular plug and play system for simple manipulation by conventional high-throughput liquid handling systems. The chip could be manipulated in the same fashion as a multiwell plate and interfaced with a novel pneumatic gasket system to achieve delivery speeds that were two-fold faster than those attained on the 16-well device.

In addition, we worked to develop potential optical interrogation platform that could be fed populations of worms by the aforementioned delivery systems. This microfluidic chip consisted of an array of parallel traps to house individual worms over long durations for time-lapse studies of nerve regeneration after cuts to single axons mediated by a femtosecond pulse laser. Specifically, the platform was designed for regeneration studies in the *C. elegans* PQR neuron.

Table of Contents

List of Tables	xii
List of Figures	xiii
CHAPTER ONE: INTRODUCTION.....	1
1.1 Dissertation overview	1
CHAPTER TWO: BACKGROUND.....	4
2.1 Overall motivation	5
2.2 Caenorhabditis elegans as a model of neurological disease	6
2.2.1 C. elegans culturing techniques	8
2.2.2 C. elegans as a drug-screening model in neurodegenerative disease.....	9
2.3 High-throughput imaging tools for c. elegans biology	10
2.3.1 Automated C. elegans imaging platforms.....	11
2.4 Microfluidics.....	14
2.4.1 Microfluidic device fabrication.....	14
2.4.2 Microfluidic flow control and valve multiplexing with nematodes.....	16
2.4.3 Fluid dynamic modeling in microfluidics.....	17
2.4.4 Well plate-based microfluidics	21
2.5 Femtosecond laser-mediated nanoaxotomy	23

2.5.1 Background on nonlinear laser ablation	24
2.5.2 Microfluidic worm immobilization platforms	26
2.5.3 PQR neuron.....	30
CHAPTER THREE: AN AUTOMATED SIXTEEN-WELL MICROFLUIDIC	
POPULATION DELIVERY DEVICE FOR C. ELEGANS TRANSPORT	33
3.1 Overview.....	35
3.2 Design and testing.....	36
3.2.1 Design considerations	36
3.2.2. On-chip conical wells for simple sample loading.....	39
3.2.3 Design solutions to prevent population cross-contamination	41
3.2.3.1 Channel architecture solutions to improve segregation	42
3.2.3.2 Automation sequence solutions to improve segregation	43
3.2.4 Automated and fast worm population delivery.....	46
3.2.4.1 Flow rates through individual well channels	46
3.2.4.2 The automation sequence.....	48
3.2.4.3 Timing optimization.....	50
3.2.4.4 Fast worm population delivery	51
3.2.4.5 Experimental validation of population segregation	53
3.2.5 Animal viability after delivery through the device	56

3.3 Materials and methods	58
3.3.1 Device fabrication	58
3.3.2 On-chip valve control	60
3.3.3 Device fluid priming	61
3.3.4 Measurement of fluid flow rates	62
3.3.5 Worm culture techniques	62
3.3.6. Worm viability	64
3.4. Conclusions	64
 CHAPTER FOUR: A PLUG AND PLAY SIXTY-FOUR WELL MICROFLUIDIC DELIVERY DEVICE FOR C. ELEGANS POPULATIONS	
4.1 Overview	67
4.2 Design and testing	69
4.2.1 The 64-well population delivery chip	69
4.2.1.1 Microfluidic chip well channel array and valve design	71
4.2.1.2 Well plate reservoir "all-stop" valve	73
4.2.1.3 Microfluidic device fabrication	73
4.2.2 Gasket system design considerations	76
4.2.2.1 Acrylic gasket component	77
4.2.2.2 The gasket clamp	80

4.2.3 Automated delivery system design	80
4.2.4 Flow rates.....	82
4.2.5 Automated delivery sequence	85
4.2.6 Ultra-fast worm population delivery.....	89
4.2.7 Experimental validation of population segregation	91
4.3. Materials and methods	95
4.3.1. Device fabrication.....	95
4.3.2 Gasket system fabrication	96
4.3.3 Automation software and hardware control.....	98
4.3.4 Device operation: priming, animal loading, and sequence initiation.....	98
4.4 Conclusions.....	99
CHAPTER FIVE: NOVEL PARALLELIZED MICROFLUIDIC DEVICES FOR C.	
ELEGANS NERVE REGENERATION STUDIES.....	101
5.1 Overview.....	102
5.2 Preliminary work	103
5.2.1 Parallel trapping microfluidic devices	103
5.2.1.1 Design #1: Microfluidic single-layer parallel trap device	104
5.2.1.2 Design #2: Membrane immobilization parallel trap device (Version 1)	105
5.2.1.3 Design #3: Membrane immobilization parallel trap device (Version 2)	107

5.2.2 Preliminary nerve regeneration studies in the PQR neuron.....	108
5.3 Design and testing.....	109
5.3.1 Device design rationale.....	111
5.3.2 Trap filling.....	111
5.3.3 Immobilization chambers.....	112
5.4 Conclusions.....	113
CHAPTER SIX: CONCLUSIONS AND FUTURE DIRECTIONS.....	115
References.....	118

LIST OF TABLES

Table 3.1: Timings for the automated delivery sequence applied to each well and device Truth table for delivery from <i>Well 1</i>	49
Table 3.2: Average animal lifespan (days) after delivery through the whole chip under different pressure conditions.....	58
Table 4.1: Valve regulation column groups.....	72
Table 4.2: Timings for the automated delivery sequence applied to each well and device truth table for delivery from <i>Well HI</i>	86

LIST OF FIGURES

Figure 2.1: <i>C. elegans</i> as a model for studying neurodegenerative disease	7
Figure 2.2: A schematic of the COPAS flow cell system.....	12
Figure 2.3: A binary microfluidic multiplexer.....	17
Figure 2.4: Fluidic circuit model.	18
Figure 2.5: Well plate format microfluidic cell culture platform	23
Figure 2.6: Absorption and ionization events that lead to ablation of tissue.....	25
Figure 2.7: Microfluidic lab-on-a-chip for imaging and laser nanoaxotomy of <i>C. elegans</i>	26
Figure 2.8: The PQR neuron.....	31
Figure 3.1: <i>Population Delivery Chip</i>	37
Figure 3.2: Device schematic cross section and a worm population in a well plate-format reservoir.	38
Figure 3.3: Description of the earlier generations of the <i>Population Delivery Chip</i> and the changes made to avoid population mixing.....	40
Figure 3.4: Unintended worm transport in the previous device iteration.	42
Figure 3.5: A mechanism for potential population mixing during a non-optimized automated delivery sequence.	45
Figure 3.6: Fluid flow rates as a function of applied pressure.....	47
Figure 3.7: Automated worm population delivery sequence	50
Figure 3.8: Worm population delivery as a function of applied pressure.....	52

Figure 3.9: Population mixing eliminated during automated delivery at 20 psi (~138 kPa).	55
Figure 3.10: Worm viability test.....	57
Figure 3.11: Fabrication of well plate reservoirs for the <i>Population Delivery Chip</i>	60
Figure 4.1: 64-well population delivery chip.....	70
Figure 4.2: Workflow for fabricating the 64-well device flow layer.....	74
Figure 4.3: 64-well population delivery chip gasket system.	77
Figure 4.4: Pneumatic on-chip valve actuation from the gasket system.....	79
Figure 4.5: Measured fluid flow rates as a function of applied gauge pressure at the gasket in four representative wells from the 64-well population delivery chip.....	83
Figure 4.6: Time of flight from four well entrances to the <i>Main Outlet</i> as a function of pressure applied at the gasket.	84
Figure 4.7: The automated delivery sequence for delivery from <i>Well H1</i>	87
Figure 4.8: Optimized delivery order for emptying all 64 wells in the microfluidic device.	88
Figure 4.9: Worm population delivery rates for four representative wells in the device.	91
Figure 4.10: Ultrafast worm population delivery.	92
Figure 4.11: Strain mixing experimental design.....	94
Figure 5.1: Three consecutive design iterations of parallel trap devices for housing, immobilization, and optical interrogation of <i>C. elegans</i> worms.....	104
Figure 5.2: Fourth generation parallel trap device for imaging, housing, and axotomy.	110
Figure 5.3: Loading sequence for the fourth generation parallel trap device.	112

Figure 5.4: Immobilization trap design variables. 113

CHAPTER ONE: INTRODUCTION

1.1 DISSERTATION OVERVIEW

The monetary burden of neurodegenerative diseases in the United States is in the range of \$317 billion annually, including healthcare costs, productivity losses, and additional governmental expenditures [1, 2]. These estimates are conservative and do not take into account the undue suffering and emotional burden on patients and their caregivers. With the general worldwide shift towards higher life expectancies, the prevalence of age-related neurological degeneration will only increase. Understanding the fundamental molecular basis of neurological disorders and identifying potential drug targets as quickly as possible would greatly hasten development of treatments for these diseases. Our lab has developed optical and microfluidic tools to enhance studies of neurodegenerative mechanisms in the roundworm, *Caenorhabditis elegans* (*C. elegans*).

C. elegans is an ideal model organism for high throughput in vivo studies of biomolecular phenomena due to its short life cycle, stereotyped neuroanatomy, fully sequenced genome, and facility of use with various molecular techniques. Additionally, since the body length scales of the *C. elegans* worms are in the range of microns to millimeters, the animals are easily manipulated in microfluidic devices. Microfluidic technology has simplified and enhanced automated liquid handling experiments in the biological and chemical sciences. Microfluidics has already enabled a vast array of interesting and important *C. elegans* neurobiology investigations [3]. With this in mind, we have designed, fabricated, and tested microfluidic devices to facilitate high-throughput processing and optical interrogation of neuroregenerative and

neurodegenerative phenomena in *C. elegans*. First, we developed an automated platform that achieved ultrafast delivery of several distinct *C. elegans* populations to a desired location (e.g. another imaging apparatus or microfluidic chip) from 16 easily-addressable well plate-format reservoirs. These wells were built into the chip and were pressurized by a custom built gasket. The device achieved a delivery time per population that was an order of magnitude faster than the most advanced commercial liquid-handling systems for small organism high-throughput transport. Then, we expanded on this work to create a scaled-up and more user-friendly version of this platform that could easily interface with automated plate-handling systems and be utilized in a wider set of research environments. This system comprised of a microfluidic chip, which now included 64 well plate format reservoirs, and a novel pneumatic gasket that eliminated the need for excessive tubing inputs that plugged into the chip and enabled modular handling and off-platform loading of the animal populations. The chip's larger channel cross-sections increased flow rates to the point that it could deliver each population in half the time achieved with the 16-well device.

Finally, we continued the development of a comprehensive microfluidic system for studying nerve regeneration via femtosecond laser-mediated nanosurgery on individual axons in *C. elegans*. This device served as an example of a downstream apparatus which could receive worm populations from the aforementioned population delivery systems. The microfluidic chip consisted of an array of traps arranged in parallel to receive several individual worms for long-term housing, immobilization, and precision nanoaxotomy. After the axons were cut, worms were housed on-chip for recovery, and

axon regeneration in response to various biological factors could be observed/recorded. We worked towards a device that could fill each trap with a single animal, immobilize them sufficiently to allow laser surgery with sub-micron resolution, house the animals during axon regeneration, and enable subsequent imaging of neuron morphologies. With the ability to handle each of the aforementioned steps of nerve regeneration studies, the device could greatly simplify the experimental workflow.

CHAPTER TWO: BACKGROUND

In this chapter we present an introduction to scientific and technological areas relevant to the work presented in this dissertation. We will discuss the biological relevance of the nematode, *Caenorhabditis elegans* (*C. elegans*) in studying neurological disease and injury and how it is amenable to high-throughput biology due to key characteristics of its size and molecular physiology. Then we will introduce the field of microfluidics and how this technology is enabling unprecedented capabilities and throughput in biological and chemical screens. Finally, we will discuss the development and implementation of laser nanosurgery with ultra-fast pulse lasers to cut individual axons and dissect their regenerative properties. These technologies coupled with the unmatched flexibility and facility of using *C. elegans* as a model organism will lead to significant progress in understanding the underlying molecular mechanisms of neurodegenerative disease.

2.1 OVERALL MOTIVATION

With the advent of modern molecular biology, a vast array of technologies have allowed for fast and comprehensive characterization of the fundamental molecular and genetic basis of different phenomena related to critical human diseases. The potential impact of understanding these mechanisms in relation to nerve regeneration and degeneration would have profound benefits for human health. Severe disorders of the central nervous system (e.g. Alzheimer's, Parkinson's, and Huntington's disease), as well as injuries (e.g. spinal cord damage and stroke) are some of the most devastating ailments known to modern medicine. A major step towards enhancing fundamental knowledge of these conditions would be to elucidate their pathology in well-understood in vivo systems that can be characterized comprehensively [4].

One such model organism is the roundworm *Caenorhabditis elegans* (*C. elegans*). This nematode is normally found growing in soil in all parts of the world across a vast range of ecological conditions. The worm's amenability to a vast array of molecular tools, nearly complete biological characterization, and simple cultivation requirements have led to unprecedentedly fast and comprehensive studies that were impossible with any other in vivo model [5, 6]. Fast generation times (three days between larval and adult stages) and simplified genetics allow the creation of mutant strains in a matter of weeks instead of months or years, which are timescales typical for more complex model organisms. Still, conventional tools, the desire to keep experimental approaches consistent between studies and research groups, and a lack of engineering expertise have encumbered the biological

sciences in terms of adopting new technology to fully benefit from the use of these simple organisms or other advantageous experimental models.

With the considerable time and resources needed for genome-wide studies of neurodegenerative diseases in mind, many have turned to microtechnology to provide tools to manipulate microscopic samples in unprecedented ways and increase the rate of research in order to perform larger studies. Specifically, the application of microfluidic engineering has yielded several new high-throughput biological assays [7]. Recent advances in microfabrication techniques vastly improved the speed, flexibility, and applicability of electronic devices by reducing the size and cost of complex electronic circuits. Microfluidics exploits these methods to make systems of microchannels that reduce the scale, cost, and processing time of manipulating chemical and biological samples. Several research groups mainly led by Quake *et al.* have made microfluidic devices consisting of intricate arrays of pressure-controlled valves for multiplex chemical and visual analysis of biological samples [8].

2.2 CAENORHABDITIS ELEGANS AS A MODEL OF NEUROLOGICAL DISEASE

Ongoing research with *C. elegans* has identified several genetic targets that have allowed the elucidation of many biomolecular phenomena related to neuronal development and neurodegenerative disease [9-12]. Using this nematode as a model organism makes these investigations feasible due to the worm's simplicity and biochemical similarity to mammals.

For instance, research focusing on *C. elegans* has aided in understanding pathogenesis of protein misfolding in neurodegeneration. The major neurodegenerative

diseases are all associated with abnormal protein folding and aggregation in the affected neurons of the central nervous system (CNS), which eventually malfunction and degenerate [9]. The molecular basis of these events is poorly understood. In the case of Huntington's disease, there is an inverse relationship between the length of glutamate chains in the mutated proteins and the age of onset of the disease but below a length of 42 glutamate residues, the mechanism and likelihood of developing the disease are unclear [13]. With this challenge in mind, researchers were able to transfect fluorescently tagged polyglutamine chains of various lengths into *C. elegans* body-wall muscle cells and observe the formation of protein aggregates and behavioral declines (Fig 2.1) [14]. This model served as a means to comprehensively probe the genetic basis of protein aggregation in Huntington's disease on a large scale.

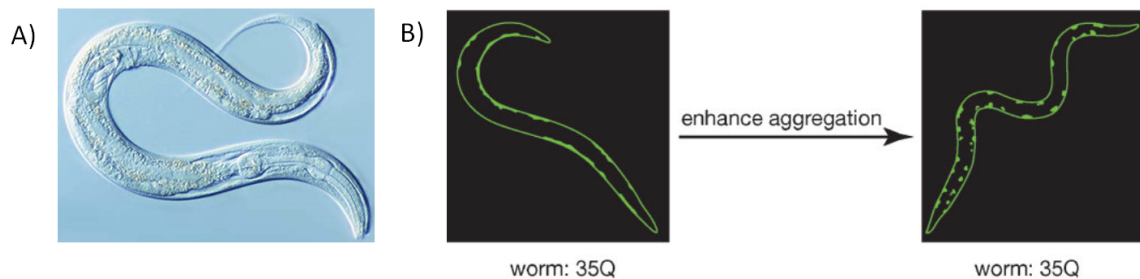


Figure 2.1: *C. elegans* as a model for studying neurodegenerative disease.

A) *C. elegans* has a nearly fully characterized genome and anatomy, and it is optically transparent. B) Fluorescently tagged proteins aggregate under specific genetic conditions in a Huntington's disease model [14].

In 2004, our group demonstrated that femtosecond (fs) pulsed lasers could be used to study nerve regeneration and development in *C. elegans*. We focused the fs-laser through a high-numerical-aperture microscope objective and precisely cut motor neuron

axons. This was followed by natural regeneration of the axons, including reconnection to the distal axon that was disconnected from the rest of the neuron by the cut [15]. The development of this technique spurred studies by many other research groups who used laser nanoaxotomy to discover genes regulating axonal regeneration in the motor and mechanosensory neurons [16-19].

For instance, Wu et al. found that the mechanosensory neuron, PLM (posterior lateral microtubule), regenerated and reconnected with far fewer anterior-posterior guidance errors when laser axotomy was performed in early larval stage *C. elegans*, as opposed to late larval and adult animals [16]. They also found that the VAB-1 Ephrin Tyrosine Kinase receptor may play a role in these guidance errors in adults. Gabel et al. demonstrated that proper axon guidance during regeneration was dependent upon the cytoplasmic protein MIG-10/Lamellipodin and regulators of actin cytoskeleton formation; UNC-34/Ena and CED-10/Rac [17]. In two more studies, the DLK-1 Map Kinase pathway was found to directly affect the development and proper regeneration following axotomy in both motor and mechanosensory neurons in *C. elegans* [18, 19]. Over-activity of this pathway leads to overgrowth of axons and synapse morphology defects, while laser-cut axons could not regenerate as efficiently as axons in wild-type animals if one of the genes in the pathway was missing.

2.2.1 *C. elegans* culturing techniques

The simplicity of cultivating and maintaining *C. elegans* is a key advantage in using this model organism to enhance research in the fundamentals of biomolecular phenomena. In fact, since its adoption by molecular biologists in the late 1960's, research

labs focused on this worm as a model organism have emerged all over the world. The benefits of using *C. elegans* to investigate biological phenomena have allowed the yearly publication rate of worm-related papers to double between the beginning and end of the previous decade [20].

Worms can be grown in non-sterile environments without the need for very stringent control of temperature, gas-composition, or humidity [21]. While tighter control of these parameters will tune animal viability, growth, behavior, and experimental outcomes to a finer degree, for many research groups it is sufficient to grow the animals at room temperature on the lab bench. Typically, researchers raise *C. elegans* on agar plates seeded with *E. coli* (*Escherichia coli*) bacteria, along with various salts and fatty acids for nutrition.

For liquid-based assays, *C. elegans* can be grown in liquid culture with bacteria with relative ease (S-medium) [21]. For larger screens, such suspensions have an advantage over the essentially two-dimensional culturing substrates on agar pads, since the three-dimensional liquid volume enables the cultivation of many more worms. Additionally, liquid culture is advantageous for high-throughput imaging systems for large-scale screens because the relevant devices generally receive the worms in suspended in fluid.

2.2.2 *C. elegans* as a drug-screening model in neurodegenerative disease

With knowledge of its fully sequenced genome (up to 60% homology with vertebrates) and easy cultivation in laboratory settings, *C. elegans* has become an emergent model for drug discovery related to human disease. Because much of the

molecular machinery responsible for certain disease is shared between the worm and humans, drug interactions can be predicted in worm assays [9]. Additionally, *C. elegans*' similarity to parasitic nematodes, which cause extensive harm to infected humans and devastate food supplies in resource-poor settings, makes it an ideal organism to characterize nematode biology and develop anti-parasitic treatment strategies [22].

More than a dozen genetic markers directly related to human disease, including genes relevant to neurological diseases, diabetes, and muscular dystrophy, have been extensively studied in *C. elegans* for drug discovery purposes [9]. For instance, the pharmaceutical company, Pfizer Inc. used *C. elegans* to screen 10,000 compounds to find suppressors of egg-laying defects linked to genetic mutations (*sel-12* and *egl-36*) that were orthologous to human Alzheimer's genes [10].

Several anti-parasitic compounds used to treat nematode infections in humans and kill agricultural pests were poorly understood until screens with *C. elegans* revealed genes in relevant neurotransmitter synthesis and processing pathways [11]. In particular, the studies elucidated factors involved in proper synthesis and transport of nicotinic acetylcholine (nACh) in neurons and their synapses. In some cases the mutations to some of these genes conferred resistance to therapeutic compounds. Such knowledge could help develop more robust anti-parasitic treatments.

2.3 HIGH-THROUGHPUT IMAGING TOOLS FOR *C. ELEGANS* BIOLOGY

Thanks to their size, geometry, and habituation to liquid environments *C. elegans* are easily cultivated in well plates using robotic liquid-handling systems. These worms can be subsequently characterized in high-throughput optical sorting systems, such as

flow-cell imagers and microfluidic devices. Further advancements and automation in these devices will start revolutionizing drug discovery and high-throughput biology with this model organism, making it an *in vivo* model with which to investigate complex biological phenomena at speeds and scales only previously achieved with simpler *in vitro* models [23, 24]. Still these optical interrogation platforms face a significant time bottleneck in screens across huge numbers of distinct worm populations due to technical hurdles in the population delivery mechanism.

2.3.1 Automated *C. elegans* imaging platforms

The only commercially available optical sorting system for *C. elegans*, the COPAS Biosort, is a modified flow cytometer that can optically scan large populations of worms to generate large-scale biological data [25-27]. This system has been used widely to perform genetic screens where basic optical data could elucidate changes in gene expression to isolate mutants of interest or quantify spatiotemporal gene expression [28]. Optical density, particle size, and one-dimensional multichannel fluorescence can be measured on 100 animals each second (Fig 2.2). With this technology, Doitsidou et al. quantified overall GFP expression from dopaminergic neurons in a forward screen for genes that modify how these neurons develop throughout the worm body [29]. Though the sensitivity of this approach was lower than typical fluorescence microscopy-based approaches, the sheer number of animals screened per unit time on the COPAS system allowed the experimenters to identify mutants nearly seven times faster than subjective visual assessments. Another group used the COPAS Biosort to generate data correlating developmental life stage with spatiotemporal gene expression along the worms' anterior-

posterior body axis using different GFP-tagged promoters [27]. They looked at thousands of animals to understand the interactions between ~900 genes related to basic physiological processes in the worm.

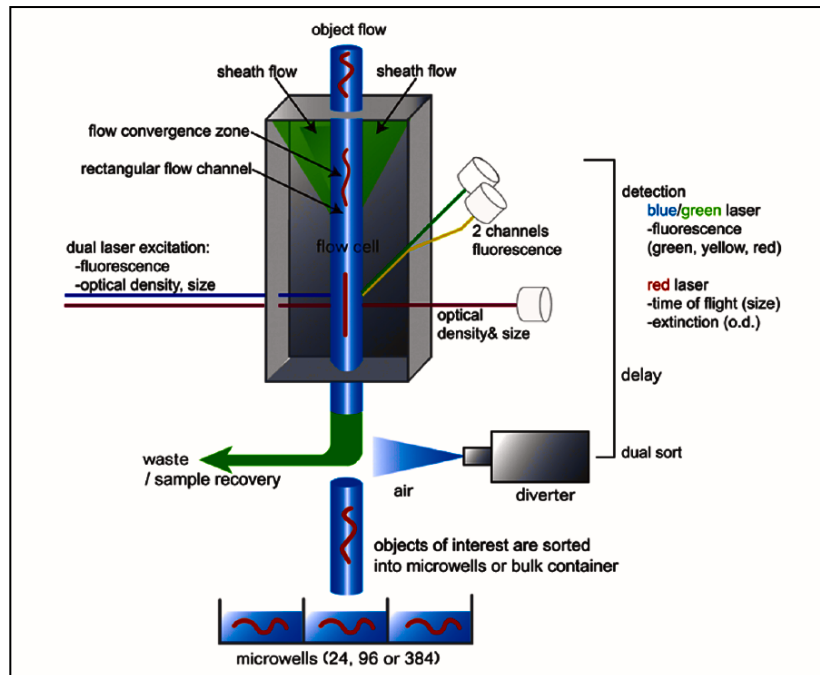


Figure 2.2: A schematic of the COPAS flow cell system.

The individual *C. elegans* worms (orange) are directed into the imaging flow cell where optical density, body length, and overall multi-channel fluorescence can be characterized and this information can be used to sort the animals in real time [28].

Before being sent to the COPAS system's optical elements, worms are housed in one large suspension or as separate populations in the reservoirs of a well plate. For screens with many distinct populations, the system also utilizes mechanical suction through tubing to transport the organism populations from well plates to the imaging hardware, and this delivery lasts ~45 sec/population. This timing is necessary to remove

the bubbles introduced to the sample during the tubing's periodic exposure to air. Bubbles can obstruct the field of view for imaging and generate artifacts in high-throughput data collection. Bubble-removal leads to a sample delivery time that is more than forty-fold longer than the imaging and sorting steps. A significant reduction in the time needed for bubble-free delivery for each population would dramatically shorten the duration of large-scale drug screens.

While capable of obtaining optical information a large number of worms in a very short time period, the COPAS system does not offer the high-resolution capabilities needed to obtain detailed information or precisely perturb the animals in a high-throughput fashion. Several research labs, including our own group, have been developing optical imaging and manipulation platforms for *C. elegans* bioassays with microfluidic approaches [3, 30-47]. These devices are generally designed in serial or parallel formats. In the parallel platforms, multiple animals can be housed and monitored simultaneously for analysis of development and life span [32, 39, 40, 43]. Serial loading chips transport and process the animals one-by-one for high resolution imaging, sorting, or optical manipulation [33-37, 41]. Using fluorescence microscope, Chung *et al.* developed a serial-processing microfluidic device that had one imaging channel receiving a single worm every few seconds [37]. The device platform utilized image processing algorithms to sort hundreds of animals per hour based on thresholds of fluorescence intensity in chemosensory neurons influenced by different genetic backgrounds. The same research group later adapted a similar platform with automated machine-learning

algorithms and image processing to tease out hard-to-detect changes synapse formation automatically [46].

In these microfluidic devices, sample populations are manually loaded with syringes. While this approach is simple and requires no special equipment, it can be very cumbersome and slow (up to ~15 min) [32]. Syringes need milliliter volumes to address the nanoliter-scales of microfluidic devices without introducing bubbles. This requirement could lead to excess use of precious reagents and drain effort and resources to prepare additional animals for screens. Researchers have used a mechanical suction method analogous to the COPAS system's delivery mechanism to transport *C. elegans* from well plates to a microfluidic device built for laser axotomies [41]. They frequently observed bubble and debris contamination, necessitating an additional on-chip washing step before each worm surgery.

2.4 MICROFLUIDICS

Microfluidics has become a ubiquitous tool in the chemical and life sciences over the last two decades, enabling automated manipulation of liquid samples at micron to nanometer length scales with unprecedented precision and throughput. The integration of these devices in various laboratory settings is enabling high-content experimentation in a repeatable and quantitative manner in areas of molecular biology, chemistry, and medicine that previously more qualitative [48].

2.4.1 Microfluidic device fabrication

Early development of microfluidic devices focused on chips made from glass or silicon. Typically, chemical wet etching or reactive ion etching (RIE) tools created

channels of varying geometries in the substrate of choice for mostly chemical analysis applications. These etching processes were both time consuming and resource intensive due to the need to perform lithography and etching with advanced machinery and harsh chemicals for every batch of devices made [49].

The pitfalls of fabrication yield and effort from using glass and silicon as a microfluidic substrate were overcome by a replica-molding approach pioneered by George Whitesides's group in the early 1990's [48]. This technique became known as soft lithography and is now the most common fabrication method used to make microfluidic devices. This approach allows for the creation of micron-scale channels of arbitrary dimension and design on biocompatible substrates for specialized applications in biological research.

Typically, a pattern defined on a photolithographic mask is used to generate a pattern on a photosensitive material (photoresist) that has been spin-coated onto a silicon wafer surface. The photoresist serves as the mold for an elastomer (e.g. polydimethylsiloxane, PDMS) that is poured onto the wafer. The elastomer is then cured and removed from the wafer, and the hardened piece bonds to a substrate, such as glass, silicon, or another piece of PDMS. The indentations left in the elastomer by the photoresist mold essentially become micron-scale fluid channels sealed from the external environment by the substrate bonded to the bottom of the new device or "microfluidic chip".

Stephen Quake's group developed a method to fabricate two-layer microfluidic chips with unprecedented complexity and functionality, owed mainly to the integration of

fully sealing on/off valves built into the devices [50, 51]. At least two photoresist molds are needed to fabricate these chips. For the bottom layer, PDMS elastomer is spin-coated across the mold so that a 20-30 μm layer rests above the photoresist features. The channels in this layer will serve as pneumatic inputs for the valve or membrane components of the chip. After the PDMS has hardened, the top layer of the device, which is usually fabricated as its own single layer in the typical fashion mentioned earlier, is bonded to the bottom layer. The top layer usually houses the biological samples (*C. elegans* worms in our case). Both layers are then removed as one piece, which has fluidic access holes drilled into it. Finally, the entire two-layer elastomer chip is bonded to a glass piece whose specifications match relevant optical system parameters.

2.4.2 Microfluidic flow control and valve multiplexing with nematodes

Valve multiplexing enables exponentially complex function with relatively few pneumatic inputs, leading to increasingly smaller and expansively functional devices. For example, binary multiplexers (Fig 2.3) can regulate “ n ” separate sample channels with $2 \times \log_2(n)$ pneumatic microfluidic control valves (e.g. 20 valves regulate 1024 samples) [51], and another combinatorial multiplexer scheme is even more efficient and uses “ N ” control valves to regulate $N!/(N/2)!$ individual sample channels (e.g. 20 valves control 184,756 samples) [52]. To date, microfluidic devices with multiplexed valve control are predominantly designed for handling liquid compounds in chemical, biochemical, and cell-based studies [50-56]. However, such samples behave more predictably in these devices than freely moving worms or other small organisms. Recently, it was suggested that a microfluidic multiplexer could deliver chemical compounds from standard well

plates to multiple *C. elegans* populations inside the device [41]. Yet, a microfluidic platform that could handle and transport multiple live populations of large-sized microorganisms (e.g. cell clusters, nematodes, drosophila and zebrafish larvae) has never been demonstrated. Such a device would need to address the complications of repeatedly transporting populations of motile multicellular organisms in microfluidic channels, preferably without harmful anesthetics.

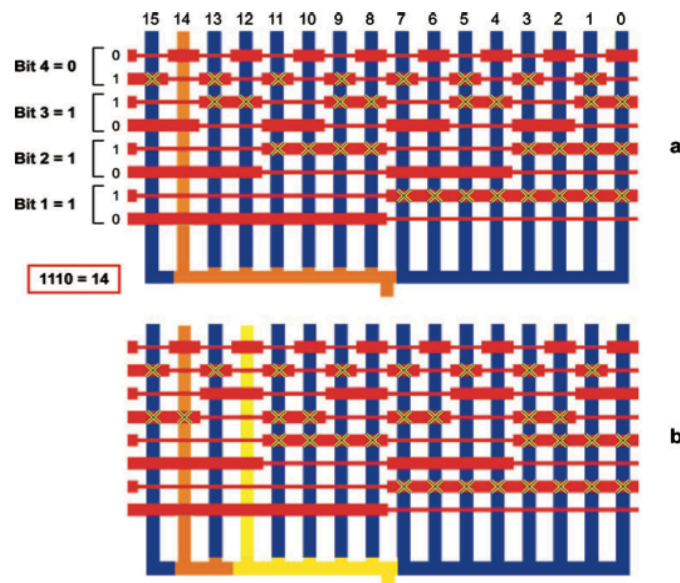


Figure 2.3: A binary microfluidic multiplexer.

Here ' n ' samples are regulated by $2 \times \log_2(n)$ control valves [53]. A) The orange sample is delivered to the common outlet by opening and closing a precise set of control valves. B) The yellow sample can be subsequently delivered by switching on/off positions between just two valves.

2.4.3 Fluid dynamic modeling in microfluidics

The development of microfluidic chips relies heavily on intuition and experience from testing and modifying the devices in conjunction with mathematical approaches

from fluid mechanics. The intuitive approach is used to develop the basic conceptual chip design, while mathematical methods help optimize fluid flow profiles and flow rates.

The process of calculating the essential fluid flow characteristics for microfluidic systems can be accomplished by reducing the system to a fluidic circuit, as illustrated in Figure 2.4 [57]. The bulk fluidic resistances of the major components are then calculated based on their geometries, followed by the pressure drop across each component. One can designate a given injection pressure from the fluid source based on pressures used experimentally and assume that the gauge pressure at the outlet is zero (atmospheric pressure). Once they find the pressure coming into the chip inlet, they can enter these parameters into a simple mathematical model to obtain expected flow rates and velocities within a given microfluidic design.

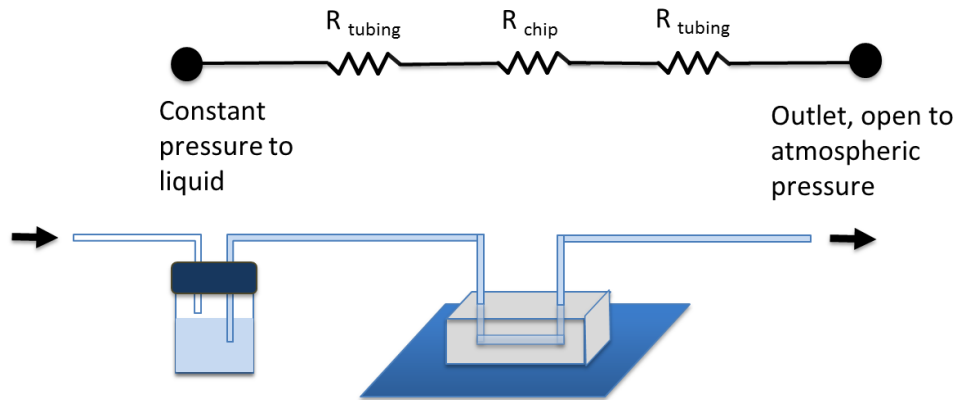


Figure 2.4: Fluidic circuit model.

Here is a basic fluidic circuit model of a microfluidic system with flow driven by a constant pressure source. R_{tubing} is the fluidic resistance of the tubing either before or after the chip and R_{chip} is the overall fluidic resistance of the microfluidic device. A fluid source under constant gauge pressure (known) is fed to the chip from tubing and then exits the chip through additional tubing to atmospheric pressure.

Reynolds number is another important fluid mechanics parameter to consider in the design of microfluidic channels. This value indicates the ratio of viscous and turbulent forces in the modeled fluid:

$$Re = \frac{d\rho u}{\mu} \quad (1)$$

Here d is the characteristic distance or diameter of the given tube, ρ is the density of the fluid, u is the fluid velocity, and μ is the viscosity. Higher Reynolds numbers indicate that turbulence and mixing will occur in the fluid, while lower values indicate that sheaths of fluid flow moving in parallel inside a microchannel will not mix or travel in directions counter to the main fluid flow vector. This lower regime is called laminar flow. Low Reynolds numbers are generally expected at microfluidic length scales and fluid velocities, so laminar flow profiles tend to dominate [58].

For the tubing connections, which externally interface into the microfluidic chips, the fluidic resistance can be estimated from the characteristic equations describing a fully developed laminar flow of Newtonian fluid in a circular tube:

$$R = \frac{128\mu L}{\pi d^4} \quad (2)$$

Here, L is the length of the tube and d is the diameter of the tube. The $1/d^4$ dependence of resistance on diameter makes even single order of magnitude differences in diameter lead to vast changes in resistance.

Fluidic resistance across the microfluidic channel is determined using an alternate method because microfluidic channels have rectangular cross-sections with dimensions

on the order of tens of microns. To get an analytical solution to the fluidic resistance of micro-channels, we used a solution of the Navier-Stokes equations for an isothermal, incompressible, isotropic liquid flow with no slip boundary conditions at the rectangular side-walls. Below is the final expression to estimate microfluidic resistance in a rectangular cross-section channel, which was described in [58]:

$$R = \frac{12\mu L}{wh^3} \left[1 - \frac{h}{w} \left(\frac{192}{\pi^5} \sum_{n=1,3,5}^{\infty} \frac{1}{n^5} \tanh\left(\frac{n\pi w}{2h}\right) \right) \right]^{-1} \quad (3)$$

Here w is the smaller dimension between the width and height of the rectangular channel, while h is the larger dimension. This equation holds true when the ratio of h to w is more than 2:1. Otherwise, other expressions of fluidic resistance may be used. All other variables are identical to their definitions in equations 1 and 2. For the devices discussed in this dissertation, calculations of the resistance of the tubing coupled to the devices were less than 0.1 % of the resistance of the entire chip due in large part to the relatively small cross-sectional dimensions the chip's microchannels.

With the characteristic flow rate of the system, we can next calculate the pressure drop after each resistance element in the system and then use this information to perform computational rendering of flow profiles in the actual microfluidic devices. These parameters are related to each other by the simple fluidic circuit model, where ΔP is the pressure drop, Q is the volumetric flow rate, and R is the fluidic resistance across a particular channel:

$$\Delta P = QR \quad (4)$$

When needed the microfluidic flow profile can be modeled in finite element multi-physics modeling software, such as COMSOL and Fluent. A microfluidic chip design can be imported into the software where different boundary conditions for flow rate, pressure, and viscosity are applied throughout the layout of the chip design. The software will numerically calculate the flow characteristics at each point in the device with the chosen parameters until it reaches a steady state.

In COMSOL one can model microfluidic fluid flow profiles by numerically by applying the Navier-Stokes equations for incompressible flow under steady state:

$$\begin{aligned} \nabla \cdot u &= 0 \\ -\nabla \cdot \mu(\nabla u + (\nabla u)^T) + \rho(u \cdot \nabla)u + \nabla p &= 0 \end{aligned} \quad (5)$$

Here u is the flow velocity vector (m/s), μ is the viscosity, ρ is density, and p is pressure. If the layout of the microfluidic channel design has any geometric symmetry, the portion of the channel that repeats along the symmetry plane is sufficient to calculate needed parameters. This approach drastically improves computational efficiency and duration.

2.4.4 Well plate-based microfluidics

At the level of internal device function, microfluidic technology enables fast and automated control of chemical and biological samples with unprecedented complexity

and precision. However, wide-spread adoption of microfluidics in relevant research areas has been slowed by the lack of a simplified interface between the macro-scale world and the micron-scale channels in these devices. Typically, several pneumatic and sample inputs on the chip must be coupled to individual syringes or pressurized sample reservoirs via tubing. Such an interface can be cumbersome and impractical, especially for labs without microfluidics expertise.

A few academic research groups and commercial entities developed well plate-based chips to facilitate delivery of samples to microfluidic channels where the chips' novel capabilities can be accessed [59-60]. Essentially, a well plate with bottomless reservoirs or machined access holes is bonded on top of a thin polymer microfluidic device layer such that each well plate reservoir is coupled to a single liquid-input site on the chip or array of chips. An example of a microfluidic well plate chip for mammalian cell culture and screening is shown in Figure 2.5 [59]. The plate-based chip array is fastened into a gasket systems or automated plate handling machine for pneumatic manipulation of chemical and biological samples. Typically, for each chip in the array, these devices have a single continuous microchannel layer with various inputs, and these units act as tissue culture bioreactors for different cell and tissue types.

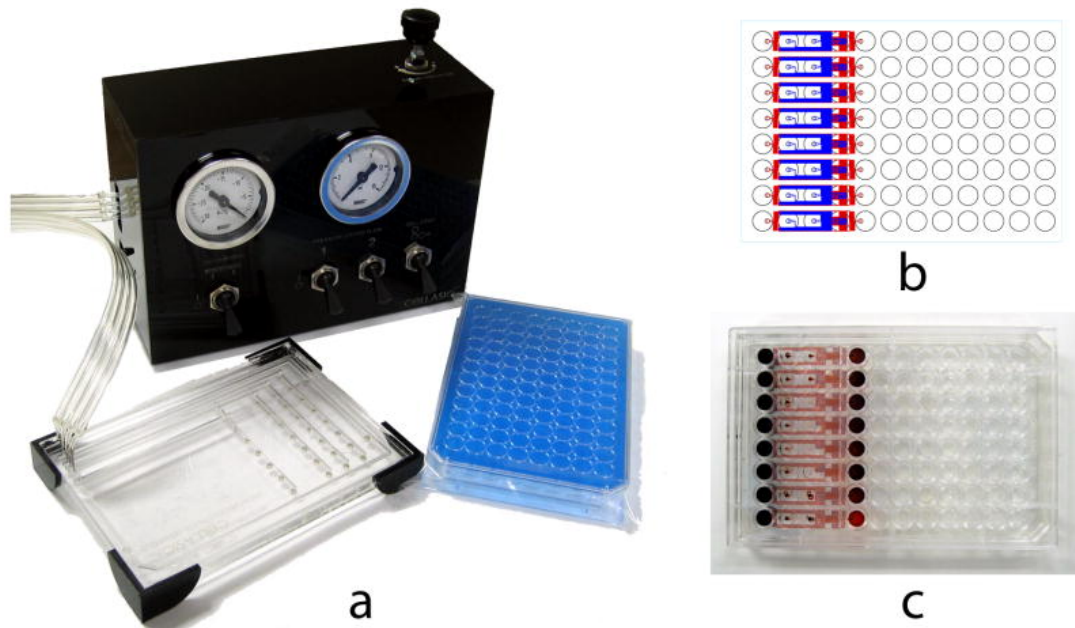


Figure 2.5: Well plate format microfluidic cell culture platform [58].

A) The system includes a pneumatic regulation system (black) coupled to a gasket that sits on top of the well plate format microfluidic chip. B) Schematic of the microchannels that interface with the well plate reservoirs. C) The actual device with microchannels loaded with food coloring dye.

2.5 FEMTOSECOND LASER-MEDIATED NANOAXOTOMY

As discussed earlier, our group performed the first targeted cuts of nerve axons in *C. elegans* using fs-laser pulses to ablate VD and DD motor neuron axons and observed their subsequent regeneration [15]. With this laser and the proper optical setup, one can ablate (photo-disrupt) femtoliter volumes with sub-micron spatial precision. The laser parameters lead to minimum damage to the surrounding tissue beyond the cut site because the time scale of plasma formation is too short for energy to transfer significantly beyond the focal point of the optical system [61].

2.5.1 Background on nonlinear laser ablation

Femtosecond laser pulses have been suggested as a precise ablation tool for living tissue owing to their high peak intensities and ability to generate plasma locally and efficiently, while still operating at low laser energies (nanjoule range). Previous neural ablation studies in *C. elegans* used nanosecond pulse ultraviolet lasers, which require microjoule energies to cause ablation and lack the sub-cellular precision seen with fs-lasers [62]. The higher energy pulsed lasers caused much more collateral damage to nearby tissue through thermal and mechanical processes. Alternatively, the ultra-short pulse durations and high photon flux of tightly focused fs-laser light are absorbed through non-linear processes, which result in very little damage to tissues outside of the focal volume.

Femtosecond laser ablation initiates through the absorption of photons in a condensed material (water, biological tissue, glass, etc.) followed by the freeing of electrons through multi-photon, tunneling, and avalanche ionization processes. Exponential growth of free electrons beyond the critical density leads to the generation of a high-density plasma within the confined focal volume [63]. This plasma expands radially, emitting a shockwave that causes damage in the form of high shear stress. The plasma becomes a cavitation bubble, which expands until the internal pressure can no longer resist surrounding water pressure and collapses. However, the gas generated can expand again due to fast confinement to a small volume, recreating the bubble.

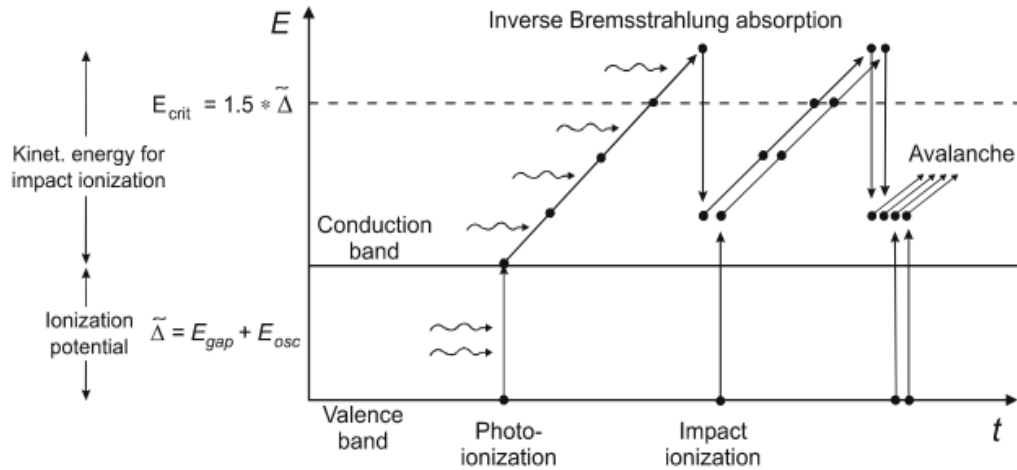


Figure 2.6: Absorption and ionization events that lead to ablation of tissue. The roles of different photoionization processes, such as multiphoton absorption, inverse Bremsstrahlung absorption, and impact ionization in free electron formation at the focal volume of the laser during nanoaxotomy [63].

Briefly, the ionization events that lead to optical breakdown and photo-damage occur as follows (Fig. 2.6). At the atomic level of the ablated material, multi-photon absorption by the electrons in the valence band excite these electrons to the higher-energy conduction band. After the electrons reach this state, several single photon absorption events in succession raise the electrons to an even higher energy state in a process known as ‘inverse Bremsstrahlung’ absorption. Then, one of these high-energy electrons collides with a conduction band electron with enough kinetic energy to excite it up to the valence band; a phenomenon known as impact ionization. The original colliding electron retains sufficient energy to remain in the conduction band. Each time this cycle repeats, impact ionization doubles the number of electrons in the conduction band. After several cycles, these events create an “avalanche” of free electrons in the focal volume that

outnumbers the free electron loss through diffusion and recombination. The energy generated by this process must also outweigh energy loss due to photon-to-large particle collisions that are asynchronous with photon absorption. When a critical density of electrons is freed at the focal spot, optical breakdown causes physical damage to the material [63].

2.5.2 Microfluidic worm immobilization platforms

Our lab applied advances in multi-layer PDMS microfluidic device fabrication to engineer a platform to study *C. elegans* worms at different phases of development between fs-laser nanoaxotomy and nerve regeneration imaging with conventional microscopy techniques [35].

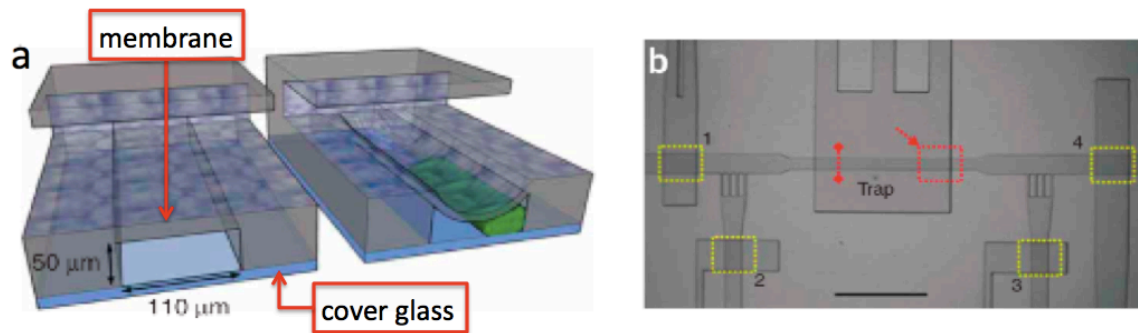


Figure 2.7: Microfluidic Lab-on-a-Chip for imaging and laser nanoaxotomy of *C. elegans*.

(a) Conceptual three-dimensional section renderings of the bilayer trap channels without and with a worm (green) immobilized by a membrane. (b) View of the trapping system: Valves 1–4 (yellow rectangles) respectively control inlet regulation (1), fine positioning of the worm (2 and 3) and gating to the recovery chambers (4) (SCALE BAR ~1 mm). [35]

As shown in Figure 2.7 we designed and fabricated a lab-on-chip platform in which single animals were loaded into a microfluidic channel either manually or with a syringe pump before entering the microfluidic immobilization trap, which was essentially a deformable membrane above the channel housing the worm [35]. When we wished to image or ablate axons, pressure was applied to the channel leading to the membrane. The membrane pressed the worm's body against the cover slip, which was bonded to the bottom of the device (Figure 2.7a). This orientation provided ideal optical access to neurons of interest. Off-chip controls were a set of computer-controlled solenoid valves and a syringe pump, which allowed automated control of fluid flow in the microchannels. Another group at MIT subsequently developed a similar device for performing fs-laser axotomy and two-photon imaging studies of nerve regeneration in *C. elegans* [34, 41].

With this membrane immobilization device, our lab studied nerve regeneration in *C. elegans* mechanosensory neurons (ALM, anterior lateral microtubule cell and PLM) and we found that axonal recovery time was greatly reduced (~60-90 minutes versus ~6-12 hours) when compared to experiments performed on agar with anesthetics [35]. These studies demonstrated the feasibility of performing laser axotomy on worms in a microfluidic device, while suggesting that the animals' regeneration capacity was more rapid in the absence of anesthetics.

This device established the necessary components to immobilize, image, and perform laser nanoaxotomy: a fluid channel with the proper dimensions to house a single worm and a deflectable membrane to precisely immobilize the animal for optical studies

[35]. The subsequent design question was to determine a mechanism to integrate these functional pieces into a high-throughput system that would enable the study of multiple animals (10's to 1000's) in a short period of time.

One solution to enabling high-throughput studies is serial automation. Precisely timed actuation of off-chip solenoid valves to activate on-chip membrane valves could control the transport of worms in a microfluidic channel such that a large number could be sequentially studied with the afore-mentioned optical methods. This “one-by-one” approach requires only one imaging and surgery staging area to receive single worms, which are subsequently transported to another location on-chip or to an external storage platform as the next worm arrives for imaging and surgery. One drawback for axotomy studies is that after surgery, the animals need to be moved to separate storage areas and then returned to the imaging channel after a given amount of time to observe regeneration. Automation of this kind of process could become very complex if large quantities of animals are being studied.

Another route to high-throughput studies of *C. elegans* worms on-chip is parallelization. In this approach the number of channels for immobilization, imaging, and surgery would be increased by one or more orders of magnitude in the device design and arranged in a parallel fluidic circuit. This way one could simultaneously load and house many worms in their own individual imaging and surgery chambers in a single chip. An advantage of parallelization versus the one-by-one approach is that with the proper design, the complexity of automation and time spent sorting and transporting animals through the device is greatly reduced. Additionally, the worms can remain housed in their

imaging and surgery chambers between observations. Housing the worms in parallel avoids repeatedly moving single worms out of the imaging and surgery portion of the chip for high-volume experiments. The primary disadvantage of this approach is that to study 100's or 1000's of worms, a large-area chip (several centimeters in diameter) or multiple chips to store the animals would be needed. Fabrication of large area microfluidic devices with two channel layers requires precise alignment of the valve control layer with respect to the fluid channel layer. Additionally, high-throughput studies would necessitate a motorized translation stage for optical observations of multiple chambers. This equipment is readily available for many standard optical setups.

A few groups have recently introduced simple microfluidic devices that utilize parallelization in their designs. A device made by Hulme *et al.* has a single inlet, which bifurcates seven times to create 2^7 (128) trapping channels that taper in width over a length of 5 mm from 100 microns to 10 microns [32]. Single animals get stuck in one of these tapering regions and block most of the flow through that particular channel, such that the likelihood of another worm entering that location is much lower than it following the upstream bifurcations to another open trapping channel. While the bifurcations limit worms from over-filling single channels, they necessitate a 15-20 minute loading time to fill the traps. Allen *et al.* developed a chip that consists of an array of tapering trapping channels in parallel placed downstream of a worm-loading inlet channel [64]. These five millimeter long trapping channels are 100 microns wide at their entrance and 8 microns at their opposite end, which is a small enough width to prevent the animals from squeezing through. A drawback to such long trapping channels is that multiple worms may fill a

single channel, which may create confusion in tracking individual specimens across multiple time points. Additionally, both of these devices require constant applied pressure to the inlet channel to guarantee long-term immobilization of animals.

A feasible approach to create a parallelized device to facilitate axotomy studies with *C. elegans* would be to place tapering channels just upstream of a larger housing chamber for each worm and arrange several of these hybrid structures in parallel to study a large number of animals. The worms would flow into the device, go through the housing chambers, block flow into the chambers by clogging the tapered channel, and then be released back into the housing chambers. The flow blockage that occurs when the worm is in the tapering channel would prevent more than one animal from entering each housing chamber so that individual worms could be tracked throughout an experiment.

2.5.3 PQR neuron

Studying nerve regeneration after axotomy in the PQR neuron could yield interesting insights into mechanisms of nerve repair. This neuron's cell body is located near the worm's tail and extends neural processes in two directions (Figure 2.8). The short process or "dendrite" extends out towards the tail and has no synapses or gap junctions, while the ventral cord process or "axon" extends toward the head along the ventral cord where it has multiple synapses. The primary purpose of this neuron is oxygen sensation inside the animal's coelomic body fluid cavity [65].

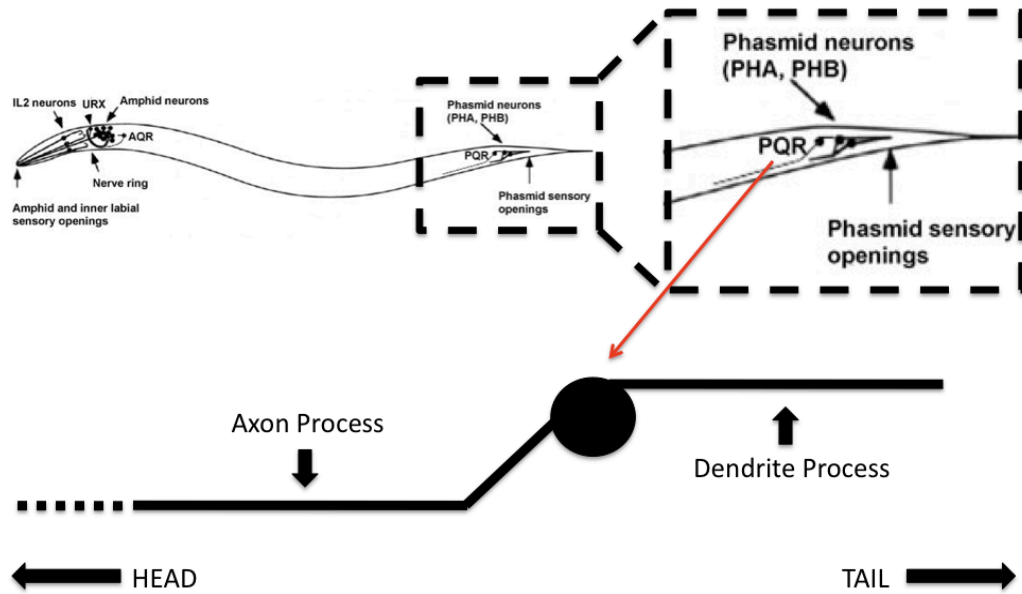


Figure 2.8: The PQR neuron.

This oxygen sensory neuron is located in the left lumbar ganglion on the posterior-lateral side of the body, and has two processes emerging from the cell body: a dendrite extending posterior toward the tip of the tail and an axon extending anterior joining the ventral nerve cord (the dotted line indicates that the axon continues towards the head for ~100-200 μm) [66].

Our preliminary studies indicate that fs-laser axotomy to the axon process of the PQR neuron yielded 100% regrowth along the previously established axonal trajectory 24 hours post laser cutting. Additionally, cuts to the dendritic process yielded 50% regrowth after 24 hrs. However, simultaneous cuts to both processes in the same neuron, yielded 100% regrowth in both processes, suggesting that regenerative cues are more active after cuts to the axon and these regenerative factors can increase the regenerative capacity of the dendrite. Since the process that grows anteriorly (axon) has a higher regenerative capacity, genes that specify the directions of axon and dendrite growth could be implicated in regeneration in the PQR neuron.

Previous findings have implicated the WNT/Frizzled genetic signaling pathway in anterior/posterior growth polarity defects in *C. elegans* mechanosensory neurons [67]. In regards the PQR neuron, it has been shown that mutations to the WNT ligand, *lin-44* can cause the dendrite to grow anteriorly [68]. A question arises in regard to whether the regenerative capacity of the axonal or dendritic processes remains unchanged after reversing neuronal polarity with specific WNT pathway mutations. If the answer is no, one might conclude that the factor(s) that give the PQR neuron's axon a higher regenerative capacity than the dendritic process are cell autonomous. However, if this regeneration were perturbed, localized extracellular cues may play a role in regeneration.

CHAPTER THREE: AN AUTOMATED SIXTEEN-WELL MICROFLUIDIC POPULATION DELIVERY DEVICE FOR *C. ELEGANS* TRANSPORT

Automated biosorter platforms, including recently developed microfluidic devices, enable and accelerate high-throughput and/or high-resolution bioassays on small animal models. However, time-consuming delivery of different organism populations to these systems introduces a major bottleneck to executing large-scale screens. Current population delivery strategies rely on suction from conventional well plates through tubing periodically exposed to air, leading to certain disadvantages: 1) bubble introduction to the sample, interfering with analysis in the downstream system, 2) substantial time drain from added bubble-cleaning steps, and 3) the need for complex mechanical systems to manipulate well plate position. To address these concerns, we developed a multiwell-format microfluidic platform that can deliver multiple distinct animal populations from on-chip wells using multiplexed valve control. This *Population Delivery Chip* could operate autonomously as part of a relatively simple setup that did not require any of the major mechanical moving parts typical of plate-handling systems to address a given well. We demonstrated automatic serial delivery of 16 distinct *C. elegans* worm populations to a single outlet without introducing any bubbles, causing cross-contamination, or damaging the animals. The device achieved delivery of more than 90 % of the population preloaded into a given well in 4.7 seconds; an order of magnitude faster than delivery modalities in current use. This platform could potentially handle other similarly-sized model organisms, such as zebrafish and drosophila larvae or cellular

micro-colonies. The device's architecture and microchannel dimensions allow simple expansion for processing larger numbers of populations.

3.1 OVERVIEW

Biological screens, especially large-scale studies on automated fluid handling platforms (microfluidic devices, flow sorters), would be supremely enhanced by an ultra-fast delivery platform for receiving specific worm populations. Such a platform should easily interface micron-scale fluidic environments to the macro-world where worm populations are prepared with liquid-handling robotic systems. Furthermore, it should automatically deliver the populations without cross-mixing or adding bubbles. Microfluidics readily meets these criteria. The technology enables liquid-liquid connections between platforms without air exposure, reducing bubble contamination. These aspects are important for the stability of fluid flow profiles and error-free data collection. Additionally, built-in microfluidic valves controlled via multiplexing can streamline automated device functionality [51, 53].

Here we present a microfluidic system for ultra-rapid transportation of worm populations treated with different compounds from well plates to a given optical interrogation platform. This chapter describes the microfluidic multiplexer device, the *Population Delivery Chip* (Fig. 3.1), which can rapidly deliver 16 different worm populations to a desired location without cross-mixing or introducing any bubbles to the samples and does not affect the worms' viability. The platform is capable of delivering each population to a prescribed location in 4.7 seconds, a nearly ten-fold improvement over current platforms. The *Population Delivery Chip* has conical on-chip reservoirs arranged in a well plate format and spacing, making the device compatible with high-throughput robotic liquid-handling systems. In the following sections, we will present

device design considerations and optimization efforts of the microchannel geometries, valve architectures, well plate reservoir interface, and the automated population delivery sequence. With *C. elegans* as the experimental model, the system could significantly reduce the time needed for large-scale drug screens and enhance fluid-based assays for a variety of applications.

3.2 DESIGN AND TESTING

3.2.1 Design considerations

The design process for a microfluidic device for *C. elegans* population delivery requires addressing four major design considerations: 1) interfacing with well plate format reservoirs, 2) delivering multiple worm populations without cross-contamination, 3) achieving fast and repeatable worm population size delivery, and 4) hands-free automation within these constraints.

The design considerations culminated in a computer-controlled multiplexed microfluidic device with built-in conical wells for high-speed population loading. The device features an optimized microchannel/microvalve architecture, which facilitates the rapid (4.7 sec/well) and automated delivery of *C. elegans* populations from 16 wells without cross-contamination between populations.

Several design iterations led us to the two-layer microfluidic device presented in Figure 3.1. The general design includes the following main features: 1) integrated on-chip wells having dimensions consistent with the wells in traditional well plates for simple loading of worms into the chip using robotic liquid-handling systems, 2) a multiplexed pneumatic microfluidic valve system to control flow in microchannels emerging from

individual wells, 3) a staggered configuration of microchannels merging into the main delivery channel, and 4) two flush units with multiple control valves to accelerate delivery of each worm population to a location of interest and guarantee no animals remain in the device afterwards.

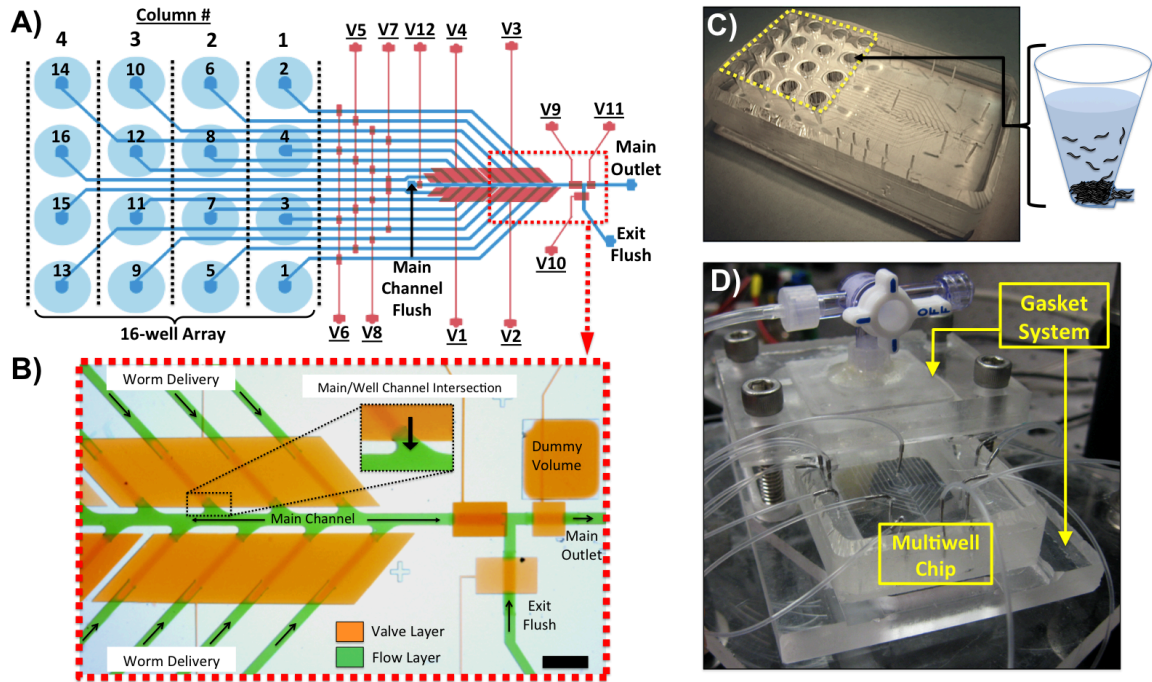


Figure 3.1: Population Delivery Chip

A) A schematic of the device indicating the flow layer (blue) and control valve layer (red). There are 16 on-chip wells arranged in a 96-well plate format for initial loading of different worm populations. Columns and wells of the array are numbered according to order of delivery. Valves $V1-V8$ are multiplexer control valves and $V9-V12$ control flow in the main channel. B) An image of the device with its microfluidic channels loaded with food coloring dye, showing the flow layer (green) and control valve layer (orange) (scale bar $\sim 1\text{mm}$). C) A macro-scale view of the device with the 16-well array indicated by the yellow dashed lines and a schematic of worms loaded into one of the conical wells. D) A macro-scale view of the entire chip/gasket system with pressurized input lines in the experimental setup.

The integration of wells into the chip substantially simplified the world-to-chip interface. The arrangement of valves near the main channel/well channel intersections, and two device-cleaning flush inlets acted together to prevent population mixing during automated delivery. An acrylic gasket sandwiched the chip to deliver pressurized air to on-chip well reservoirs. Microfluidic valves arranged according to the multiplexer control scheme regulated flow through the device's microchannels with a minimal number of valve inputs [53]. The automated delivery software allowed for flexible arrangement of valve actuation timings, which were optimized to prevent mixing between populations and achieve fast and nearly complete population delivery during device operation.

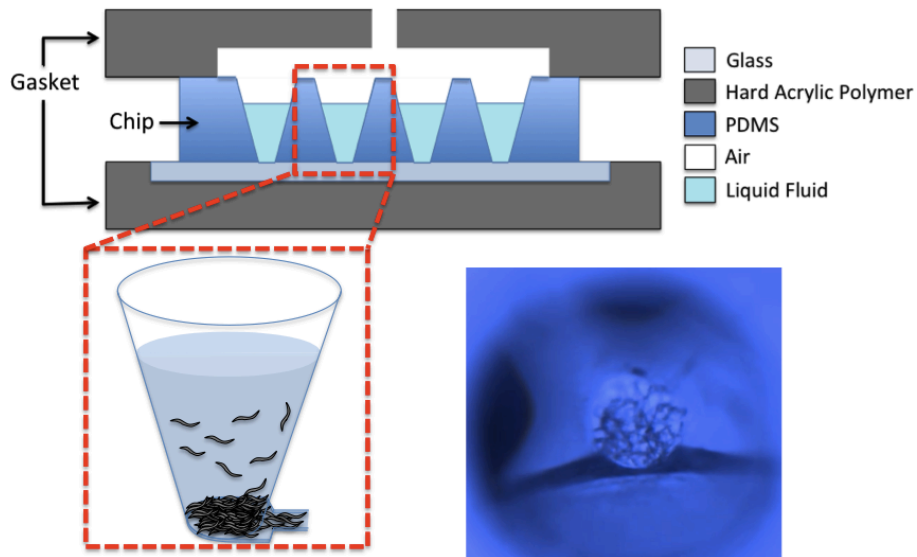


Figure 3.2: Device schematic cross section and a worm population in a well plate-format reservoir.

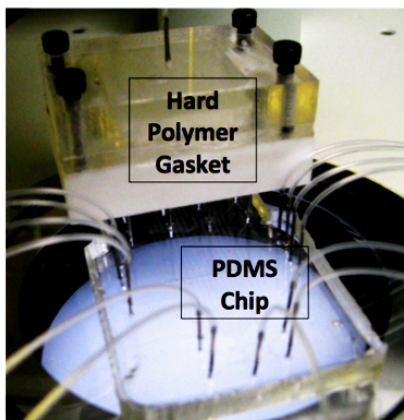
The schematic shows the relative position of the different device setup components. A schematic of a given well with worms loaded, as well as a top-down view photograph of worms in a well are also shown.

3.2.2. On-chip conical wells for simple sample loading

To address the first design consideration, we integrated an array of well plate reservoirs within the microfluidic device. A simple molding method enabled us to fabricate identical conical wells into the PDMS and directly connect them to the microchannels in the device (Fig. 3.11). The conical shape of the reservoirs enabled concentrating the animal population at the interface of the well-bottoms and microchannel entrances.

In our earlier approach we made an attempt to interface standard well plates with the microfluidic chip through an acrylic/fluoropolymer gasket (Fig. 3.3). However, that approach was prone to a few challenges. The wells interfaced with the chip through metal tubing sticking out of gasket's bottom side. Aligning all 16 metal tubes with 16 on-chip fluid ports was technically challenging and resulted in sample leakage between the metal tubing and the PDMS chip. Additionally, the population of animals could potentially accumulate in the gasket wells or in the metal tubing coupler, and cause contamination.

A) Earlier Generation



B) Final Generation

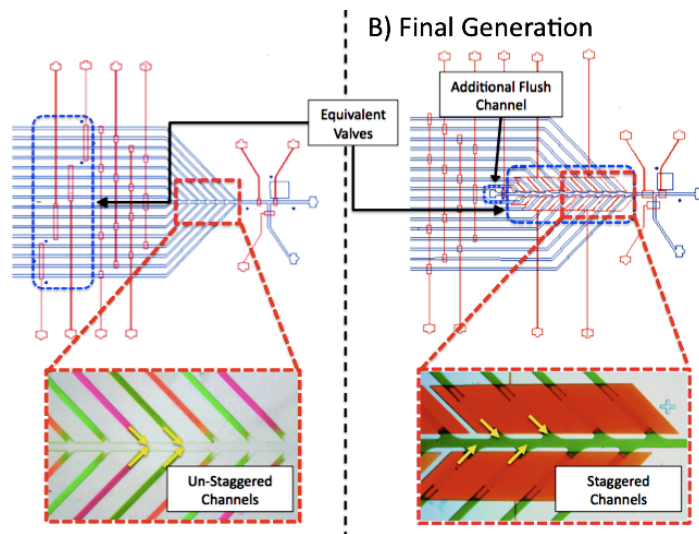


Figure 3.3: Description of the earlier generations of the *Population Delivery Chip* and the changes made to avoid population mixing.

A) Earlier generation device with macro-scale image of the polymer gasket and the PDMS chip. In this device samples were loaded in wells inside the white polymer gasket, which was sealed to an air pressure line. The bottom of each well linked to the microfluidic chip's inlets via metal couplers. Leakage at the metal coupler-polymer interface became problematic. B) Final generation device. For parts A and B of this figure, the blue dashed lines surround four equivalently functioning valves in both devices. The yellow arrows in the zoomed-in photos illustrate the difference between the well channel-main channel interfaces in the un-staggered and staggered well channel arrangements. In the earlier version, experiments with colored dyes revealed unintended flow between well channels, hinting at the potential for cross contamination between populations during automated delivery, which was later confirmed. The final generation showed similar potential for mixing in dye experiments, but the placement of valves near the main channel, the addition of the *Main Channel Flush*, and sequence optimization eliminated population mixing during delivery.

By integrating the wells directly into the multiplexer microfluidic chip, we could eliminate fluid leakage, simplify initial sample loading, and make the device more compatible with robotic liquid-handling systems (Figure 3.2). Most worms loaded in fluid suspension would sink and concentrate at the bottom of these conical wells in a couple of minutes; staging them at the well channel entrances before delivery. Having the

entire worm population placed at the channel entrance shortened the distance animals traveled on-chip and decreased the timing necessary to deliver a similar number of worms. Wells built into the chip streamlined device operation.

3.2.3 Design solutions to prevent population cross-contamination

Device architecture in relation to microchannel geometries and microfluidic valve location, along with the automated delivery sequence arrangement played major roles in the optimization of the *Population Delivery Chip's* ability to prevent population mixing during delivery. Occasional cross-contamination between populations within different well reservoirs occurred in our initial designs (Fig. 3.3a). Worms' unpredictable swimming behavior caused them to periodically deflect at the well/microchannel intersection with the main channel, occasionally directing the worms into other well channels, instead of allowing them to flow out of the *Main Exit* (Fig 3.4). These events could occur despite the fact that the device was directing flow from a single well to the outlet, and not towards the other well channels. We believe that the sharp corners at the diagonal intersections of the well channels and the main channel, and the fact that these intersections were arranged directly opposite of each other (un-staggered) were the two major contributors to cross-contamination. Considering these observations, we pursued a few design solutions that successfully prevented population cross-contamination.

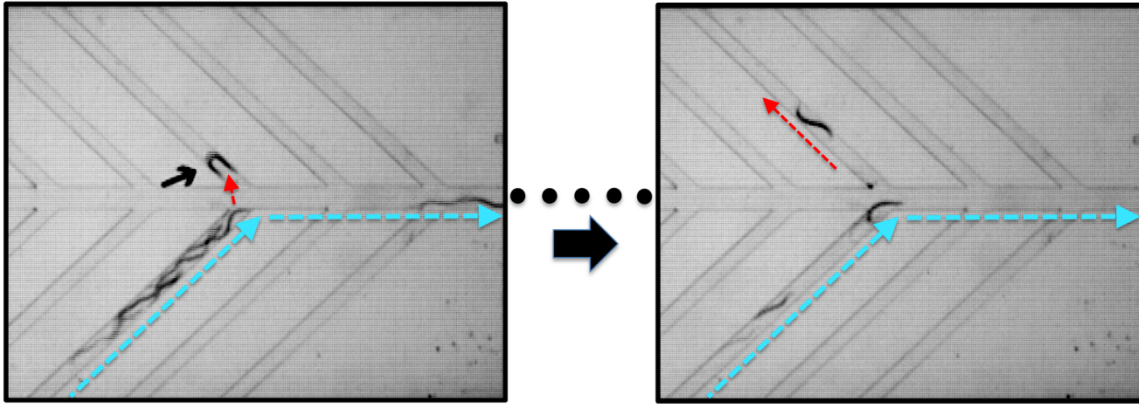


Figure 3.4: Unintended worm transport in the previous device iteration.

Two consecutive frames are shown from a video of the previous device in action. The blue arrow shows the direction of intended flow in the device as a population is delivered to the main channel. A single worm manages to swim from the bulk population into another well channel (red arrow) instead of the device exit.

3.2.3.1 Channel architecture solutions to improve segregation

We made four key changes to the channel design to prevent worm population cross-contamination between wells. First, we moved the large control valves from an upstream position close to the intersection of the well channels with the main channel (Fig. 3.3b). This design element prevented worms that were moving through main channel from unintentionally being transported into the well channels instead of to the exit. Second, we integrated a flush channel upstream of all of the main channel/well channel intersections to wash out remaining members of a sample population between delivering each population from different wells (Fig. 3.1a). Third, we rearranged the intersection of well channels with the main channel in a staggered pattern to ensure that the entrances of two well channels do not sit directly across from one another along the main channel. Finally, we rounded the sharp channel corners at the intersection of the

well channel and the main channel. By eliminating sharp-angled intersections, unpredictable worm movements around these corners were avoided. Automated operation of the final device showed no instances of worms accidentally flowing into another well channel.

3.2.3.2 Automation sequence solutions to improve segregation

Flow in each well-channel from a given well to the main channel, was regulated by an upstream (*V5-V8*) and a downstream valve (*V1-V4*). The sequence for delivery from different wells was chosen based on this valve configuration to prevent cross-mixing between the populations during delivery. Added channel cleaning steps acting together with this delivery sequence helped prevent population mixing as well.

First, we chose to deliver populations in groups of wells that share the same upstream valve (*V5-V8*). By positioning downstream valves close to the main channel, we successfully minimized dead volumes where possible mixing could occur. However, manipulation of freely moving, living organisms required additional attention. Worms could freely swim in the well-channels even if the flow was completely stopped by the upstream and downstream control valves. After transporting most of a given well's population to the desired location, a few worms could remain in the well channel. We therefore implemented a "flushback" or cleaning step to push any worms remaining in the well-channel back to their destination well, beyond the upstream valves. This step prevented them from escaping into the main channel during delivery from other wells with which they shared the same downstream valve (*V1-V4*). This washing step alone, however, was not sufficient if the order of wells was randomly chosen. Worms could

potentially swim past opened upstream valves even if the downstream valves regulating their well channels were closed. For example, delivery from *Well 7*, just after delivery from *Well 1* could cause the following complication: During population delivery from *Well 1*, *V6* needs to be opened, also allowing *Well 3*'s population to swim closer to *Well 3*'s downstream valve (*V1*). If we choose to deliver from *Well 7* next, its population could be cross-contaminated with worms from *Well 3* that slipped downstream of *V6* during delivery from *Well 1* (Fig. 3.5). Such events could only be avoided by applying an additional flushback step on *Well 3* before delivery from *Well 7*. However, we eliminated these types of complications by arranging the sequence such that wells regulated by the same upstream valve would deliver their worms in sequence, and then the sequence would clean their well-channels in a single step, as one group before proceeding to the next column of wells. For example, fluid flow from *Wells 1-4*, the first column of wells, is regulated by valve *V6*; therefore the optimized sequence delivered populations from *Wells 1-4* consecutively. Unloading wells in this fashion also minimized the number of washing sequences required. Specifically, after delivering all four of these populations, the automated program performed a single cleaning step to wash back any excess worms in the well-channels to their respective sample reservoirs. Cleaning steps did not need to be repeated on these wells since *V6* never reopens.

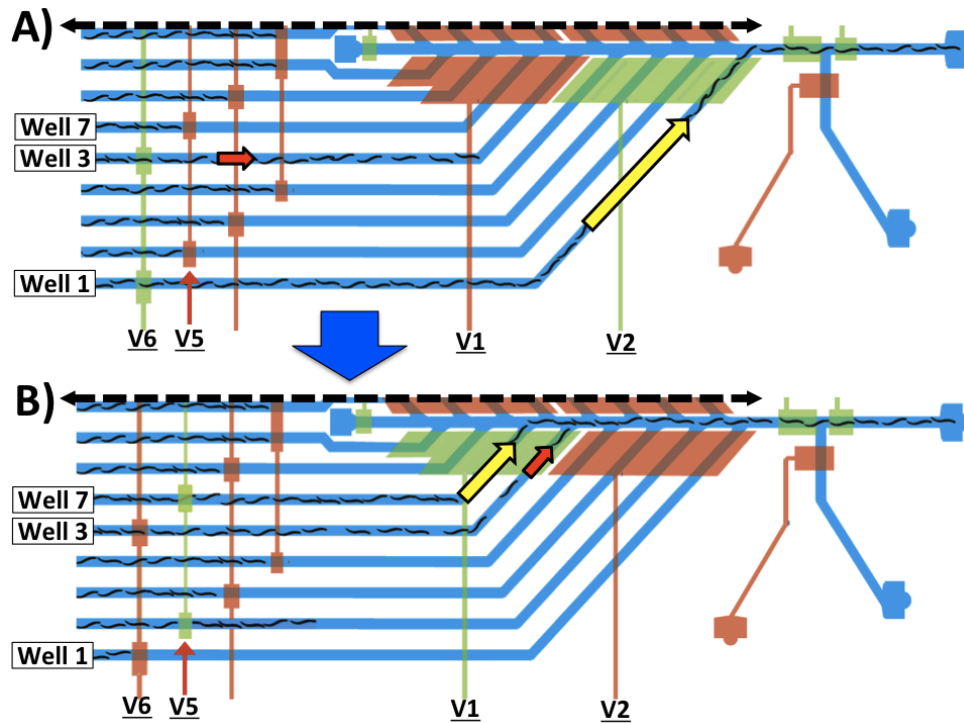


Figure 3.5: A mechanism for potential population mixing during a non-optimized automated delivery sequence.

A) During population delivery from *Well 1* (yellow arrow), *V6* needs to be opened, also allowing *Well 3*'s population to possibly swim (small red arrow) closer to downstream valve (*V1*) even if the downstream valve (*V1*) is closed and there is no flow in the well-channel of *Well 3*. B) If we choose to initiate delivery from *Well 7* (yellow arrow) following delivery from *Well 1*, without a flushback step on *Well 3*, we run the risk of *Well 3*'s worms (small red arrow) also swimming into the main channel with *Well 7*'s population since *V1* must open.

Secondly, the chosen order of well columns unloaded assured that wells whose channels intersect furthest downstream in the main channel had their populations delivered earliest in the sequence. Specifically, the sequence began with *Wells 1-4* in column 1 and proceeded until populations in *Wells 13-16* in column 4 were delivered last. Based on the schematic in Figure 3.1, it is apparent that a specific population of worms

traveling in the main channel towards the *Main Outlet* could not contaminate any undelivered population as it passed by the downstream well channel intersections of other wells. Either the downstream well channels were already emptied if they shared the large open valve near the main channel with the chosen well channel, or they were not yet emptied but closed off from the main channel by one of the other large valves. Independently, with the new configuration of staggered channels, we never observed worms unintentionally entering a well channel.

3.2.4 Automated and fast worm population delivery

To achieve the fastest worm population delivery rates, prevent population mixing during delivery, and preserve worm viability, we optimized the delivery pressures and timings. To estimate minimum timings for full population delivery, we first measured flow rates across the range of allowable pressures applied to the gasket, the on-chip valves, and flush. We then tested and adjusted these timing/pressure combinations until we reached nearly full population delivery from each well during the automation sequence. Finally, we verified that the optimized design and delivery sequence could indeed provide fast delivery without population mixing and/or damage to worm viability.

3.2.4.1 Flow rates through individual well channels

We measured flow rates across the individual wells to the *Main Outlet* for different gasket pressures ranging from 2.5 – 20 psi (~17 – 138 kPa), at 2.5 psi increments (~17 kPa) and compared them to theoretical calculations based on the flow resistance imposed by the individual well channel geometries [57]. Data was collected from one well in each vertical column of the well plate reservoir array.

Measured flow rates generally varied linearly with applied pressure (linear regression $R^2 = \sim 0.99$ for all measured data) and overlapped with the theoretically expected values within 10% (Fig. 3.6). Since fluidic resistance is directly proportional to channel length, the longer channels had lower flow rates given the same pressure at the gasket. This result implied that one would have to linearly adjust the pressures or timings applied to the wells via the gasket system to deliver the same number of worms across wells with different channel lengths. Such differences could be easily accounted for in the automation software, by adjusting the timings of the automation steps for each well.

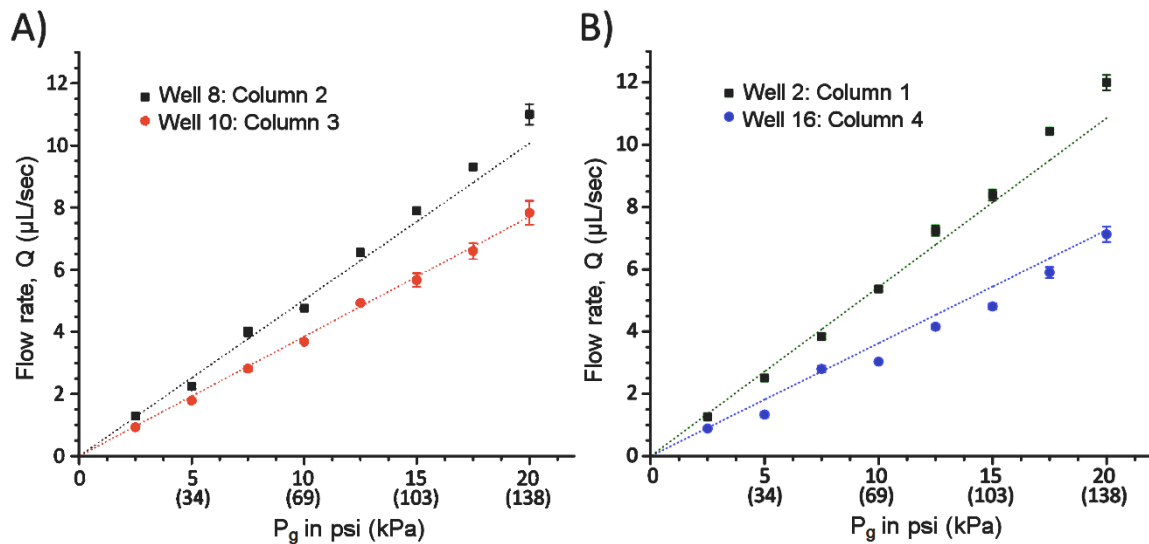


Figure 3.6: Fluid flow rates as a function of applied pressure.

Measured fluid flow rates through *Wells 2, 8, 10, and 16* plotted against theoretical values (dashed lines).

Sources of slight deviations from theoretical flow rates were most probably a result of the elastic properties of PDMS. At the higher pressures, it is possible for the PDMS channel cross-sections to expand and effectively decrease the channel's fluidic

resistance [70]. This expansion might have been the cause for the slightly higher-than-predicted flow rates observed above 12.5 psi (~86 kPa) in *Wells 2* and *8*. Other sources of small drifts from theoretical values could include physical inconsistencies at the external interfaces to the microchannels caused by the variability of manual punching or the slight accumulation of debris in the device.

3.2.4.2 The automation sequence

We optimized the delivery sequence to shorten the delivery time of the full population from each well, while still preventing population mixing during delivery. Figure 3.7 illustrates the steps of the automation sequence and Table 3.1 presents the optimized timings and the on-chip actuation scheme used in each step.

Within a few minutes after loading the worms in the wells and sealing the gasket, worms begin swimming to the first valve nearest to the wells, which are completely sealed to prevent worm passage (Fig. 3.7a). The delivery of worms then proceeded in four steps with an optimized timing for each step (Fig. 3.7c, Table 3.1). Figure 3.7c illustrates the steps of the automation sequence for *Well 1*, as an example. First, the system delivered a single population of worms out of the given well towards the *Main Outlet*. It then flushed excess worms from the main channel and completed their delivery to the location of interest by using flow from *Exit Flush*. Finally, it sent undelivered worms back to their origin well. Since *Exit Flush* had an essentially limitless fluid reservoir and faster flow rate per unit pressure than any of the well channels, it could quickly complete worm population delivery, which minimized the time spent driving

flow through the origin well. This strategy eliminated the risk of exhausting the well's fluid supply and introducing bubbles to the device.

Further sequence optimization could include the execution of Steps 3 and 4 simultaneously. Since *V9* is closed and *Main Channel Flush* is idle during Step 3, flow from *Main Channel Flush* can be directed back to the origin well to complete the well channel-cleaning step, while *Exit Flush* completes delivery of the original population. This approach will effectively eliminate Step 4's timing allocation for each well, reducing the overall delivery time for each well to 4 seconds.

Table 3.1: Timings for the automated delivery sequence applied to each well and device truth table for delivery from Well 1. “1” indicates the valve/fluid reservoir is pressurized, while “0” means that it is not pressurized. MCF- *Main Channel Flush*, EF- *Exit Flush*. All other valves not described here remain closed throughout this example.

Step	Timing (s)	Gasket	V2	V6	V9	V10	V11	V12	MCF	EF
1	2.8	1	0	0	0	1	0	0	1	0
2	0.5	0	1	1	0	1	0	0	1	0
3	0.7	0	1	1	1	0	0	1	0	1
4	0.7	0	0	0	0	0	1	1	0	1

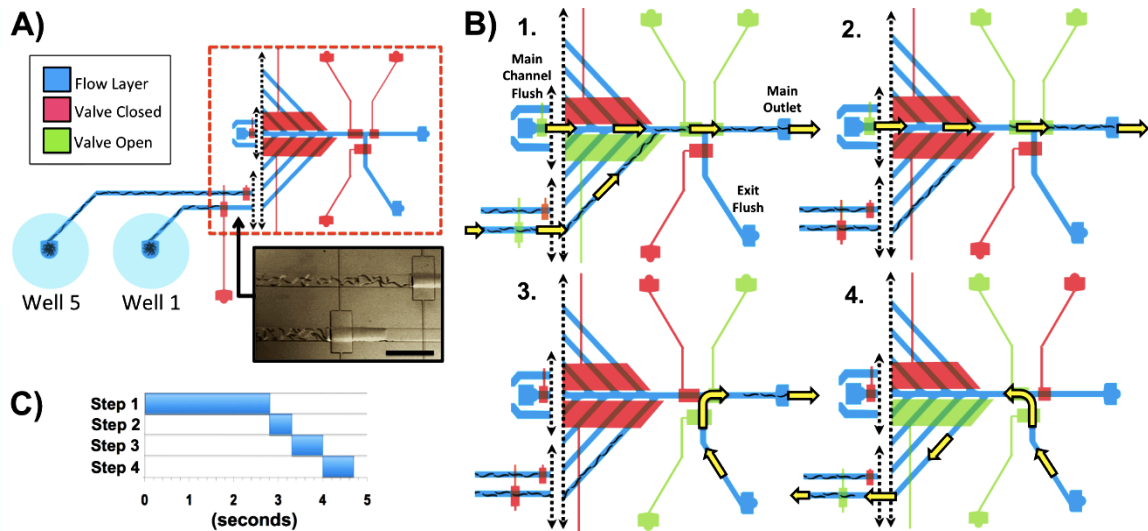


Figure 3.7: Automated worm population delivery sequence

A) Schematic of device showing areas active during sequence example as the worms are pre-staged at first set of control valves. An image of pre-staged *C. elegans* worms is below the schematic (scale bar is 1 mm). B) Illustration of all steps for one full sequence cycle. Step 1: Appropriate valves open as the gasket is pressurized to send *Well 1*'s population to the main channel, where *Main Channel Flush* then accelerates the worms' transport to the main exit. Step 2: Excess worms are cleared from the main channel towards the *Main Outlet* via flow from *Main Channel Flush*. Step 3: Flow from *Exit Flush* delivers the worms from the *Main Outlet* to an off-chip location. Step 4: "Flushback"; *Exit Flush* flow is redirected backwards to clear any remaining worms in the well channel back to *Well 1*. This step is executed on *Wells 1-4* only after finishing Steps 1-3 on each of them. C) Timings for each step.

3.2.4.3 Timing optimization

We optimized the timings of the automation sequence by placing worm suspensions (~100-200 worms/well, strain: SK4005) that had reached the L4 life stage into the wells and running the automation sequence to induce flow through the wells at various pressures and timings. We collected the worms delivered during the automated sequence in a well plate. Worms that did not get delivered during the sequence were

collected immediately afterwards. The two groups were counted for each well in order to determine the total number of worms initially loaded in a given well relative to the total delivered during the sequence.

Considering the measured fluid flow rates (Fig 3.6) and well channel distances, we postulated adequate timings for the full population delivery from each well for a given pressure. Based on these calculations and preliminary experiments, we found a timing of 2.8 seconds for Step 1 with the maximum pressure (20 psi, ~138 kPa) applied through the gasket, would be adequate to empty the slowest wells in the device. Thus, we applied this timing to all of the wells to ensure maximal delivery success across the chip at the highest pressure.

3.2.4.4 Fast worm population delivery

To characterize the robustness of the population size delivery across different pressures at the chosen timing, we measured the number of delivered worms for various gauge pressures to the gasket and the *Main Channel Flush* fluid reservoir (5 – 20 psi, ~35 – 138 kPa) but maintained a 20 psi gauge pressure for the *Exit Flush* reservoir throughout the experiments. The conical cross-section of the wells enabled a majority of the worms loaded into a given well to settle at the base of the sample reservoir, in proximity to the well channel entrance or the first valve (Figs. 3.1c and 3.7a). With the conical shape of wells and optimized timings in the automated delivery sequence, we achieved quick and nearly complete delivery of the worm populations from the on-chip wells to an off-chip location.

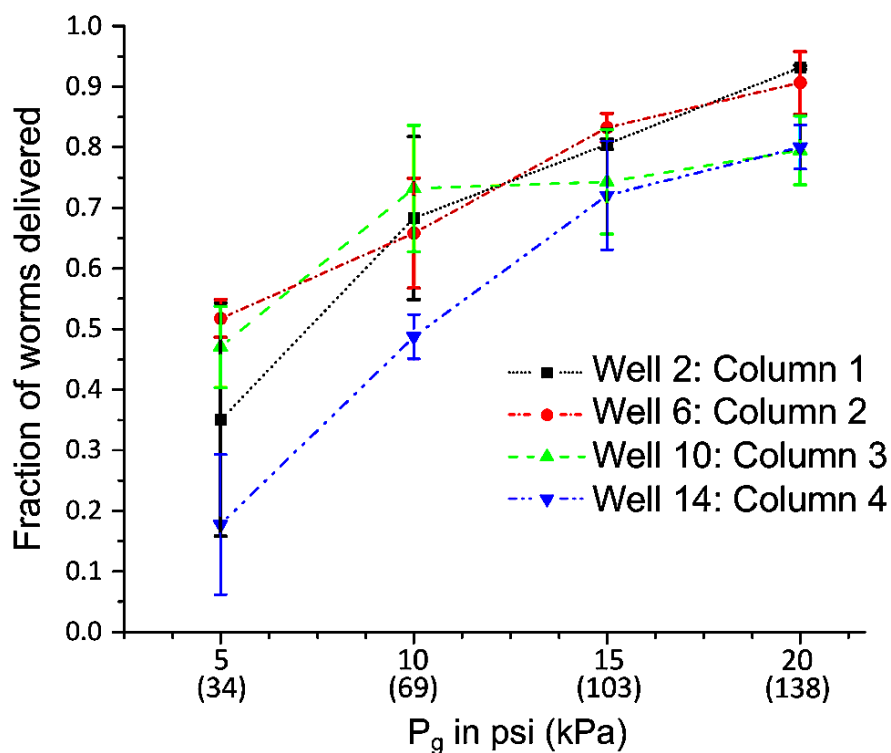


Figure 3.8: Worm population delivery as a function of applied pressure.

The fraction of worm populations loaded in 4 representative on-chip wells from 4 different columns of the *Population Delivery Chip* that are delivered to the outlet of the device as a function of pressure applied at the gasket and the *Main Channel Flush*.

Figure 3.8 shows what fraction of the initially loaded worm populations in 4 wells were delivered for various gauge pressures applied to the gasket and the *Main Channel Flush*. At the maximum pressure applied to the gasket and *Main Channel Flush* (20 psi, ~138 kPa), the *Population Delivery Chip* only required 4.7 seconds per well to deliver an average of 80 – 93% of each worm population initially loaded into the on-chip wells. Delivery of more than 100 worms for each population is more than adequate for most *C. elegans* bioassays. The achieved delivery speed took place in a fully automated process and was nearly an order of magnitude faster than any other platform capable of delivering

worm populations from wells without bubbles (45 sec vs. 4.7 sec). Saving 40 seconds of transport time per population would potentially eliminate 40 million seconds of actual experimental time when applied to a million-compound screen. This is equivalent to 1,388 days (8 hrs/day), 277 weeks (5 days/week), or 5.55 years (50 weeks/year) of time savings for a single large screen.

Since a majority of the worms settled at the bottom of the wells before delivery, most of a population moved from its well to the main channel after only fraction of the well reservoir volume was exhausted. Consequently, the fluid level in a given well was maintained near its initial value and bubbles could not enter the device via exhaustion of the reservoirs. If desired, we could create actuation timings that nearly but not completely exhaust the wells' fluid supplies without bubble introduction since the flow rates were well characterized. We could further improve the overall delivery speeds and efficiency by reducing overall channel lengths and increasing channel cross-sectional dimensions to reduce flow resistances, and applying higher pressures to the gasket and flush channels.

3.2.4.5 Experimental validation of population segregation

We next performed experiments to confirm that the automation and device architecture maintained worm population segregation. Instead of using 16 different populations, we used only 4 strains and ran two different tests. In the first test we loaded each row of the well-reservoir array with a different *C. elegans* strain, and then in the second test we loaded each column with a different strain. Each of the 4 strains had a different set of neurons labeled with endogenous fluorescent markers, making visual

differentiation between the strains via microscopy very simple. We placed one of the 4 strains into a set of 4 wells and ran the automated delivery sequence at the maximum operational gauge pressure (20 psi, ~138 kPa). We then collected the populations in 96-well plates and observed each worm collected on a fluorescent stereoscope to characterize their neurons' morphologies and confirm strain type. We also counted the number of worms belonging to each strain within the collected population samples.

The data shown in Figure 3.9 suggest that a synergy of the automated delivery sequence and microchannel architecture prevented population cross-contamination between wells during operation of the *Population Delivery Chip*. With each row of the well-reservoir array having a different *C. elegans* strain (Fig. 3.9a), the device only delivered worms of the expected strain for each well. This result implied that there was no mixing between the rows of the well array. However, mixing between columns was not yet ruled out in this case, since all four wells in each row had the same strain. To confirm the elimination of mixing between columns, the experiment was repeated with a distinct strain loaded in the 4 wells of each column instead of each row (Fig. 3.9b). These experiments definitively demonstrated the device's ability to deliver 16 different populations to a desired location without cross-contamination.

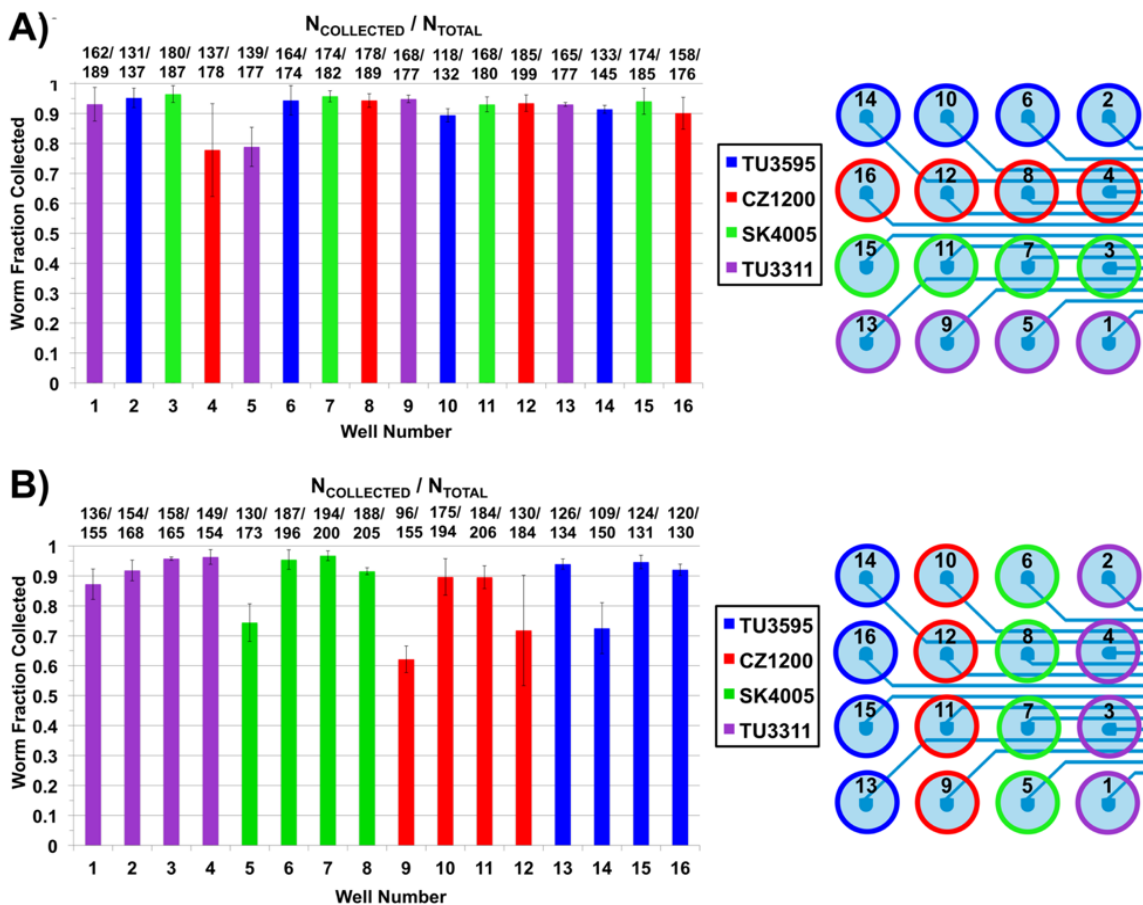


Figure 3.9: Population mixing eliminated during automated delivery at 20 psi (~138 kPa).

The graphs show the fraction of animals collected after delivery from a given well that are of the same strain initially loaded into the well. The actual average number of collected worms over the average number of those initially loaded is indicated above each bar. A) Four distinct strains loaded in each **row**. B) Four distinct strains loaded in each **column**. A corresponding color-coded schematic on the right of both graphs indicates into which wells the strains were loaded at the beginning of both experiments. Each color represents a single type of strain.

3.2.5 Animal viability after delivery through the device

To test the effect of chip delivery on worm viability, we loaded SK4005 worms into 4 representative wells on the device and delivered them to the main exit port with the automated delivery sequence. We randomly collected 20 worms from 4 wells for each condition tested and put each population onto separate NGMSR growth pads. For control tests, we also collected 20 worms from the original worm suspension, which never experienced on-chip delivery.

Figure 3.10 presents the day-by-day survival data of 20 worms after delivery through the chip with various pressures (5 psi, 10 psi, and 20 psi) applied to the gasket. When compared to the control group, differences in animal viability for 11 out of the 12 groups delivered through the device were not statistically significant. In all cases, every single worm survived at least 6 days and every population had at least one worm that lived between 23 – 29 days.

Table 3.2 further summarizes the total average lifespans of worms in the test groups and the log-rank test statistics comparing them to the control group. Looking at the average lifespan of worms in our control group (17.8 ± 6.6 days) there were almost no major decreases in average lifespans in worm populations delivered via the *Population Delivery Chip*. Among 12 viability tests, only the 20 psi (~138 kPa) group of *Well 14* showed a statistically significant difference. However, as can be seen from Figure 3.10, the drop off in viability relative to control begins after day 14, which could be attributed to factors such as worm handling during plate transfers. These results implied that the chip would

not significantly damage the animals, and the device platform could be a useful component in automating *C. elegans* bioassays across its entire operational pressure range.

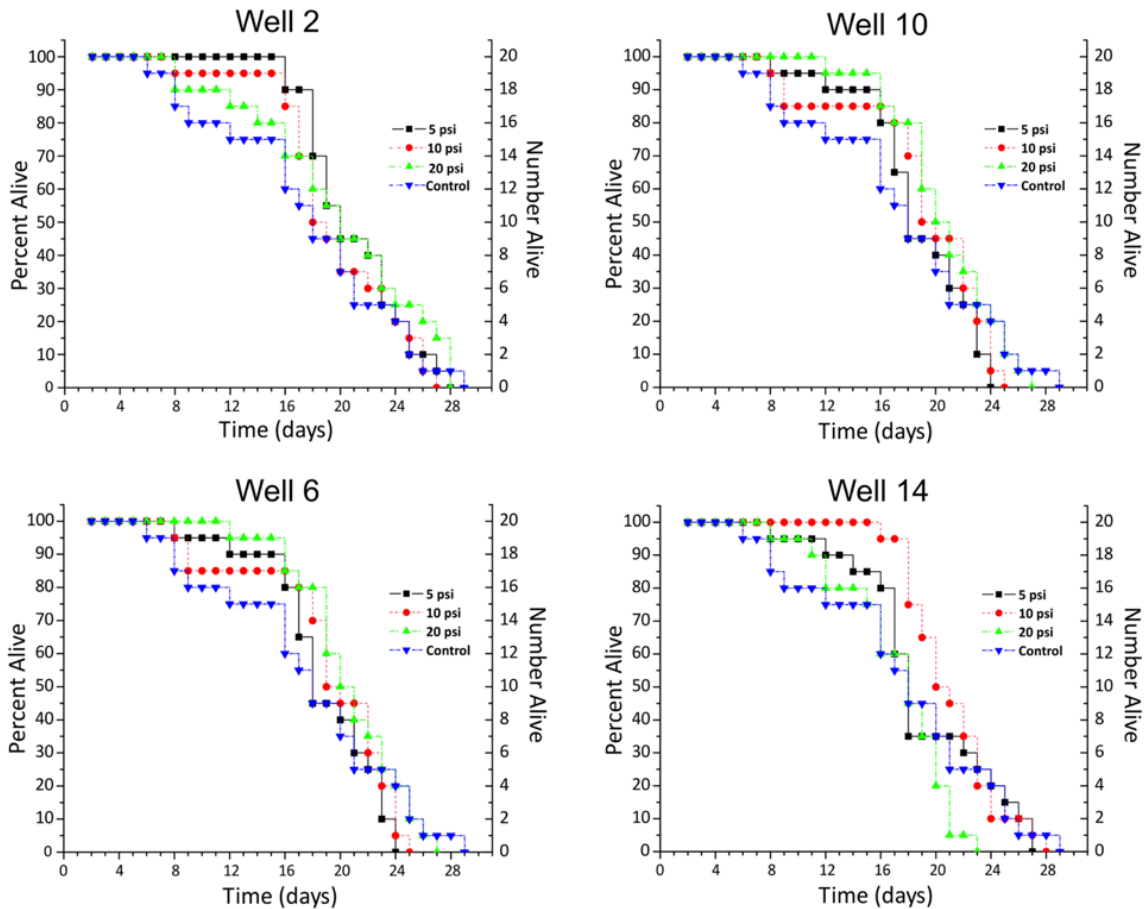


Figure 3.10: Worm viability test.

The daily change in live worm population numbers for 3 different applied pressures to the gasket relative to control in four representative wells; each well resides in a different column of the device.

Table 3.2: Average animal lifespan (days) after delivery through the whole chip under different pressure conditions. The initial size for each worm population was $n=20$. The average lifespan of worms in the control group was 17.8 ± 6.6 days (\pm indicates standard deviation). The p-value for each condition based on the log-rank test statistic relative to control is given as well. P-value <0.05 was considered significant.

Pressure	5 psi (~35 kPa)	10 psi (~69 kPa)	20 psi (~138 kPa)
Well Number	Life span (p-value)	Life span (p-value)	Life span (p-value)
Well 2	19.1 ± 3.7 (0.975)	17.8 ± 4.6 (0.447)	17.9 ± 6.3 (0.880)
Well 6	16.8 ± 4.1 (0.096)	17.2 ± 5.1 (0.366)	18.7 ± 3.8 (0.679)
Well 10	17.4 ± 4.3 (0.399)	17.3 ± 4.7 (0.352)	17.2 ± 6.1 (0.642)
Well 14	17.1 ± 5.1 (0.399)	19.2 ± 3.2 (0.956)	15.2 ± 3.9 (*0.036)

* Indicates statistical difference

3.3 MATERIALS AND METHODS

3.3.1 Device fabrication

We used modified multilayer soft-lithography techniques for the fabrication of our devices [49]. Two photoresist molds on silicon were used to pattern the two layers of microchannels in the device. The “flow layer”, which contained the worms, required two photolithography masks to make the positive photoresist (AZ50-XT, Applied Electronic Materials Inc.) features and the negative photoresist (SU-8 2025, Microchem Corp.) features. The average height of the “flow layer” was $\sim 55 \mu\text{m}$. A dummy volume was patterned around main exit channel to prevent over-development of portions that were patterned in positive photoresist. We also patterned the control layer mold in the negative resist ($\sim 36 \mu\text{m}$ in height).

We then patterned features into the elastomer (polydimethylsiloxane, PDMS, Dow Corning) with these molds. PDMS was mixed at a 10:1 (resin: crosslinker) ratio and poured onto the flow layer mold, which had conical P-1000 pipette tips pre-positioned on

the well entrance ports by a PMMA holder surrounding the wafer (Fig. 3.11). The conical wells could hold up to 100 μL of fluid depending on the height of the device. A $\sim 55 \mu\text{m}$ thick layer of PDMS was then spin-coated onto the control layer mold to create on-chip valves. We placed this layer with the mold in a 65°C oven until the spin-coated PDMS was partially cured. The PDMS flow layer piece was then bonded on top of the control layer via oxygen plasma treatment and sat in the 65°C oven overnight for bond strengthening. Though not absolutely necessary, oxygen plasma treatment enhanced bonding between the flow layer piece and the partially cured surface PDMS on the control layer mold. This treatment allowed for longer curing of the control layer's PDMS prior to bonding to reduce collapses of the flow layer channel ceilings onto the control layer mold's PDMS coating. After this process we bonded the entire chip to a sheet of 3/16 inch thick borosilicate glass via oxygen plasma treatment. The device was then left in 65°C for at least 4 hours to enhance the glass to PDMS bonding.

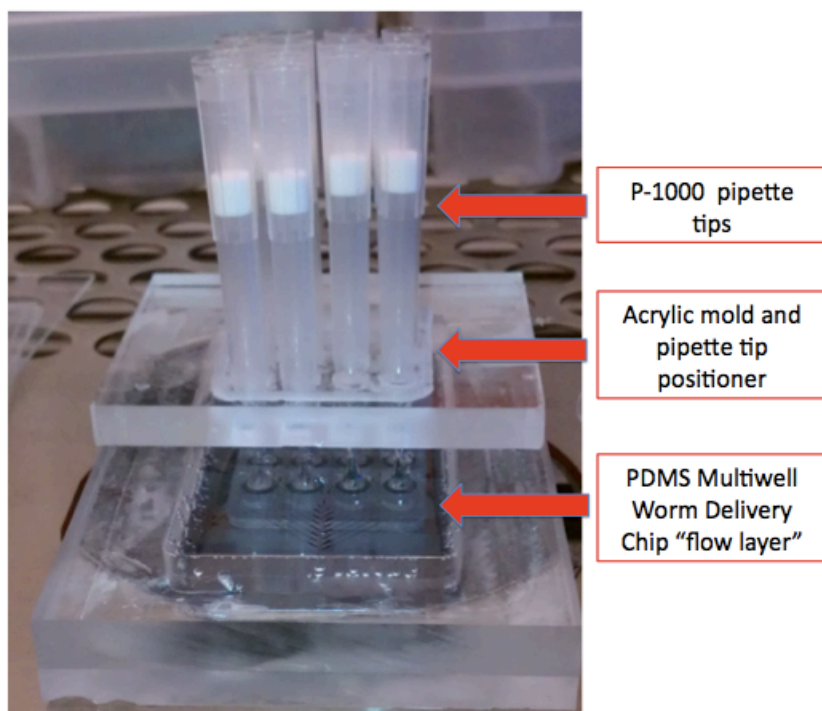


Figure 3.11: Fabrication of well plate reservoirs for the *Population Delivery Chip*.

To fabricate the on-chip wells, P-1000 pipette tips (Thermo Fisher Scientific Inc.) were positioned over the well channel inlets on the photoresist mold of the “flow layer” and these tips were secured to their positions via cured PDMS. PDMS was then poured into the PMMA barrier to create the bulk PDMS piece that would carry the device’s flow layer and population input wells.

3.3.2 On-chip valve control

The pneumatic control setup consisted of 16 three-way solenoid valves (The Lee Company) controlled through a voltage amplifier (ValveLink 8.2, AutoMate Scientific) and a NI-DAQ 6501 controller board (National Instruments), which was connected to a computer through via USB port. We fed DI water (valves) and M9 solution (flush channels) from air-pressurized reservoirs into the on-chip fluid inlets through the

solenoid valves. When they were in the “off” or open position, the inputs leading to on-chip valves were exposed to a vacuum of -8.7 psi (~-60 kPa) gauge pressure via the solenoids. The vacuum pressure increased the valves’ opening speed and led to faster on-chip responses to the automated control program.

We developed automation software in LabVIEW to control actuation of the solenoid valves. A separate image acquisition program provided by the camera manufacturer (Manta G201 IRC, Allied Vision Technologies) captured video and images during experiments.

3.3.3 Device fluid priming

After securing all of the fluidic connections on the device, we loaded 100 μL of M9 solution into each on-chip well. We then sandwiched the device in the gasket and sealed it to the device’s well plate reservoirs by uniformly tightening the four screw clamps (Fig. 3.1D). We primed the device for experiments by first introducing fluid from the flush channels until there were no longer any bubbles coming into chip. We then opened all of the on-chip valves excluding those that blocked off the flush channels (these channels eventually led to fluid reservoirs) and pressurized the wells at 7.5-10 psi (~50-70 kPa) through the gasket. Once fluid had completely filled the microchannels, valve *VII* (Fig. 3.1A) was closed to block flow out of the chip, while pressure was still applied to the gasket. This pressurization forced the remaining air bubbles to diffuse out of the fluid and into the surrounding PDMS. Generally, within 10 minutes all bubbles were removed from the device channels. All on-chip valves were then closed prior to sample loading.

We then released the chip from the gasket for worm population or fluid loading. First excess fluid was removed from each of the wells until ~10-20 μL of M9 solution remained. For fluidic flow rate experiments the wells were filled with M9 via syringe or pipette. For worm delivery experiments, worms were prepared in M9 suspension and loaded into the device at a density of ~100-200 worms per on-chip well. We then sealed the gasket to the device and for less than 5 minutes for the worms to settle to the bottom of the wells.

3.3.4 Measurement of fluid flow rates

We primed the chip with M9 solution and then executed an automated valve sequence to send fluid from a specific on-chip well during the application of different gasket pressures. Fluid exiting the chip was collected in a reservoir and weighed on a high-resolution scale (Adventurer Pro AV213, Ohaus Inc.) immediately after sample collection to negate effects of evaporation.

3.3.5 Worm culture techniques

Preparation of NGMSR plates seeded with bacteria

Saturated cultures of HB101 *E. coli* were grown by inoculating 250 mL of LB Broth, Miller (Fisher Scientific) with a single colony and incubating the culture for 24 h at 37°C. We seeded 10 cm NGMSR (Streptomycin-Resistant Nematode Growth Media) plates with bacteria by adding 1-2 mL of saturated HB101 to each plate and leaving the plates with their lids closed at room temperature for 2–3 days for drying. NGMSR pads were prepared with Nistatin (anti-fungal, Fisher Scientific, 0.01 mg/mL) and Streptomycin sulfate (anti-bacterial, Sigma Aldrich, 0.2 mg/mL).

We used the following strains in our experiments: SK4005: *zIs5 [(Pmec-4::gfp) + lin-15(+)] I*, CZ1200: *juIs76 [(Punc-25::gfp) + lin-15(+)] II*; *lin-15b(n765) X*, TU3311: *uIs60 [Punc-119::yfp + Punc-119::sid-1]*, and TU3595: *uIs72 [pCFJ90 (Pmyo-2::mCherry)+ Punc-119::sid-1 + Pmec-18::mec-18::gfp]; sid-1(pk3321); him-5(e1490) V; lin-15b(n744) X*.

Preparation of synchronous worms

We transferred a large population of gravid adult worms grown on seeded NGMSR plates to a small volume (0.3 mL) of a 1:2 mixture of 5 M sodium hydroxide to sodium hypochlorite (bleach). After 2-3 minutes, the adult bodies are mostly dissolved, leaving unhatched embryos intact. We spun down this suspension with a centrifuge, removed the supernatant, and then added 1 mL of distilled H₂O to wash out the bleaching solution. We repeated the washing step two more times, and pipetted the embryos onto an unseeded NGMSR plate. After 12 hours, most of the embryos reached the L1 life stage. These worms were then transferred to seeded NGMSR plates, where they reached the L4 life stage after an additional 24-28 hours.

Preparation of worms for device loading

L4-stage worms were cleaned of debris that might occlude channels in the Population Delivery Chip or downstream devices that would receive the animals. Worms were washed off NGMSR growth plates with filtered M9 solutions and pipetted into a 15 mL centrifuge tube that was placed in an ice-water bath for 5 minutes. The lower temperature prevented worms from swimming vigorously enough to stay afloat and the vast majority of them sank to the bottom of the tube. We removed the supernatant above

the worm pellet and then we refilled it with filtered M9. The process was repeated two more times to minimize bacteria and small debris in the animal suspension.

We then resuspended the worms, loaded 100 μ L of the worm stock into a well of a 96-well plate, and counted the population to determine sample density. If adjustment to the suspension density was required, we waited again for the animal stock to sink to the bottom of the centrifuge tube and adjusted the supernatant volume accordingly.

3.3.6. Worm viability

For viability tests, animals were scored every 24 hours [69]. The populations were incubated at 16.5° C throughout their lifetimes. The animals were scored as dead if they did not move after touch with platinum wire, or crawled off the agar pad. Whenever necessary, we transferred worms to new seeded plates to separate them from their progeny and contaminants. The log-rank test was used to determine statistical differences between test population and control population lifespans. P-values < 0.05 were considered statistically significant.

3.4. CONCLUSIONS

We designed, characterized, and optimized the *Population Delivery Chip* with integrated conical wells for delivery of *C. elegans* worms to a given automated fluidic apparatus. The device could deliver up to 16 different worm populations in sequence to a desired location from its 4x4 array of well plate format reservoirs without mixing any populations, harming the animals' viability, or the requirement for anesthetic treatments on the animals. The device used an automated loading sequence with software control to produce repeatable flow rates and sizes of delivered worm populations. Furthermore, the

platform displayed delivery throughput not seen in other more complex worm population delivery platforms. These advances will accelerate biosorter screens and provide a dependable macro-scale interface for delivering small organisms to automated microdevices for high resolution imaging and manipulation.

In future versions of the chip, initial loading of animal populations could be processed by robotic liquid-handling systems by pressurizing the on-chip pneumatic microfluidic valves to block flow in the well channels. These robotic platforms can handle culturing, preparation, and incubation of worm populations before loading into the delivery chip. Further optimization of channel dimensions would ensure that all channels leading to the wells would have the same fluidic resistances, thus ensuring the same flow rates and worm delivery rates across each well for the same pressures applied to the gasket and fluid inputs. Higher pressures coupled with larger channel cross-sections will allow much faster delivery times, potentially shorter than 2.5 sec/population. Finally, expanding the number of precisely regulated well reservoirs by an order of magnitude can be achieved by adding a few additional control valves to the set of multiplexed valves and rearranging the well channels' placement and geometry to accommodate more samples.

CHAPTER FOUR: A PLUG AND PLAY SIXTY-FOUR WELL MICROFLUIDIC DELIVERY DEVICE FOR *C. ELEGANS* POPULATIONS

The platform in chapter 3 established the technology and methodologies to perform fast and repeatable delivery of multiple *C. elegans* populations via a microfluidic interface. However, to truly perform large high-throughput screens with this approach, such a system must maximize the number of samples it can process and be compatible with current automated bio-screening platforms, such as robotic liquid-handling systems that use standard well plate sample holders. Here we introduce a microfluidic chip and corresponding gasket system that make a significant step towards bridging this gap. The chip utilizes the maximum area of a 96-well plate footprint to house 64 sample wells for holding populations, in addition to on-chip valve inputs. Subsequently, the gasket system not only pressurizes the wells to drive population delivery, but also brings individual pneumatic inputs to the on-chip valves. This design makes the system behave in a plug and play fashion. After loading samples into the wells, one simply secures the chip inside the gasket without needing to plug in many semi-permanent tubing inputs for each valve. A new automation software and electronic pneumatic system regulate flow such that faster, more complete, and more consistent delivery rates are achieved: 94% of the loaded population in a given well is delivered to the desired destination.

4.1 OVERVIEW

Expanding on our work with the device from chapter 3 for fast delivery of *C. elegans* populations, we have designed and fabricated a platform that handles several more worm populations and is fully compatible with well plate handling systems. This microfluidic chip contains 64 well plate-format reservoirs (Fig. 4.1), which can each hold a distinct worm population, and the device interfaces with pneumatic control inputs in a simplified plug and play fashion. These design elements enable simpler operation of the platform and will facilitate high-throughput screens on imaging platforms at a much larger scale.

We previously characterized the fluidic flow rates, worm population delivery rates, and animal viability of the 16-well device. This first iteration was capable of delivering each population in less than 5 seconds, an order of magnitude faster than the most advanced worm population delivery systems. Applying the knowledge gained while designing this device, we created a system with a four-fold increase in well plate-format reservoirs (64) and a more robust gasket apparatus to improve throughput and usability. We also updated the hardware and software components to give more consistent and controlled worm delivery rates. In the first generation system, we were able to deliver between 80-93% of given populations loaded into the on-chip wells in under five seconds. We engineered this second iteration platform with larger channel cross-sections and integrated dynamic electronic pressure regulators to achieve delivery at twice the speed of the 16-well device at an average rate of 94% of the total population loaded in each well.

A main innovation in this second generation system was the pneumatic gasket. To make the platform more amenable to automated fluidic plate-handling systems used in high-throughput biological research and drug screens, we significantly reduced the number of tubing ports plugged into the microfluidic chip. Instead of delivering pressurized fluid to the on-chip multiplexed valves via tubing, we delivered air-pressure through the gasket via individual ports to small liquid-filled wells built into the chip that interfaced with the on-chip valves. These ports were embedded in the gasket and sealed around each on-chip valve input with a small O-ring. This approach made the chips more modular and transportable between experimental steps, so they could be loaded with up to 64 *C. elegans* populations via conventional pipettors or liquid handling systems. An “all-stop” valve was integrated at the interface of each well-plate reservoir to the microchannels to prevent animals from escaping from the wells into the chip when the device was not in the gasket. After filling the chip with worm populations, the gasket clamp firmly sealed the gasket to the chip, and subsequently, the pneumatic inputs were activated to commence population delivery to an automated imaging platform.

We characterized the second-generation system by measuring fluid flow rates as a function of pressure applied to various device inputs, and we used this information to develop and test an automated worm population delivery sequence. We then validated the utility and repeatability of the sequence by characterizing population delivery rates and quantifying the extent of cross-contamination between sample populations loaded into the chip.

4.2 DESIGN AND TESTING

4.2.1 The 64-well population delivery chip

The 64-well microfluidic multiplexer chip's design (Fig. 4.1) took into account fabrication and operational techniques described for the 16-well chip in the previous chapter and expanded upon them to make the next iteration of the platform easier to operate and more amenable for high-throughput plate handling systems. As in the 16-well chip, the new device consisted of several conical well plate-format reservoirs connected to a single microfluidic channel patterned in PDMS, and flow in these channels could be regulated in any desired configuration by a multiplexed system of on-chip pneumatic valves. Similarly to the previous design, each channel originating from a well plate format reservoir intersects with the main channel that is connected to flush inputs residing upstream of all of the well channel intersections (*Main Channel Flush*) and near the exit of the device (*Exit Flush*) (Fig. 4.1b).

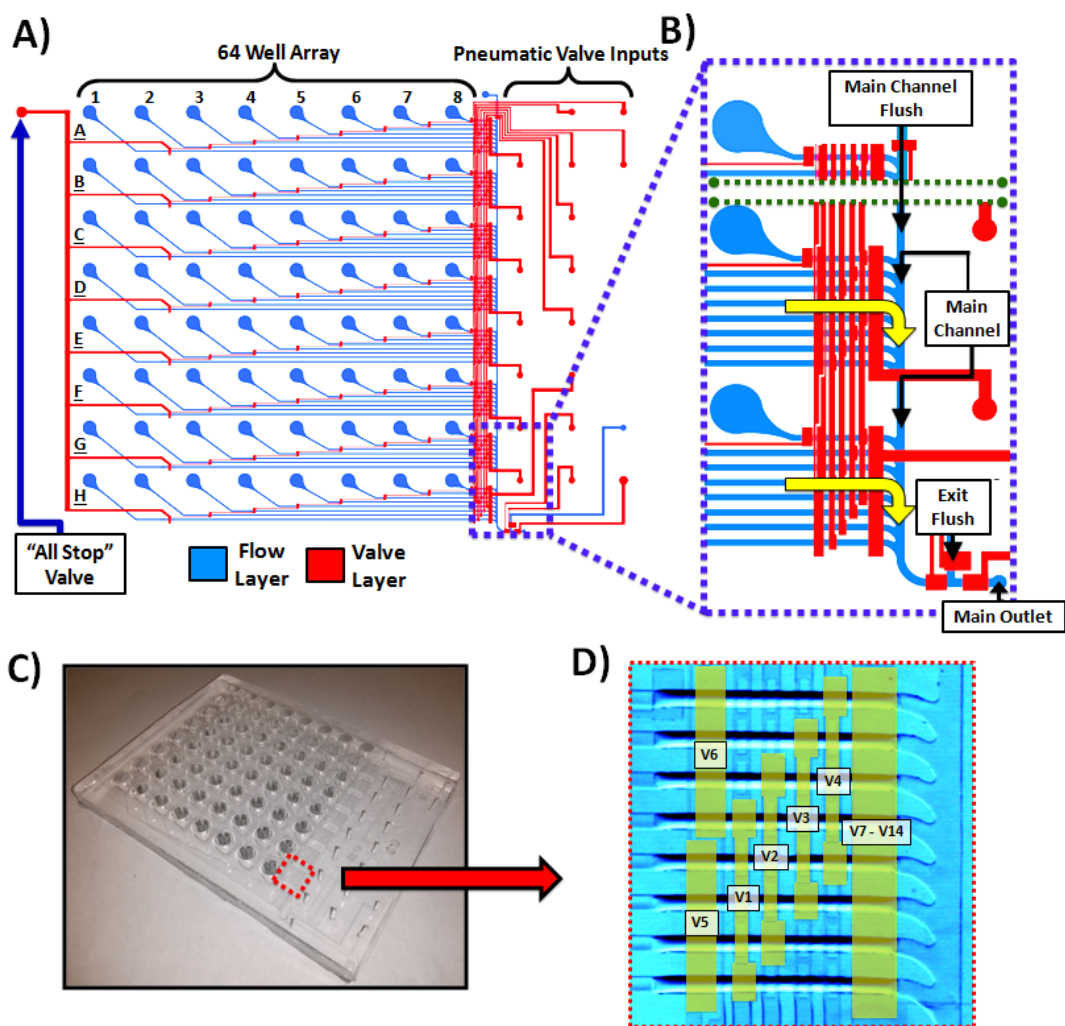


Figure 4.1: 64-well population delivery chip.

A) A schematic of the two-layer microfluidic device with the array of 64 well plate-format reservoirs and multiple pneumatic valve inputs. The blue layer houses the populations and the red layer contains the pneumatic on-chip valves inputs. Each well is referenced by the row (A-H) and column designation (1-8). B) Key functional areas of the device: worm populations arrive to the Main Channel from well reservoirs one-by-one via the paths indicated by the yellow arrows. Flush channels help with completing delivery without mixing. C) An image of the actual microfluidic device with a section of multiplexed valves that regulate a row of reservoirs in the array is indicated by the red square. D) An image of the interface of well channels from a single row in the reservoir array with the main channel. The set of corresponding multiplexed on-chip valves is indicated by the yellow outlines and corresponding valve names (V1-V14).

4.2.1.1 Microfluidic chip well channel array and valve design

Taking into consideration the 16-well chip, we wished to create a microfluidic device that scaled up that device's design rationale, while minimizing increases in overall complexity due to added well plate-format reservoirs. In the 16-well chip there were four well reservoir "groups" in the device that were organized by column in the reservoir array and corresponding valves regulated fluid flow in these columns (Fig. 3.1). Multiplexed valve control relied on two valves opening at once to permit flow through a specific well. One of these valves would choose the row (*V1-V4*) and the other valve would choose the column (*V5-V8*) in the well plate format reservoir array. For example, opening *V6* would permit flow through column 1 only, while *V5*, *V7*, and *V8* were closed. Concurrently, opening *V1*, while *V2-V4* were closed would allow flow through third row down in the well array (*Wells 3, 7, 11, and 15*). Thus, only opening these two multiplexed valves would exclusively allow flow through *Well 3*. As previously described, this design coupled with the proper order of serial population delivery conferred specific advantages to minimizing the number of flush back steps needed and eliminated cross-contamination during the automated delivery sequence.

Similarly, in the 64-well device we organized the wells into eight column groups, each consisting of eight wells. In this case, single valves controlled flow in two out of the eight columns of the device, and two additional valves would be needed to choose between these two columns (refer to the table below and Fig. 4.1.d):

Table 4.1: Valve regulation column groups. Figure 4.1 shows valve and column locations in the device.

Shared Valve	Column Number in Array
<i>V1</i>	1 and 5
<i>V2</i>	2 and 6
<i>V3</i>	3 and 7
<i>V4</i>	4 and 8
<i>V5</i>	1, 2, 3, 4
<i>V6</i>	5, 6, 7, 8

Valves *V5* and *V6* are responsible for choosing between the two columns regulated by each of the above valves. For example, exclusively opening *V1* and *V5* opens flow through only through column 1 in the 64-well device. Simultaneously, each of the valves, *V7-V14* specify which one of the 8 rows (*A-H*, Fig. 4.1a and d) is being addressed. The valve arrangement motif in Figure 4.1d shows how all of the aforementioned valves are arranged for each row in the array (rows *A-H*, Fig. 1a). This modular structure simplified designing the device and the automation sequence, which will be discussed shortly. However, based on the binary multiplexing logic, 64 wells should only require 12 multiplexed valves for flow regulation ($2 \times \log_2(n)$ valves controls "*n*" channels, [51]), while our system uses 14. Having two fewer valves may have slightly simplified the hardware design, but would have forced us to give up a more straightforward valve design with the modular motifs for each row in the well reservoir array.

4.2.1.2 Well plate reservoir "all-stop" valve

In terms of compatibility with liquid handling systems, the chip's "all-stop" valve prevented samples loaded into the wells from flowing into the device microchannels before interfacing with the gasket (Fig. 4.1a). This all-stop valve was actuated via a stand-alone pneumatic input that did not require an external feed pressure. This configuration permitted off-platform loading of the chip's 8x8 array of well plate-format reservoirs without sample populations escaping the wells into the main channel or cross-contaminating other samples. Once the populations were loaded into the device, all of the other on-chip valves could be closed via the gasket to stop flow and sample escape throughout, permitting release of the "all-stop" valve.

4.2.1.3 Microfluidic device fabrication

We fabricated the flow layer mold with larger channel heights to achieve faster flow rates in comparison to the 16-well device ($\sim 55\mu\text{m}$ versus $\sim 110\mu\text{m}$). Thus, for the flow layer, the ratio of the channel height to width in the 16-well device was $\sim 1:6$, whereas the 64-well device had a ratio of $\sim 1:3$. The taller channel heights prevented collapsing and bonding of the channel ceiling to the substrate in the most parts of the device. With the 16-well iteration, extra care had to be taken during this bonding step to avoid these collapsing events by applying very limited pressure to the PDMS piece in crucial device locations.

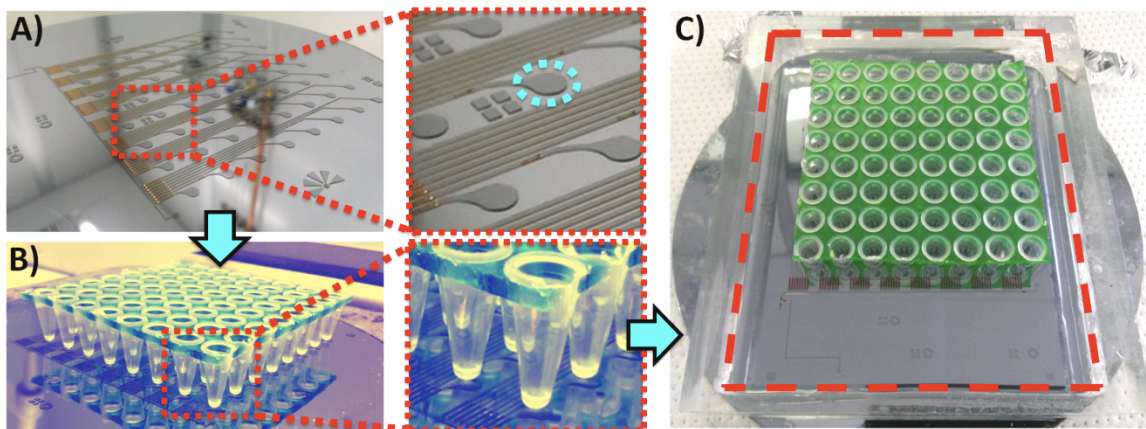


Figure 4.2: Workflow for fabricating the 64-well device flow layer.

A) The six-inch silicon wafer is shown with the patterned photoresist to mold the PDMS features. A sample input port is highlighted with the blue circle. B) An 8x8 well section of a PCR plate is aligned with the population input ports in the mold. C) An acrylic barrier piece (red lines) is then placed around the area patterned in photoresist, and PDMS is then poured into its inner boundary.

We utilized an 8x8 section of a PCR well plate for molding the well reservoirs into the chip (Fig 4.2). This technique greatly simplified well mold alignment with flow layer population input ports (Fig 4.2a). During fabrication of the previous 16-well device, we utilized an acrylic guide to individually position 16 P-1000 pipette tips at precise positions on the resist mold. This procedure required a great deal of manual dexterity and could require up to an hour to complete. It was difficult to position one pipette tip on the mold without creating movement in the acrylic positioner and displacing a previously placed pipette tip. Using the single 64-well section of a PCR plate to mold wells in the flow layer required much less time and concentrated effort since this process only

required positioning a single object in the correct position, as opposed to 16 or 64 pipette tips.

To ensure proper alignment of the device's flow layer piece to the control layer during bonding, we scaled the flow layer mold to account for the inherent shrinkage that occurs in PDMS due to exposure to specific temperatures and baking times. This scaling was necessary to accommodate for the alignment tolerances of the densely arranged valve and channel features in the large area design. Based on previous studies, we predicted that the device area of the flow layer piece in the plane of the silicon mold would isotropically shrink across the planar device area by $\sim 1.3\%$ from the original mold area [72]. The shrinkage forced us to purposely increase the area of the photoresist patterned mold by the predicted shrinkage factor to guarantee that channels in the flow layer aligned adequately with valve channel patterns in the control layer. When alignment was properly executed, all of the on-chip valves overlapped sufficiently with the designated flow layer channels. An important factor in this procedure was having simultaneous confirmation that alignment markers on opposite ends of the device were properly placed. Thus, we used two stereoscopes to visualize the markers during bonding. Having one stereoscope coupled to a camera that displayed its field of view on a nearby monitor and the other serving as a manual scope proved sufficient for alignment.

Creating such a large area device required modification of the glass to PDMS bonding procedure to minimize bonding defects and valve leakages. In particular, when both the large area PDMS device (~ 8 cm x ~ 10 cm) and the glass were placed in the plasma chamber, maintenance of uniform plasma across the entire surface of both pieces

became more difficult to maintain. Without uniform exposure to plasma, regions of poor bonding between the glass and PDMS resulted, causing cross-talk between valves in the device. We minimized these defects by first exposing the glass and then the PDMS piece to the plasma separately, so that these pieces could be placed in the central area of the plasma chamber and receive a relatively strong and uniform oxygen plasma dose across their surfaces.

4.2.2 Gasket system design considerations

The main design goals of the gasket system in 64-well device platform were to simplify the system operation workflow and increase the platform's amenability to high-throughput liquid handling systems. Improvements to usability were achieved by replacing the semi-permanent tubing interfaces (Fig. 3.1d) required to operate the on-chip valves (which are ubiquitous in the microfluidics field) with air-delivery lines permanently built into the gasket itself (Figs. 4.3, 4.4). Each time a new chip was loaded into the gasket system, there was no need to manually plug in each valve input to the chip by hand because the air-delivery lines in the gasket were designed to align and seal with the on-chip interfaces. By reducing the number of tubing inputs and creating a gasket and computer-control system that could still individually address each valve and consequently each on-chip well plate reservoir, this gasket system now acted more as a plug and play platform into which the microfluidic multiplexer chip could be quickly inserted.

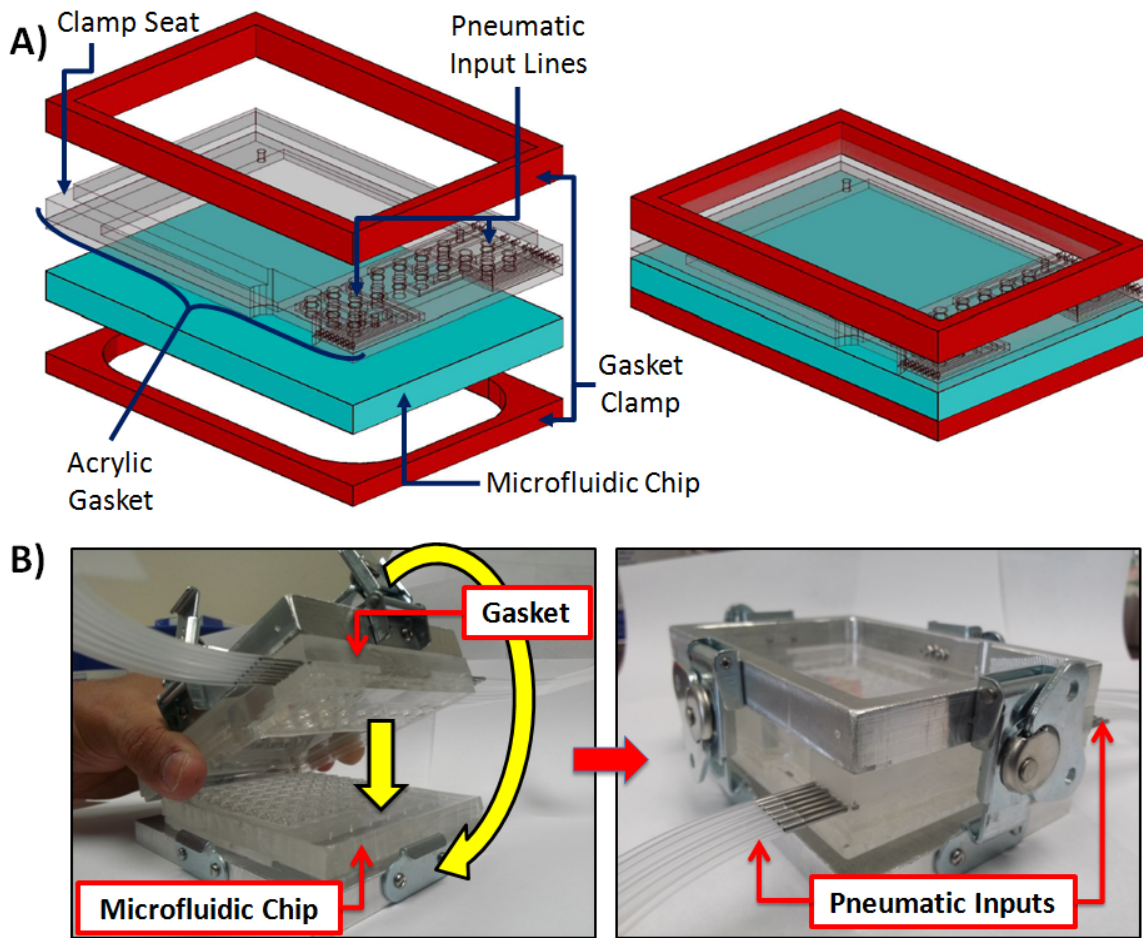


Figure 4.3: 64-well population delivery chip gasket system.

A) A schematic of the gasket system components indicates how they vertically stack (left) and combine together (right). B) The actual gasket system with pneumatic inputs and twist latches in an open (left) and sealed configuration (right).

4.2.2.1 Acrylic gasket component

The gasket system was composed of custom machined parts. A two-layer acrylic-rubber hybrid gasket delivered pressurized air to the microfluidic on-chip valve inputs and well reservoir array. The top layer was an acrylic piece consisting of machined indentations that would serve as air delivery lines. A thinner acrylic slab was then bonded

on top of the surface of the thicker acrylic part to cover the indentations and effectively create sealed channels. Precisely positioned holes in the thin acrylic piece served as pneumatic exits for these channels where the gasket interfaced with the microfluidic chip. The placement of the openings allowed air to travel from the gasket's pneumatic inputs to specific on-chip valves (Fig. 4.4). The openings on this second acrylic layer were bordered by rubber O-rings. When we tightened the clamp around the gasket and the chip, the hard rubber O-rings resisted the compression by vertically deforming the PDMS on the top surface of the chip and pressing against the gasket, creating a tight seal. These seals could resist up to ~ 207 kPa (30 psi) at the microfluidic valve interface (Fig 4.4 b,c) and ~ 138 kPa (20 psi) from the chamber above the well plate reservoir array (Fig 4.4b).

Inside the gasket, there were 18 air-delivery lines to pressurize the fluid in each on-chip valve and the well plate-format reservoirs (Fig. 4.3). Vertical holes were drilled through the entire gasket at locations where tubing interfaced the chip to deliver liquid into the device for the flush channel inputs (*Exit Flush, Main Channel Flush*). Preliminary tests with similar platform being developed in our lab indicate that fluid inputs for flush channels could also be fed via a sealed gasket feed, as opposed to the metallic tubing interfaces plugged directly into bulk PDMS.

The dense packing of all of these various pneumatic interfaces on the bottom surface of the gasket required the use of the O-rings in order to maintain the seals. Originally, it was projected that a thin layer of PDMS across this surface with air-access holes would be sufficient to create the necessary air-tight seals against the various inputs on the microfluidic device surface. We had used this approach with the gasket for the 16-

well device. However, the previous device's gasket was exerting compression force on much smaller area on the surface of the chip surrounding the well plate format reservoirs



Figure 4.4: Pneumatic on-chip valve actuation from the gasket system.

A) Individual pneumatic outputs and their corresponding air delivery lines are shown in the partially-assembled gasket. B) The entire gasket system with a microfluidic device and the pneumatic outputs sealed to individual valve inputs on the chip. C) A schematic illustrating the delivery of pressurized air (green arrow) via the gasket to an individual liquid reservoir connected to an on-chip valve to pressurize the liquid (red arrow) and close the valve.

when compared to the 64-well system. Secondly, the previous gasket was not required to seal small valve inputs that were located several centimeters from the clamping screws. The current gasket clamp exerts compression force directly on the outer perimeter of the gasket and relies on the rigidity of the gasket material to transfer this force to every interface between the gasket and the microfluidic chip. With PDMS between these junctures, pneumatic cross-talk and leakage between valve inputs occurred as a result of excessive PDMS deformation at pressures above ~ 207 kPa (30 psi). Instead, securing more rigid rubber O-rings directly to the acrylic surface and tightening the gasket clamp maintained all of the individual seals to the microfluidic chip across the required pressure ranges (Fig. 4.4).

4.2.2.2 The gasket clamp

A clamp sandwiched the gasket and the PDMS device (Fig 4.3). This component was essentially two aluminum pieces that could reversibly latch to each other and compress the gasket and the chip together such that desired pneumatic input pressures were maintained. A single twist latch on each of the four sides of the top clamp piece fastened to corresponding hooks protruding from the bottom clamp piece. Twisting all four latches till they could no longer be displaced provided enough force to seal the corresponding pneumatic inputs to the microfluidic chip via the O-rings. The top clamp piece fit snugly onto a step machined onto the topside of the gasket for simple and repeatable positioning.

We found that the gasket clamp had to be tightened to the highest degree possible without damaging the acrylic or the chip in order to guarantee adequate sealing and pressure maintenance, especially inside the chamber above the wells. Occasionally, subtle air leaks between the O-rings and the PDMS chip's surface were observed via submersion of the device in a water bath and tracking emerging bubbles, but the system maintained the desired pressures robustly.

4.2.3 Automated delivery system design

Several approaches were considered to achieve uniform and repeatable population size delivery across all of the well plate format reservoirs assuming that an equal number of worms were loaded in each well. One avenue could have been to design the microchannel geometries and dimensions in the multiplexer chip such that all of the channels emerging from single wells had uniform fluidic resistances across the device.

This approach would ensure that uniform pressure and timing parameters during automated delivery would result in equal fluid volumes and population sizes being dispensed from each well. However, achieving this would require building channels with variable widths and/or heights. Variable heights would have required us to pattern several layers of photoresist on a single mold; a prohibitively time consuming process due to the multiple iterations of fabrication optimization. The variability of photoresist feature heights typically seen in the patterning of even a single layer would have made achieving the desired dimensions very challenging. Concurrently, varying the channel widths would require a range of dimensions, which could have prevented us from equally spacing the reservoirs according to the 96 well plate arrangement, unless we considered a vastly different design.

Thus, a robust approach was assumed that would minimize the time needed for delivery of a maximum proportion of the populations as quickly as possible, while simultaneously addressing the variability in feature sizes encountered in photolithography. We used voltage-controlled pressure regulators to dynamically set the pressure applied at junctures in the microfluidic multiplexer that would require variable pneumatic application to induce nearly uniform delivery rates for each well in the device: the chamber above the wells in the gasket and the fluid reservoir coupled to the *Main Channel Flush* line. We took experimentally measured flow rates from each well and then deduced the potential time of flight for a given population of worms from each well plate format reservoir for a range of pressures.

With this information, we chose pressures to apply at the on-chip wells and the *Main Channel Flush* via our automation software and electronic variable pressure regulators to deliver the same proportion of each loaded population from the wells in a minimal time period.

4.2.4 Flow rates

To develop an automated sequence we had to characterize pressure dependent flow rates in important functional areas of the device, chiefly through the well plate-format reservoirs and the flush channels. From this information in addition to the channel dimensions characterized during fabrication of the chip, we could obtain estimates of fluid velocities and time of flight of the sample populations and determine the required time to deliver populations to the exit of the device within feasible pressure parameters.

We first characterized flow rates and time of flight through four representative wells in the chip. Looking at the schematic in Figure 4.1a, it can be seen that up until the main channel intersections, every well channel in a given column (*I-8*) has the same length and architecture, and concurrently every row (*A-H*) of well channels has the same arrangement of eight unique channel lengths. Given the same pressure drop across the wells to the *Main Outlet*, the only major variable parameter in terms of flow rates between equivalent well channels of different rows (e.g. *D5* versus *G5*) are the distances of their intersections with main channel from the *Main Outlet* (Fig 4.1b). With these considerations in mind, we characterized flow rates in the longest and shortest well channels (columns *I* and *8*, respectively) in rows that were the nearest and farthest (rows

H and *A*, respectively) from the *Main Outlet* to cover the full range of possible flow rates in the device.

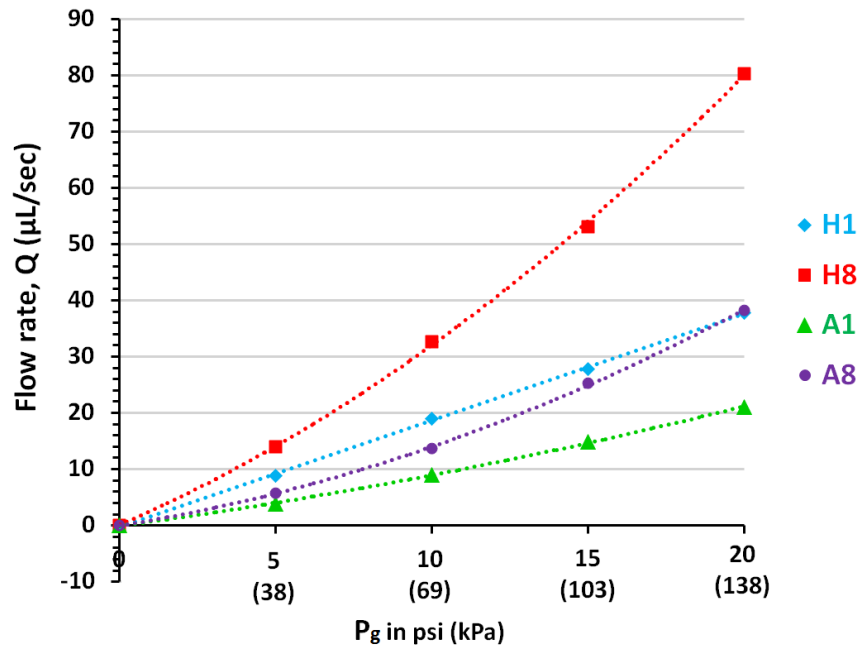


Figure 4.5: Measured fluid flow rates as a function of applied gauge pressure at the gasket in four representative wells from the 64-well population delivery chip. The dotted lines are polynomial fits to the measured data.

As expected, the data shows that flow rates through *Well H8* are the fastest because the path length from its well reservoir entrance is the shortest amongst all the wells in the device, resulting in the smallest fluidic resistance (Fig. 4.5). Concurrently, flow rates through *Well A1* are the slowest in the device since its path length and fluidic resistance is largest of the wells. Based on the device design, all other wells should have flow rates for a given air pressure applied at their entrances that would fall somewhere between the flow rates measured for *Well H8* and *Well A1*.

Dividing the flow rates by the average channel cross-sectional area of a given well channel provided the average fluid velocity through the channel. Using this data along with the path length from well entrance to the *Main Outlet*, we could see that for pressures at 10 psi or higher applied to the gasket, all wells in the device had time of flights under 1 sec between the well and the *Main Outlet* (Fig. 4.6). This implied we could achieve delivery much faster than the 16-well device, which needed around 2.5 seconds to initially move a majority of the population out of the well, followed by additional flush steps. The main source of flow rate improvement was due to doubling the channel cross-sectional areas across the device, thus decreasing the overall fluidic resistance.

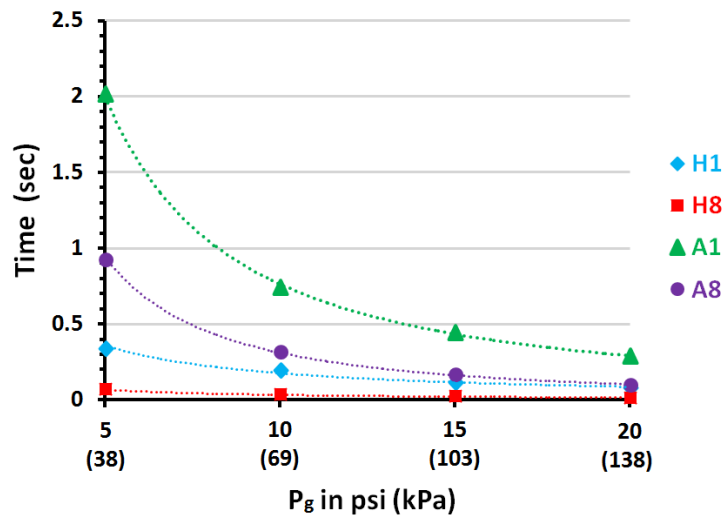


Figure 4.6: Time of flight from four well entrances to the *Main Outlet* as a function of pressure applied at the gasket.

The dotted lines are power law fits to the data.

4.2.5 Automated delivery sequence

The steps of the automated delivery sequence for sending a population from a single well (*Well H8*) is shown in Figure 4.7. Briefly, after worms from every well have been staged at the first set of valves nearest to their entrances (*V5* and *V6*) the platform pressurizes the fluid in the wells and opens the corresponding valves to allow delivery of worms from *Well H8* to the *Main Outlet*, while simultaneously sending pressurized fluid from *Main Channel Flush* toward the exit as well. Like the previous device, this flow from the *Main Channel Flush* prevents worms from spontaneously flowing in the wrong direction. After a majority of the population has passed the multiplexed valve section (*VI-VI4*), these valves close and the *Main Channel Flush* continues to send fluid to push the worms to their desired location off chip and through the coupling tubing. This step also clears out any remaining worms out of the *Main Channel*. Finally, flow from *Main Channel Flush* is directed back towards the well to clear out worms caught between the multiplexed valves during Step 1. This is accomplished by opening the multiplexed valves and closing off the exit. Simultaneously, the *Exit Flush* continues the population delivery by sending flow through the *Main Outlet* to the external destination.

The third step in the automation sequence essentially executes Steps 3 and 4 of the sequence described in Chapter 3 simultaneously. This strategy saves a significant amount of time during the delivery process, while still ensuring that the various worm populations will not cross-contaminate. Table 4.2 describes the valve actuation scheme and timings for the sequence steps. Valve and fluid input names refer to components described in Figures 4.1 and 4.7.

Table 4.2: Timings for the automated delivery sequence applied to each well and device truth table for delivery from *Well H1*. “1” indicates the valve/fluid reservoir is pressurized, while “0” means that it is not pressurized. MCF- *Main Channel Flush*, MCV- *Main Channel Valve*, EF- *Exit Flush*, EV- *Exit Valve*. All other valves not described here remain closed throughout this example.

Step	Timing (s)	Gasket	V1	V5	V7	EV1	EV2	EV3	MCV	MCF	EF
1	1.5	1	0	0	0	0	1	0	0	1	0
2	0.75-1.25	0	1	1	1	0	1	0	0	1	0
3	0.25	0	0	0	0	1	0	0	0	1	1

Like the previous device, the order of well populations delivered played a key role in eliminating cross-contamination events and minimizing the total time to deliver all 64 wells. The two main strategies used with the first device's delivery sequence were to deliver from wells that interfaced with the main channel nearest to the *Main Outlet* before those that interfaced more upstream and to select the order of wells emptied based on column groups. These tactics eliminate the possibility that any number of worms from an undelivered population will infiltrate the spaces between the multiplexed valves, so they would not be in a position to contaminate another population during its delivery. Figure 3.6 illustrates an example of this type of contamination event. For the device discussed here, cross-contamination could occur under similar circumstances. A result of opening *V1* is that all populations in column 8 can move past *V1* up to one of the following valves, *V7-14*, which are the final barriers to worms entering the *Main Channel*. Since the system must open one valve out of the set including *V7-V14* to deliver a given population, it is imperative that all populations in column 8 are delivered before any other on the device. As an example, in Figure 4.7 the population highlighted by the purple

rectangle (*Well G1*) in step 3 will be delivered next in the sequence because it has moved up to *V8* during the previous population's delivery.

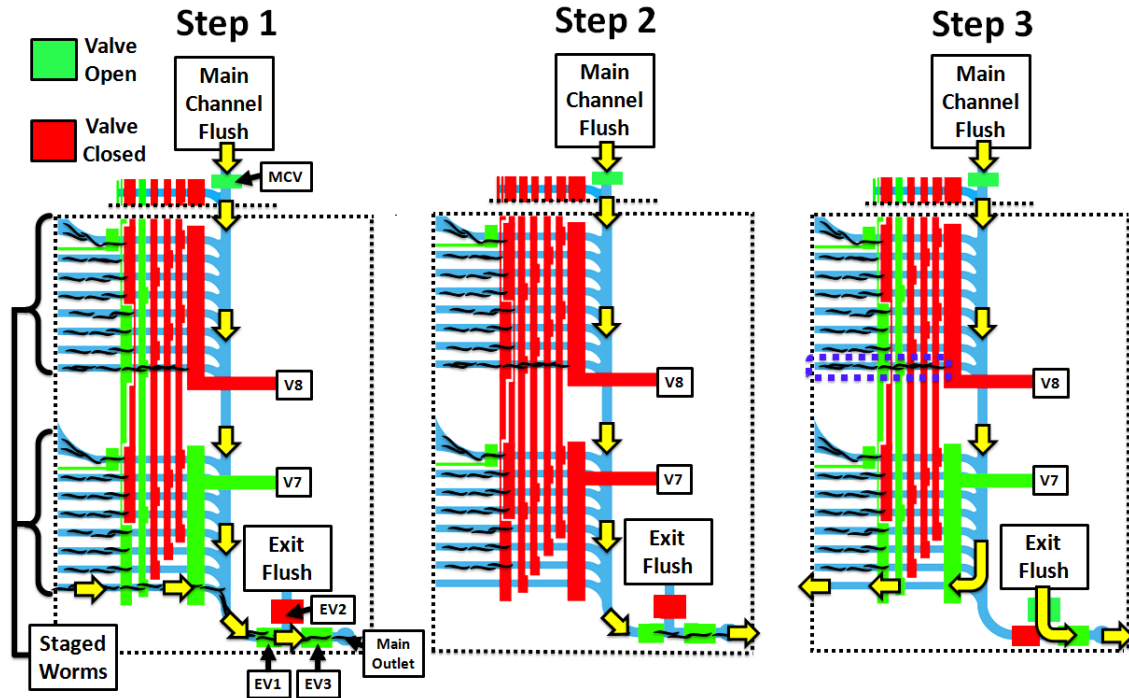


Figure 4.7: The automated delivery sequence for delivery from *Well H1*.

Step 1: Worms (curved black line segments) loaded in the wells are staged near the valves closest to the well entrances. Appropriate valves open as the gasket is pressurized to send the population from *Well H1* to the main channel, where *Main Channel Flush* then accelerates the worms' transport to the main exit. Step 2: Excess worms are cleared from the main channel by flow from *Main Channel Flush*. Step 3: Flow from *Exit Flush* delivers the worms from the *Main Outlet* to an off-chip location, as *Main Channel Flush* is simultaneously directed backwards to push remaining worms in the well channel back to *Well H1*. In the schematic for Step 3, a purple rectangle indicates the next population to be delivered (*Well G1*). An alternative version of Step 3 is executed for the final well in a given column, such that all wells in the column receive a simultaneous flush back flow from the *Main Channel Flush*.

Based on the device architecture and the sequence optimization considerations we developed an order for serially delivering from all 64 wells in the device. Figure 4.7

labels each well based on its temporal position in the sequence. The progression of wells delivered ensures that each well in a given column is emptied before a well of another column is addressed, and the order guarantees that wells that interface the *Main Channel* closest to the *Main Outlet* will be emptied before their upstream counterparts. During the delivery sequence for the last well in a given column (any well in row A), the program executes a modified version of Step 3 in which flush back is performed on wells in the column in order to prevent any worms that have slipped past *V5* or *V6* from cross contaminating with subsequent samples.

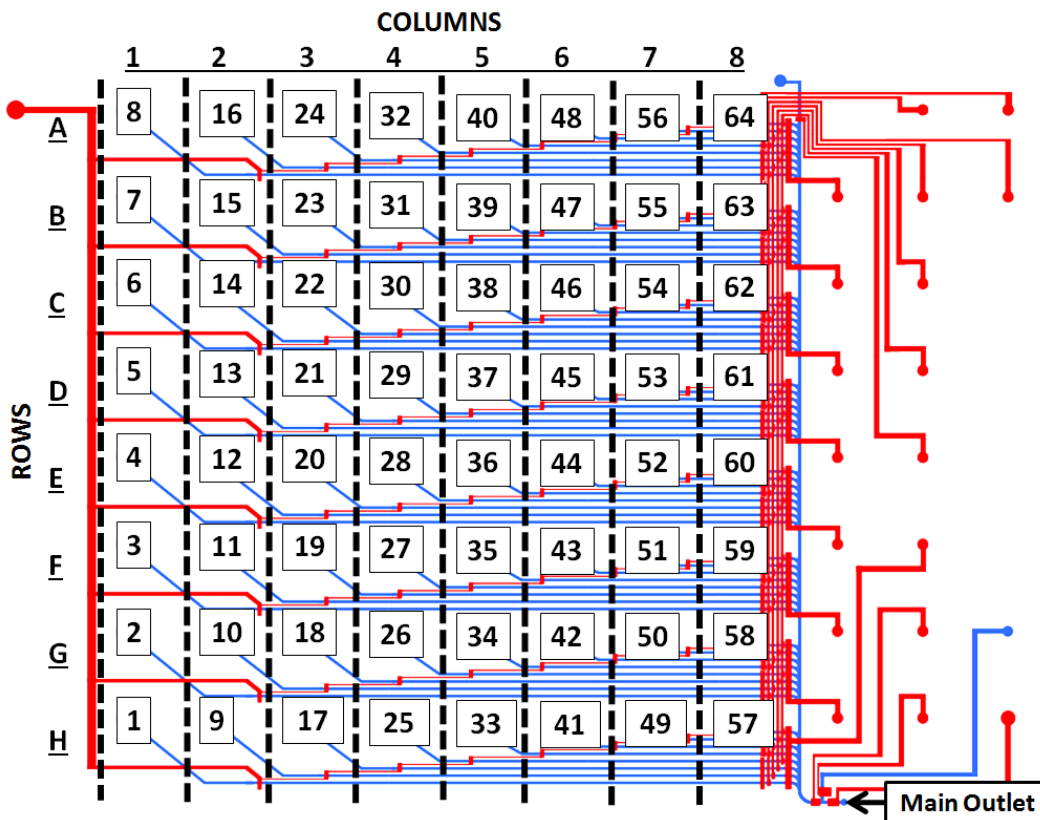


Figure 4.8: Optimized delivery order for emptying all 64 wells in the microfluidic device.

Wells are labeled with their position in the serial delivery sequence during automated device operation.

4.2.6 Ultra-fast worm population delivery

Our empirical measurements of flow rates through relevant wells in the device and initial tests with worm populations arrived at sufficient delivery times and pressures applied at the various pneumatically-driven inputs to achieve up to ~97% population delivery of the initially loaded population in under 3 seconds from the wells tested. We chose to test delivery through the four wells (*A1*, *A8*, *H1*, and *H8*), which represented the maximal and minimal flow rates per unit pressure applied to the gasket through their well channels and comprised the device's extremes for well channel distances from the *Main Outlet*. This strategy was meant to validate proper delivery from all wells in the device since the full range of critical parameters relevant to delivery rates would be evaluated.

We applied up to ~103 kPa (15 psi) at the gasket to the well reservoir array and varied the pressure sent to the *Main Channel Flush* fluid reservoir via the electronic pressure regulator to compensate for variable flow rates through the different well channels. This compensation was motivated by the finding that when the pressure applied to the well reservoirs through the gasket matched the pressure applied to the *Main Channel Flush* fluid reservoir during Step 1 of the sequence, worms occasionally would not even emerge from the wells, especially wells residing in row *A*. We believed that flow from *Main Channel Flush* overwhelmed or effectively blocked the simultaneous flow emerging from the well.

Applying variable pressures at the *Main Channel Flush* fluid reservoir enabled generation of fluid flow rates emerging from the *Main Channel Flush* that were a reduced fraction of flow rates coming out of the delivering well. Specifically, during Step 1 of the

delivery sequence we found that setting the pressure so that the flow rate emerging at the *Main Channel Flush* input was seventy-five percent of the flow rate emerging from the well of interest minimized the flush channel interfering with the population delivery. For *Well A8* we found that setting the *Main Channel Flush* flow rate at sixty-five percent of the supposed well channel flow rate conferred a higher yield of worms than the seventy-five percent setting. Additionally, we had to increase the duration of Step 2 for this well by 0.5 seconds to clear a majority of the worms exiting the well from the *Main Channel*. For the timings used we found that pressures between ~69 and ~103 kPa (10-15 psi) at the gasket, along with the reduced factor pressure at the *Main Channel Flush* were sufficient adjustments in the sequence to achieve efficient delivery (Fig 4.9, 10 psi: 81% \pm 10 and 15 psi: 94% \pm 2). These delivery rates were a considerable improvement over the performance of the 16 well device in Chapter 3, where the range of delivery rates was ~80-93% when 20 psi was applied at the gasket and the *Main Channel Flush* reservoir. In fact, at ~103 kPa (15 psi) applied to the gasket and a *Main Channel Flush*, we observed a nearly complete removal of the population from the well in under 1 second (Fig 4.10). These findings imply that the lower fluidic resistances and flow rate compensation mechanisms in the 64-well device setup result in far more consistent and efficient population delivery than what was achieved on the 16 well chip platform.

Preliminary tests showed that the established sequence timings were not sufficient to deliver measureable worm populations at ~35 kPa (5 psi) applied at the gasket. Step 1's time duration would have to be increased considerably to achieve valuable delivery rates at this pressure applied through the gasket. At the maximal pressure, we found that

applying ~ 138 kPa (20 psi) at the gasket caused leakage or "cross-talk" between flow from multiple wells, as the pressure was sufficient to overcome the valve sealing on-chip for a few of the wells. Since the 64-well device's flow layer channel height was nearly twice the height of the 16-well chip, the channel ceiling or "membrane" above the control layer were required to deform twice as much in the newer device. This channel height discrepancy could explain improved ceiling of the 16 well device's valves during the application of 20 psi at the gasket.

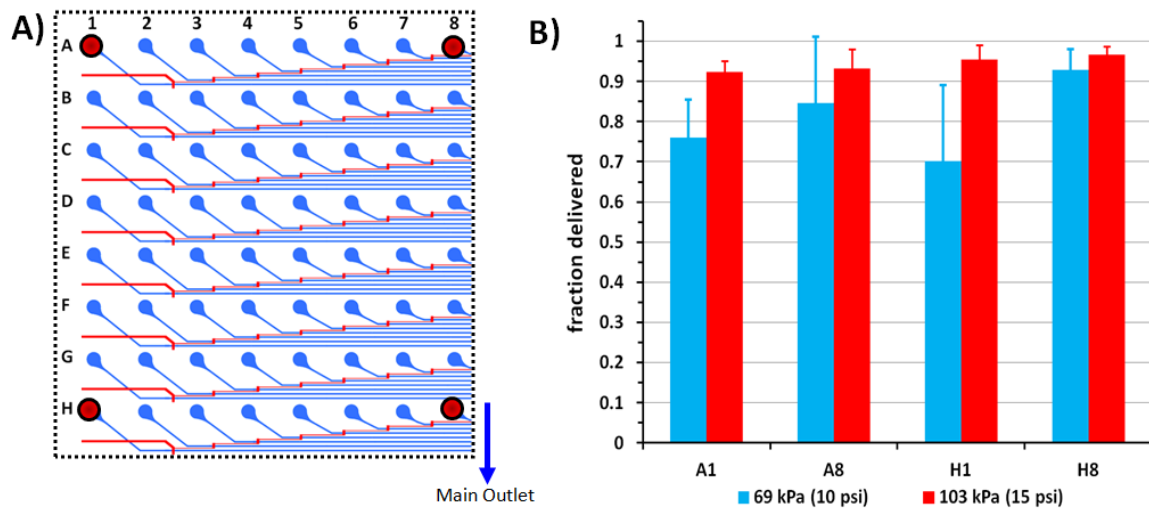


Figure 4.9: Worm population delivery rates for four representative wells in the device.

A) The locations of the four wells tested in the device are indicated by red dots in the schematic. B) The fraction of the total initial population in each well delivered during the delivery sequence as function of two operation pressures applied to the well reservoir array through the gasket (n=3).

4.2.7 Experimental validation of population segregation

To confirm that mixing between loaded populations in different wells of the device would not interfere with desired device operation, we conducted a few delivery

sequence experiments with multiple distinct strains loaded into the on-chip wells. We loaded 3 separate populations into the chip in distinct orders along a given row (Fig. 11). The two strain preloading configurations allowed us to confirm whether or not there was cross-mixing of worms between wells in the given row. As mentioned earlier, each row within the device's well plate format reservoir array has the same motif of eight well channels with flow regulated by seven multiplexed valves. We surmised that if mixing between the wells within a single row in the array were eliminated, particularly the row closest (row *H*) and the row farthest from the chip exit (row *A*), we could sufficiently rule out mixing between wells of any of the rows as a proof of concept. These rows contain the two extremes for two key worm delivery parameters: flow rates coming from wells within a given array column and the distance the worm populations must travel to reach the exit. Worms from wells in row *A* will be the least likely to reach the exit of the chip and be cleared from the main channel between deliveries from each well in the sequence with the optimized timing and pressure parameters.

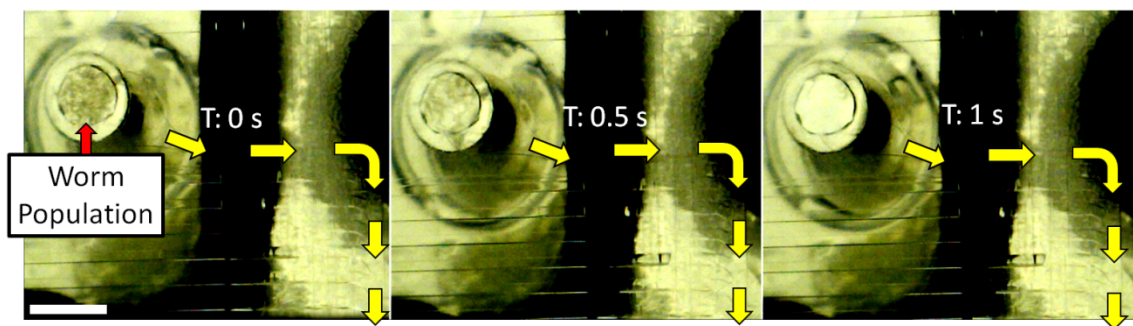


Figure 4.10: Ultrafast worm population delivery.

At time 0 worms have sunk to the interface of the well plate reservoir and the well channel. Delivery commences and after one second the well is essentially empty. Scale bar is ~3mm.

We loaded and delivered 3 different strains in sequence according to the configurations outlined in Figure 4.11. The figure shows a mixing truth table for the two configurations. Looking at a single well loading configuration, when a given strain is loaded into a subset of wells in the row, mixing between a given well of interest and wells that were preloaded with the same strain cannot be ruled out during the delivery sequence, even if the device is functioning properly. However, mixing between wells with different strains is easily confirmed, as indicated by the green mixing candidates. In Figure 4.11d, the two loading configurations are compared and by overlapping their truth tables it is evident that all cases of mixing between wells in the rows are ruled out as long as only the strain preloaded in a given well is collected during the delivery sequence.

We ran the sequence as outlined in Figure 4.11c at ~ 103 kPa (15 psi) applied at the gasket. We preloaded ~ 100 worms for each strain according to the configurations outlined in Figure 4.11a, as well as 4.11b and ran each case 3 times. In 91 out of 96 population deliveries from individual wells, we observed zero cross-contamination of the wrong strain in a given well. In the five cases that we observed any mixing, the contaminating worms comprised on average $<1.9\% \pm 0.6$ of the total population delivered.

We also performed additional experiments to confirm that animals from row *A* were not contaminating animals from row *H*, since all wells belonging to the same column had the same strain pre-loaded into them during the experiments outlined in Figure 4.11 (e.g. well *A3* and well *H3* have the same strain). We pre-loaded a distinct

strain in all wells in row *A* and pre-loaded a different strain in the wells of row *H* and validated that there was no cross-contamination between the two rows during the delivery sequence.

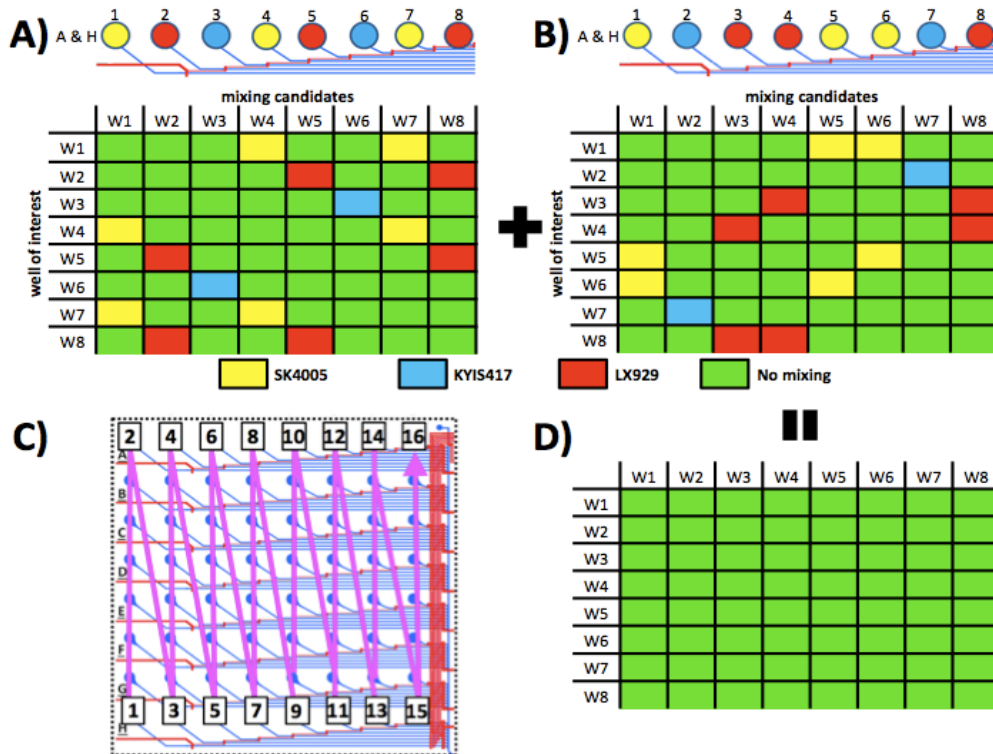


Figure 4.11: Strain mixing experimental design.

A) (TOP) The first configuration of worm strains preloaded into the wells of rows *A* and *H* before initiating the delivery sequence. (BOTTOM) A truth table for mixing events between given wells of interest and all other wells in the given row that cannot be logically eliminated in the given configuration. The color-coded worm strain name key is also shown. B) The second preloaded configuration of worm strains and corresponding population mixing truth table. C) The sequence order of well populations delivered during experiments to confirm elimination of cross-contamination between wells within rows of the device's well plate reservoir array. D) Overlapping the green squares (confirmed non-mixing cases) of the truth tables for both worm strain preloading configurations in the worm mixing experiments indicates that validating both cases will confirm that no mixing occurs within the given rows.

We confirmed the near elimination of cross-contamination between wells in the rows that were located at the device's two extremes in terms distance from the main exit. Additional optimization of the delivery sequence should bring cross-mixing down to even more negligible levels, particularly increasing the duration of Step 2 by 0.1-0.5 sec when the *Main Channel* is being cleared of potential contaminating worms.

4.3. MATERIALS AND METHODS

All methods related to worm maintenance, handling, and preparation for loading into the device are outlined in chapter 3. Techniques for measuring fluid flow rates on-chip are also described in that chapter.

4.3.1. Device fabrication

As previously described, the microfluidic chip was fabricated using multilayered soft-lithography via techniques similar to methods established for the 16-well device. In this case, the device molds were patterned on six-inch wafers as opposed to four inch wafers due to the larger device area. Using the fabrication methods described in Chapter 3, a control layer mold consisting of negative resist was patterned on one wafer and a flow layer mold consisting of negative and positive resist was patterned on the second wafer. The control layer thickness in this case was $\sim 45 \mu\text{m}$ and the flow layer thickness was $\sim 110 \mu\text{m}$.

To create the 64 well plate-format reservoirs in the flow layer mold, first an 8x8 well section was cut from a conical 96-well PCR plate (Eppendorf Corp.) using a band saw. This piece was then cleaned by submersion in isopropyl alcohol and air-dried prior to applying 50 μL of PDMS (10:1, elastomer: base agent) to the outer tip of each conical

reservoir in the plate section. With the flow layer mold situated on a level hot plate, the PCR plate section was placed such that its conical wells sat on and aligned with the flow layer mold's population input ports (Fig. 4.2b). We turned on the hot plate and set it to 75° C to cure the PDMS on the tips of conical wells and fix the PCR plate piece's location on the mold. After placing an acrylic barrier on top of the flow layer wafer mold, we poured 90 grams of uncured PDMS (10:1, base agent: curing agent) inside the perimeter of the barrier (Fig. 4.2c). We placed these components in an oven at 72.5° C for 3 hours to cure the PDMS.

We then bonded the large area device to its control layer via previously-described oxygen plasma treatment method. Due to the device's large area, optical alignment tools were now necessary to properly position the flow layer relative to the control layer. Using two stereoscopes, we confirmed the correct positioning of alignment markers on opposite sides of the device before making the permanent bonding contact. Then we performed a baking step, followed by bonding the device to 3mm thick piece of custom-cut borosilicate glass.

4.3.2 Gasket system fabrication

All components of the gasket system (Fig. 4.3) were machined via CNC or manual milling. The parts were fabricated so that the entire gasket system fit the footprint of standard well plates. We machined a 12.5 mm thick acrylic part to have multiple 2 mm x 1 mm cross-section channels that terminated with 3mm wide circular openings (Fig. 4.4a). We then machined a 3 mm thick acrylic part to fit flush against the larger piece just described and drilled several 3 mm holes into it, such that the holes completely

overlapped with the openings on the thicker acrylic part (Fig. 4.4a). We then sandwiched both parts between two 7 x 7 inch borosilicate glass sheets that were held in place by tightened screw clamps, and placed these components in an oven at 70° C for 30 min, followed by another 30 min bake at 145° C. We then placed the components back into 70° C for 30 more minutes and finally let them cool down to room temperature [71].

The channels machined into the thick acrylic part were now sealed from the external environment except at the circular openings that overlapped with the equivalent features in the thinner part. We then machined grooves around the entire circumference of each pneumatic output orifice and secured rubber O-rings (Danco Inc.) into the inner edges of the grooves (Fig 4.4b-c).

The pneumatic entrances for each air-input channel were machined into two of the short sides of the gasket (Fig 4.3b, 4.4a). A 5mm x 5mm step was then machined on the top-side of the gasket for alignment of the gasket clamp (Fig 4.3a). 17 gauge metallic couplers were then secured into these holes with adhesive for coupling to solenoid valves (Fig. 4.3b). Holes were then drilled through the entire thickness of the gasket where tubing from the flush lines would interface the microfluidic chip.

The gasket clamp was machined out of aluminum (a 12.5 mm thick piece and a 6.3 mm thick piece) (Fig. 4.3). Holes with screw threads were then drilled into the center of each of the four sides of the rectangular aluminum components of the clamp. Four twist latches (Fastenal Inc.) were secured to the perimeter of top aluminum part with screws. Corresponding latch hooks were screwed onto the four sides of the bottom aluminum piece of the gasket clamp, which would sit below the chip and the gasket.

4.3.3 Automation software and hardware control

A set of twenty-one solenoid valves controlled by a custom automation program written in LabVIEW regulated fluid flow in the multiplexer device by coupling pressurized fluid and air to the pneumatic inputs inside the gasket. Computer-controlled pressure regulators (QPV1, Proportion Air Inc.) controlled the dynamic pressure applied to the well plate format reservoir array and the *Main Channel Flush*'s fluid reservoir.

4.3.4 Device operation: priming, animal loading, and sequence initiation

Tubing inputs for the *Exit Flush*, *Main Channel Flush*, and *Main Exit* (Fig. 4.1b) were plugged into the device via 22 gauge metal couplers (Instech Solomon). $\sim 20 \mu\text{L}$ of filtered dionized water was loaded into each of the on-chip pneumatic microfluidic valve reservoirs (Fig. 4.1c, 4.4c). The chip and the acrylic gasket were then sandwiched and clamped together within the gasket clamp. 207 kPa (30 psi) was then delivered to each on-chip valve input via the gasket to fill the valve channels with DI water. After priming the valves, the *Exit Flush* delivered filtered M9 solution to the device to fill it with fluid and remove air bubbles. Valves one through eight (VI-V8, Fig. 4.1c) were then closed and $\sim 70\text{-}105$ kPa ($\sim 10\text{-}15$ psi) was applied to the on-chip well plate reservoir array and the fluid coming into the chip via the *Exit Flush* input. The closed valves served as dead ends for fluid flow so that the pressurized fluid would force any air bubbles in the microchannels to diffuse through the bulk PDMS.

To load animals onto the chip after priming, a stand-alone pneumatic source, such as a syringe coupled to the "all-stop-valve" input (Fig. 4.1a) was pressurized to block flow out of the wells. After removing the chip from the gasket system, $\sim 100\text{-}150$ worms

were then loaded via micropipette (P-200) coupled maximum recovery pipette tips into the desired wells and allowed to sink to the well bottoms (~5 min). Meanwhile, the chip was returned to the gasket system, and the on-chip valves were then pneumatically closed. At this point, the "all-stop-valve" was opened and the delivery sequence could commence.

4.4 CONCLUSIONS

We designed, fabricated, and characterized a microfluidic multiplexer platform for ultra-fast delivery of *C. elegans* populations to optical interrogation systems. The modular system consisted of a microfluidic chip with 64 wells for housing the distinct sample populations, and this chip interfaces with a novel gasket system that delivers pneumatic input to the on-chip valves and well plate format reservoirs. An "all-stop" valve that can be actuated without external pressurized input, blocks flow out of each population-housing reservoir, enabling sample loading at any location, and increases the chip's amenability with automated liquid handling systems.

The 64-well platform greatly improved upon the performance of the 16-well device in terms delivery efficiency and timing. We demonstrated that all wells in the device should be able to deliver at least 92% of their preloaded population in fewer than 3 seconds, as opposed to the minimum of 80% in less than 4.7 seconds on the 16-well platform. This improvement in delivery consistency and efficiency could further reduce the time needed to perform larger high-throughput screens. Furthermore, improving the sealing capabilities of multiplexed valves to avoid the cross-talk observed between wells at 20 psi applied at the gasket would further improve delivery efficiency. Increasing the

length of the overlap regions between *Valves 1-14* and the semicircular channels in the flow layer could improve the valves' sealing capabilities.

Increasing the duration of Steps 2 and/or 3 in the delivery sequence will most likely eliminate the negligible cross-contamination events observed during the population segregation validation experiments. Additionally, the higher applied pressures at the gasket enabled by improved valve sealing will lead to faster delivery during Step 1 of the sequence and decrease the likelihood that worms remain in the main channel.

CHAPTER FIVE: NOVEL PARALLELIZED MICROFLUIDIC DEVICES FOR *C. ELEGANS* NERVE REGENERATION STUDIES

In this chapter we present a novel microfluidic optical interrogation platform for studying neuroregenerative phenomena in *C. elegans*. The microfluidic chip consists of an array of microchannels arranged in parallel to trap many individual worms for precise nanoaxotomy and imaging of nerve regeneration. The device is the culmination of four device iterations in which we optimized the efficiency of filling each trap with a single worm, immobilization of the animals during imaging, and the housing and tracking of the worms over multiple time points during the course of axonal regeneration. In the workflow of an automated screen, this device could be placed downstream of the population delivery platforms discussed in the previous chapters or work as a stand-alone system.

5.1 OVERVIEW

In this chapter, we describe four iterations of a parallelized microfluidic device concept for trapping, housing, imaging, and performing axotomy on *C. elegans*. These devices were built to increase the number of axotomies and images one could acquire in a given amount of time by trapping and housing many worms simultaneously for nerve regeneration studies. We discuss how we attempted to integrate knowledge from each generation to improve overall functionality of subsequent designs. Key aspects of proper device operation were the percentage of traps that filled with single worms, the ability to immobilize worms for optical studies, and the long term animal storage capability for observations at different time points.

All devices were fabricated using standard soft-lithography methods for producing PDMS microfluidic devices. Our first design was the single-layer parallel trap device, which established a method for delivering multiple worms in unison to individual traps, which were essentially channels that gradually tapered in width [32]. We then fabricated the first version of the membrane immobilization parallel trap device, which circumvented the need to pressurize worms in tapering channels for immobilization by housing worms beneath deformable membranes.

Finally, we made a second version of the membrane immobilization device, in which we improved the deformable membrane function by having even wider trapping channels. It was also outfitted with a nutrient perfusion channel to improve animal viability during long-term on-chip studies. Unfortunately, these perfusion channels had deleterious effects on parallel worm trapping efficiency. However, we were still capable

of performing preliminary nerve regeneration studies on the PQR (oxygen-sensing) neuron with relative ease on this design. Overall, each device had a number of advantages and disadvantages as platforms for efficient trapping of multiple worms, long-term animal storage, and high-throughput imaging and nanosurgery. These preliminary developments finally led to a fourth generation high-throughput microfluidic *C. elegans* nanoaxotomy platform. This final device attempted to capitalize on the advantages of the previous three devices to maximize capabilities in all the key functional areas relevant to performing long term axotomy studies on multiple worms in parallel.

5.2 PRELIMINARY WORK

5.2.1 Parallel trapping microfluidic devices

We initially developed three microfluidic chip prototypes to make a device capable of trapping large numbers of worms simultaneously in separate trapping chambers for live imaging and laser nanoaxotomy. The rationale behind the designs presented was to place several channels leading to trapping chambers in parallel relative to in-coming flow such that a population of worms initially loaded into the device would eventually fill each chamber with a single worm. The device would then allow the experimenter to perform the following steps on each worm in one device: 1. femtosecond laser nanoaxotomy, 2. high-resolution imaging of nerve cells and axons, 3. long-term housing of *C. elegans* worms between each experimental perturbation or time point.

Such a device would allow the experimenter to immobilize and interrogate several worms for multiple days without using anesthetics, microbeads, or adhesives. The animals would be free to move in their individual chambers until optical observation or

manipulation necessitated a short-term immobilization period. Nutrient-infused liquid media loaded in the chip would maintain the animals' viability throughout the experiments.

We evaluated each device iteration based on three main criteria: 1. capacity to fill all of their traps with a single animal efficiently, 2. the immobilization mechanism's ability to allow for sufficient neuronal imaging, 3. the feasibility of performing laser axotomy on worms in the platform.

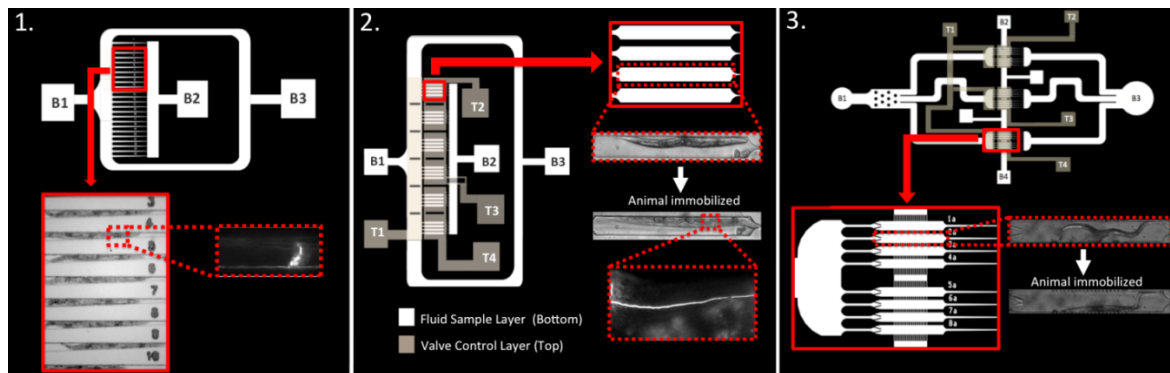


Figure 5.1: Three consecutive design iterations of parallel trap devices for housing, immobilization, and optical interrogation of *C. elegans* worms.

5.2.1.1 Design #1: Microfluidic single-layer parallel trap device

The first device developed and tested (Fig. 5.1, design #1) consisted of multiple tapering trap channels arranged in parallel such that each trap received a single worm from an initially loaded population at the device inlet. Each tapering channel had an entrance that was 50 μm in diameter and linearly decreased over a length of 1000 μm to an exit that was 10 μm in diameter. Since L4 stage *C. elegans* worms are $\sim 30 \mu\text{m}$ wide

on their short body axis and $<700\ \mu\text{m}$ long on their large body axis, those channel dimensions easily allowed the L4 animals to enter the traps without escaping through the tapering exit. Having the trap channel's length less than twice the length of a single animal's long body axis was meant to prevent multiple worms from entering a single trap.

The close proximity of the traps to the population inlet resulted in filling nearly 100% of the traps very quickly ($<30\ \text{sec}$), and the trap channel dimensions allowed only a single worm to enter the trap a vast majority of the time. However, immobilization by constantly applying pressure to the inlet to push worms was not ideal for high-resolution imaging and axotomy. The axons of most neurons-of-interest studied in *C. elegans* nerve regeneration studies must be as close as possible to the cover glass for optimal ablation and imaging. However, the traps in this iteration of the device generally orientated the worms' bodies such that these neurons were rotated up to 90° from the optimal position. Worms often also escaped their traps if pressure at the inlet was lost, and the animals were also too motile in these trap channels to perform precise axotomies on their neurons.

5.2.1.2 Design #2: Membrane immobilization parallel trap device (Version 1)

In order to circumvent the issues derived from the previous device's immobilization mechanism, we made a second iteration of the parallel trap device (Fig. 5.1, design #2). In this chip, the trapping chambers utilized the membrane valve-based immobilization method used in our lab's previous work [35]. We changed the trap channel widths to allow the immobilization membrane to deflect downward ($100\ \mu\text{m}$) and linked them to a downstream tapering channel similar to the previous design. These

tapering channels were much shorter and had a much steeper tapering angle until they reached the 10 μm channel width to prevent worm escape. The steeper tapering angle allowed less than $\sim 25\%$ of the animal's body to enter the tapering channel, which positioned the majority of its body under the membrane. We also placed an additional membrane valve just upstream of parallel traps to block the trap channel openings after loading worms into the device. This valve would prevent the animals from escaping the traps over long time periods between full immobilization.

We were able to house the worms for over 24 hrs in the device trap channels with no drop off in viability. The valve upstream of the traps prevented animals from escaping during this time period, as long as there was no pressure leakage at the valve's on-chip pneumatic input port. During immobilization, the membrane valves above the trap channels usually guided the animals to an orientation that allowed for optimal imaging and laser axotomy conditions. However, if the immobilization valve membrane thickness was too high or the worm in a given trap was larger than expected, animal motility would decrease the likelihood of having the desired optical access. Additionally, animal population loading efficiency and performance dropped relative to the previous design, as not all traps would receive a worm, while other traps would fill with multiple worms. The wider trap channel had enough area for multiple worms, and the redesigned tapering channel allowed for less surface area of the worm's body to be flush against its sidewalls and block flow into the trap channel. These factors led to filling or overfilling of trap channels closest to the population inlet, while traps in the periphery of the parallel trap array remained empty.

5.2.1.3 Design #3: Membrane immobilization parallel trap device (Version 2)

In the third iteration of this design (Fig. 5.1, design #3), we made the following major revisions to improve device function: 1. Widen the trap channels for increased membrane deflection during immobilization, 2. Place the trap channels equidistant from the population inlet to encourage loading of all traps, 3. Place a passive one-way stop valve at the trap channel entrances to negate the need for a membrane valve to confine the animals in the traps between membrane immobilization, and 4. Adjust the tapering channel angle to increase flow blockage into the trap channel once an animal is stuck in the tapering channel. We also included a perfusion channel to run nutrients across all of the traps.

The increased trap channel width improved immobilization and allowed for facile imaging and axotomy in the device. The one-way stop valves at the trap channel entrances prevented worms from escaping during a 24 hr period in a vast majority (~90%) of the traps tested. One disadvantage we noticed was that the wider trap channels allowed animals to orient somewhat randomly in the channel such that their entire bodies were not always flush against one side wall of the trap chamber (Fig. 5.1, design #3). In many cases the actuated membrane valve would crush their bodies during immobilization due to these unfavorable orientations, leading to decreased viability after the valve was released. The perfusion channel design also introduced unintended flow paths into the trap channels, such that despite the improved flow blockage into tapered channels, multiple animals could still enter a given trap.

5.2.2 Preliminary nerve regeneration studies in the PQR neuron

Our preliminary studies indicate that fs-laser axotomy to the axon process of the PQR neuron yielded 100% regrowth along the previously established axonal trajectory 24 hours post laser cutting. Additionally, cuts to the dendrite process yielded 50% regrowth after 24 hrs. However, simultaneous cuts to both processes in the same neuron yielded 100% regrowth in both processes, suggesting that regenerative cues are more active after cuts to the axon and these regenerative factors can increase the regenerative capacity of the dendrite. Since the process that grows anteriorly (axon) has a higher regenerative capacity, genes that specify the directions of axon and dendrite growth could be implicated in regeneration of PQR.

Further studies with mutations in the WNT/Frizzled pathway could help understand if these genes play a role in regeneration, as they were previously implicated in neuronal development defects in the ALM, PLM, and PQR neurons [66, 67]. Since for example, mutations to the WNT ligand, *lin-44* can cause the dendrite of the PQR neuron to grow anteriorly instead of towards the posterior, defining the roles of such extracellular cues in regeneration could provide novel insights into regrowth and reconnection mechanisms [67].

To facilitate nerve regeneration studies in *C. elegans*, we developed fourth generation microfluidic parallel trapping device for the housing and immobilization of worms during neuroimaging and laser-guided nanoaxotomy. The device consisted of several immobilization chambers arranged in parallel to receive individual worms from a

population loaded on-chip, house the animals, and immobilize them during optical interrogation and nanoaxotomy.

5.3 DESIGN AND TESTING

Based on our previous work with parallel trap devices (Figure 5.1), the fourth generation platform combined the best features of the three previous designs, as well as novel approaches to achieve optimal function. Mainly, this design was meant to facilitate filling all, or a vast majority, of its immobilization chambers and properly orienting and immobilizing these animals during imaging and nanoaxotomy.

The new design featured a set of parallel staging traps upstream of a set of parallel immobilization traps. The staging traps were very similar in design and function to the immobilization channels in the first version of the parallel trap device (Fig. 5.1, design #1). Like this previous parallel trap device, the staging area consisted of short tapering channels that are slightly longer than the average L4 worm (Fig. 5.2b). They are situated within millimeters of the device's entrance for the worm population to ensure fast and complete trap filling. Instead of tapering down to a width that prevents worms from moving further, the ends of the traps were blocked by a partially sealing membrane valve (Fig. 5.2b). Once all of the traps are filled with a worm, the valve opens and flow directs the worms to the downstream immobilization traps (Fig 5.3).

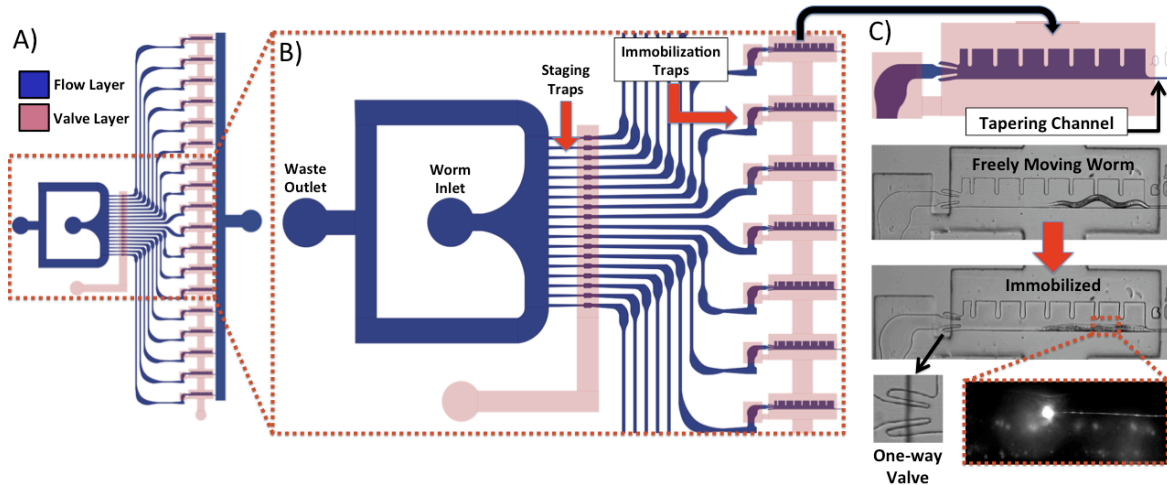


Figure 5.2: Fourth generation parallel trap device for imaging, housing, and axotomy.

A) A schematic of the two layer device with the flow layer and valve control layer labeled. B) A worm population will arrive via the worm inlet, get trapped in the staging traps, and then be transported to the immobilization traps. C) An individual immobilization trap for housing and immobilizing individual *C. elegans*.

The immobilization traps are wider channels that terminate into a tapering channel that will prevent the animals from passing through (Fig. 5.2c). Above these traps resides a deformable membrane that deflects toward the channel floor when pressurized to immobilize the animal against one of the channel walls and the cover glass. Multiple protrusions will extend from the channel wall opposite of the sidewall that the worm rests against during immobilization (Figure 5.2c, 5.4). These restrictions keep the animal in a repeatedly optimal orientation for imaging and nanoaxotomy by ensuring the animal's entire body is resting against one sidewall of the immobilization trap when the membrane is pressurized. This orientation ensures that the worm's body is not unfavorably crushed by the immobilization membrane, which occurred in design 3 of the previous device

iterations (Fig. 5.1, #3). Another set of protrusions (one-way valves) at the entrance of the immobilization traps are orientated such that animals can easily enter the traps initially but cannot easily exit them between immobilization steps (Fig. 5.2c).

5.3.1 Device design rationale

The device was tested in regards to its ability to fill each of its traps with a single worm and immobilize those worms in a manner conducive to easy imaging and axotomy of the neuron of interest; specifically maintaining the worm's body in a straight orientation and minimizing body movements during optical interrogation. It was important to have a single worm in each trap so that axon injuries and subsequent recovery at different time points could be tracked in single organisms in a high throughput manner.

5.3.2 Trap filling

A key component of the device's success was its ability to fill each trap with a single worm. Initially after delivering worms to the device entrance, each staging trap needed to house a single worm before sending worms to the individual immobilization traps (Fig. 5.2c). Success in this step of device operation depended on the staging traps' channel dimensions and actuation scheme (valves and fluid reservoirs) (Fig. 5.3). The channels allowed space for staging a single worm per trap, and during delivery to the immobilization traps; actuation of the valves and pressurized fluid needed to allow for the worms go past the valve, closing soon enough to block additional worms. Other factors affecting trap filling were flow resistance throughout the chip and valve design.

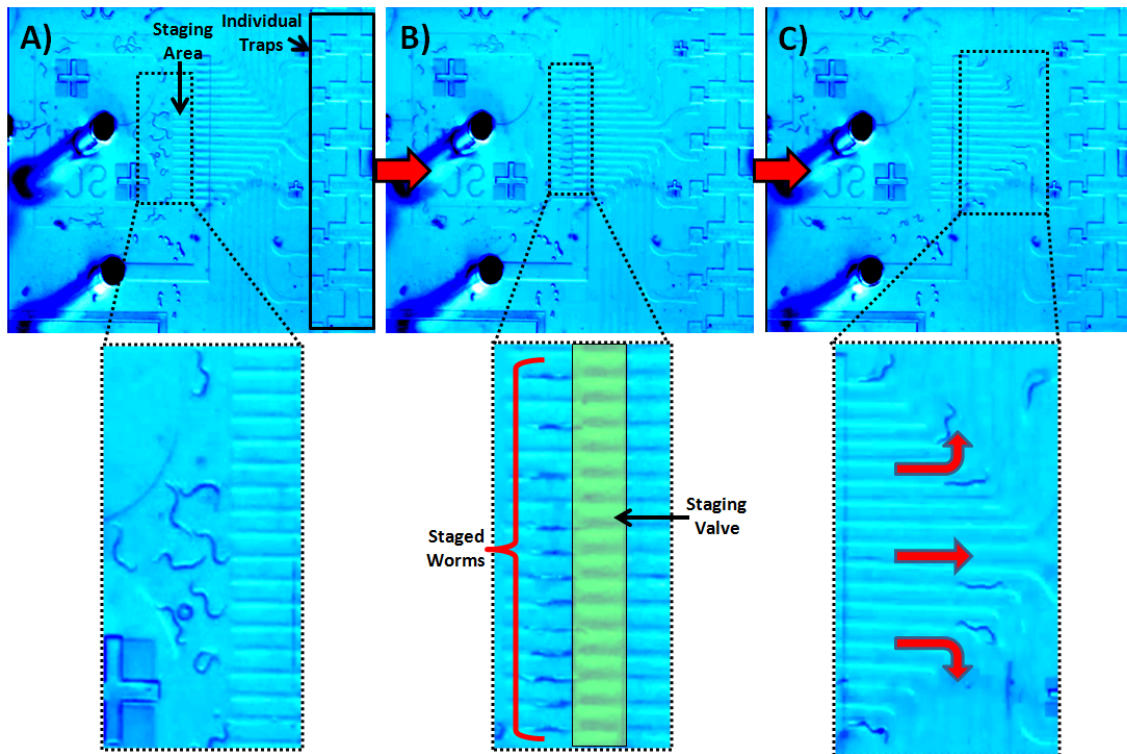


Figure 5.3: Loading sequence for the fourth generation parallel trap device.

A) Freely moving worms enter the chip. B) The flow at the entrance forces the worms into the tapering channels in the staging area, which is partially blocked off with the staging valve. C) The staging valve is released and the individual worms travel to the individual traps.

5.3.3 Immobilization chambers

Successful immobilization will depend on an individual trap's ability to decrease animal motility sufficiently for sub-micron resolution imaging and laser nanoaxotomy. Design #3 from our preliminary work had wide enough channels for sufficient immobilization but often oriented the worm body unpredictably (Fig. 5.1). We integrated posts into the latest version of the device to ensure the worm body is repeatedly positioned during immobilization as shown in Figure 5.4. The trap design had

several individual features that could be parametrically studied and optimized to reach the functional goals of the device. The post width and length needed to keep the worm against a single channel wall, while the spacing between the posts and the width of the posts were meant to allow for enough deflection of the immobilization membrane to optimally minimize animal motility.

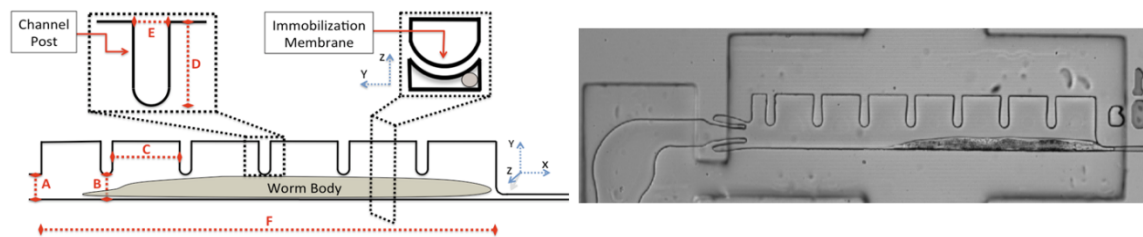


Figure 5.4: Immobilization trap design variables.

The dimensions of the immobilization trap components, which can be optimized to achieve proper function are labeled with red letters. Also included are a schematic of the immobilization valve cross-section and an image of the actual device with an immobilized worm.

5.4 CONCLUSIONS

Further optimization and testing of the parallel trap device based on individual trap design and overall device function will allow for higher throughput time lapse and multiple time point imaging studies on neuroregenerative phenomena. Expansion of the device to include multiple columns of immobilization chambers will allow the simultaneous investigation of several mutant strains. Integration with automated axotomy and imaging systems that also actuate on-chip valves at precise moments for limited durations will generate repeatable datasets of individual worms regenerating their axons, which have been tracked and imaged throughout the process of nanoaxotomy and

regeneration. This approach will yield detailed and quantitative analysis of these biological phenomena in vivo at speeds and scales not yet achieved in a research setting.

CHAPTER SIX: CONCLUSIONS AND FUTURE DIRECTIONS

Here we described the development of multiple microfluidic platforms with the purpose of enhancing and automating microscopy-based studies with *C. elegans*, particularly for gaining a deeper understanding of neurodegenerative and neuroregenerative phenomena. *C. elegans* provides the ideal characteristics for high-throughput manipulation in automated fluidic systems and is amenable to a vast array of imaging techniques and optical tools, including femtosecond laser nanosurgery.

This knowledge has led a vast array of microfluidic tools to enhance high-throughput biology with *C. elegans* as a model organism. We have described a few new platforms that build upon the concept of fast transport and optical interrogation of *C. elegans* worms in a manner that is conducive to systems built for large scale, high-content screening.

We developed and tested two iterations of a two-layer microfluidic multiplexer for fast delivery of *C. elegans* populations to imaging systems. The first system established the paradigm of integrating multiwell format reservoirs into a two-layer microfluidic device and could achieve delivery of entire populations of *C. elegans* at speeds that were an order of magnitude faster than commercial systems designed for similar applications. The 16-well chip system did not harm animal viability, kept the populations separate, and was easily integrated with other platforms, such as microfluidic imaging devices. While the well plate-format reservoirs built into the chip were amenable to automated and liquid handing systems, the chip needed to be coupled to semi-permanent pneumatic connections to function properly.

We expanded on this device concept by building a 64-well device that fit into a typical well plate format footprint. The microfluidic chip in this system could be loaded with populations in any location without the need for semi-permanent pressurized connections because its pneumatic inputs interfaced with a novel gasket system that made the entire system behave as a plug and play platform. The microchannel architecture and custom automation software cut the delivery time by more than two seconds per population relative to the 16-well platform, and delivery rates for entire populations from given wells in the device were much higher and more consistent.

Future work with this platform will include coupling it to other microfluidic imaging platforms for high-throughput imaging studies of worm strains expressing genes relevant to human neurodegenerative diseases, such Alzheimer's and Huntington's disease. These genes can cause neuronal cell death or increase protein aggregate formation during the aging processes and these changes can be quantified with certain imaging techniques in a high-throughput manner. Understanding these phenomena and how to perturb them will result in new insights on treating such diseases.

Finally, we discussed the development one such downstream optical interrogation device, a parallel trap microfluidic immobilization chip for performing time-lapse studies of nerve regeneration in response to femtosecond laser-mediated axotomy. The work on this platform culminated in a fourth generation device that built upon three previous device iterations to efficiently trap, immobilize, and house multiple *C. elegans* worms over the course of hours or days. This tool could be further optimized to reach the desired operational milestones and will hopefully be used to study the effects of the

WNT/Frizzled development pathway on nerve regeneration in the PQR neuron's axon and dendrite processes.

REFERENCES

- [1] Insel TR (2008) Assessing the economic costs of serious mental illness. *Am J Psych* 165: 663–665.
- [2] Kessler RC, Heeringa S, Lakoma MD, Petukhova M, Rupp AE, Schoenbaum M, Wang PS, et al (2008) Individual and societal effects of mental disorders on earnings in the United States: results from the national comorbidity survey replication. *Am J Psych*, 165: 703–711.
- [3] Ben-Yakar A, Chronis N, Lu H (2009) Microfluidics for the analysis of behavior, nerve regeneration, and neural cell biology in *C. elegans*. *Curr Opin Neuro*, 19: 561–567.
- [4] Horner PJ, Gage FH (2000) Regenerating the damaged central nervous system. *Nature* 407: 963-970.
- [5] Kerschensteiner M, Schwab ME, Lichtman JW, Misgeld T (2005) In vivo imaging of axonal degeneration and regeneration in the injured spinal cord. *Nat Med* 11: 572-577.
- [6] Bhatt DH, Otto SJ, Depoister B, Fetcho JR (2004) Cyclic AMP-induced repair of zebrafish spinal circuits. *Science* 305: 254-258.
- [7] Breslauer DN, Lee PJ, Lee LP (2006) Microfluidics-based systems biology. *Mol Biosys*, 2: 97-112.
- [8] Melin J, Quake SR (2007) Microfluidic large-scale integration: the evolution of design rules for biological automation. *Ann Rev Biophys Biomol Struc* 36: 213-231.
- [9] Kaletta T, Hengartner MO (2006) Finding function in novel targets: *C. elegans* as a model organism. *Nat Rev Drug Disc* 5: 387-398.
- [10] Ellerbrock BR, Coscarelli EM, Gurney ME, Geary TG (2004) Screening for presenilin inhibitors using the free-living nematode, *Caenorhabditis elegans*. *J Biomol Screen*,9: 147-152.
- [11] Jones AK, Buckingham SD, Sattelle DB (2005) Chemistry-to-gene screens in *Caenorhabditis elegans*. *Nat Rev Drug Disc*, 4: 321-330.

- [12] Van Ham TJ, Breitling R, Swertz, MA, Nollen EA (2009) Neurodegenerative diseases: lessons from genome-wide screens in small model organisms. *EMBO Molecular Medicine* 1: 360-370.
- [13] Brinkman R R, Mezei MM, Theilmann J, Almqvist E, Hayden M R (1997) The likelihood of being affected with Huntington disease by a particular age, for a specific CAG size. *Am J Hum Gen* 60:1202–1210.
- [14] Morley JF, Brignull HR, Weyers JJ, Morimoto RI (2002) The threshold for polyglutamine-expansion protein aggregation and cellular toxicity is dynamic and influenced by aging in *Caenorhabditis elegans*. *Proc Natl Acad Sci USA* 99: 10417-10422.
- [15] Yanik MF, Cinar H, Cinar HN, Chisholm AD, Jin Y, Ben-Yakar A (2004) Neurosurgery: functional regeneration after laser axotomy. *Nature* 432: 822.
- [16] Wu Z, Ghosh-Roy A, Yanik MF, Zhang JZ, Jin Y, Chisholm AD (2007) *Caenorhabditis elegans* neuronal regeneration is influenced by life stage, ephrin signaling, and synaptic branching. *Proc Natl Acad Sci USA* 104: 15132-7.
- [17] Gabel CV, Antoine F, Chuang C, Samuel AD, Chang C (2008) Distinct cellular and molecular mechanisms mediate initial axon development and adult-stage axon regeneration in *C. elegans*. *Develop* 135: 3623-3623.
- [18] Hammarlund M, Nix P, Hauth L, Jorgensen EM, Bastiani M (2009) Axon regeneration requires a conserved MAP kinase pathway. *Science* 323: 802-806.
- [19] Yan D, Wu Z, Chisholm AD, Jin Y (2009) The DLK-1 kinase promotes mRNA stability and local translation in *C. elegans* synapses and axon regeneration. *Cell* 138: 1005-1018.
- [20] Han M (2010) Advancing biology with a growing worm field. *Develop Dyn* 239: 1263–1264.
- [21] Riddle D, Blumenthal T, Meyer B, Priess J (1997) *C elegans* II. New York, NY: Cold Spring Harbor Laboratory Press.
- [22] Chan MS (1997) The global burden of intestinal nematode infections — fifty years on. *Parasitol Today* 13: 438–443.
- [23] Qin J, Wheeler AR (2007) Maze exploration and learning in *C. elegans*. *Lab Chip* 7: 186–92.

- [24] Chronis N, Zimmer M, & Bargmann, CI (2007) Microfluidics for *in vivo* imaging of neuronal and behavioral activity in *Caenorhabditis elegans*. *Nat Methods*, 4: 727–731.
- [25] Pulak R, Kalutkiewicz P, Ferrante A, O’Connor G, Kean J, Clover R (2001) Fully Automated Instrumentation for Analysis in *C. elegans*. International *C. elegans* Meeting.
- [26] Suiban B, Belougne J, Ewbank J, Zugasti O (2012) Quantitative and automated high-throughput genome-wide RNAi screens in *C. elegans*. *J Vis Exp* 60.
- [27] Dupuy D, et al. (2007) Genome-scale analysis of *in vivo* spatiotemporal promoter activity in *Caenorhabditis elegans*. *Nat Biotechnol* 25: 663-668.
- [28] R. Pulak, Techniques for Analysis, Sorting, and Dispensing of *C. elegans* on the COPAS™ Flow-Sorting System *Methods in Molecular Biology*, vol. 351: *C. elegans: Methods and Applications*.
- [29] Doitsidou M, Flames N, Lee AC, Boyanov A, Hobert O (2008) Automated screening for mutants affecting dopaminergic-neuron specification in *C. elegans*. *Nat Methods* 5: 869- 872.
- [30] Qin J, Wheeler AR (2007) Maze exploration and learning in *C. elegans*. *Lab Chip* 7: 186–192.
- [31] Chronis N, Zimmer M, Bargmann CI (2007) Microfluidics for *in vivo* imaging of neuronal and behavioral activity in *Caenorhabditis elegans*. *Nat Methods* 4:727–731.
- [32] Hulme SE, Shevkoplyas SS, Apfeld J, Whitesides GM (2007) A microfabricated array of clamps for immobilizing and imaging *C. elegans*. *Lab Chip* 7: 1515–1523.
- [33] Kim N, Dempsey CM, Zoval JV, Sze J-Y, Madou MJ (2007) Automated microfluidic compact disc (CD) cultivation system of *Caenorhabditis elegans*. *Sensor Actuat B-Chem* 122: 511–518.
- [34] Rohde CB, Zeng F, Gonzalez-Rubio R, Angel M, Yanik MF (2007) Microfluidic system for on-chip high-throughput whole-animal sorting and screening at subcellular resolution. *Proc Natl Acad Sci USA* 104: 13891–13895.

- [35] Guo SX, Bourgeois F, Chokshi T, Durr NJ, Hilliard MA, Chronis N, Ben-Yakar A (2008) Femtosecond laser nanoaxotomy lab-on-a-chip for in vivo nerve regeneration studies. *Nat Methods* 5: 531-533.
- [36] Zeng F, Rohde CB, Yanik MF (2008) Sub-cellular precision on-chip small-animal immobilization, multi-photon imaging and femtosecond-laser manipulation. *Lab Chip* 8: 653-656.
- [37] Chung K, Crane MM, Lu H (2008) Automated on-chip rapid microscopy, phenotyping and sorting of *C. elegans*. *Nat Methods* 5: 637-643.
- [38] Chung K, Lu H (2009) Automated high-throughput cell microsurgery on-chip. *Lab Chip* 9: 2764-2766.
- [39] Stirman JN, Brauner M, Gottschalk A, Lu H (2010) High-throughput study of synaptic transmission at the neuromuscular junction enabled by optogenetics and microfluidics. *J Neurosci Methods* 191: 90-93.
- [40] Hulme SE, Shevkoplyas SS, McGuigan AP, Apfeld J, Fontana W, Whitesides GM (2010) Lifespan-on-a-chip: microfluidic chambers for performing lifelong observation of *C. elegans*. *Lab Chip* 10: 589-597.
- [41] Samara C, Rohde CB, Gilleland CL, Norton S, Haggarty SJ, Yanik MF (2010) Large-scale *in vivo* femtosecond laser neurosurgery screen reveals small-molecule enhancer of regeneration. *Proc Natl Acad Sci USA* 107: 18342-18347.
- [42] Gilleland CL, Rohde CB, Zeng F, Yanik MF (2010) Microfluidic immobilization of physiologically active *Caenorhabditis elegans*. *Nat Protoc* 5: 1888-1902.
- [43] Chung K, Zhan M, Srinivasan J, Sternberg PW, Gong E, Schroeder FC, Lu H (2011) Microfluidic chamber arrays for whole-organism behavior-based chemical screening. *Lab Chip* 11: 3689-3697.
- [44] Carr JA, Parashar A, Gibson R, Robertson AP, Martin RJ, Pandey S (2011) A microfluidic platform for high-sensitivity, real-time drug screening on *C. elegans* and parasitic nematodes. *Lab Chip* 11: 2385-2396.
- [45] Cáceres IDC, Valmas N, Hilliard MA, Lu H (2012) Laterally orienting *C. elegans* using geometry at microscale for high-throughput visual screens in neurodegeneration and neuronal development studies. *PloS One* 7: e35037.

- [46] Crane MM, Stirman JN, Ou C, Kurshan PT, Rehg JM, Shen K, Lu H (2012) Autonomous screening of *C. elegans* identifies genes implicated in synaptogenesis. *Nat Methods* 9: 977-980.
- [47] Lockery SR, Hulme SE, Roberts WM, Robinson KJ, Laromaine A, Lindsay TH, Whitesides GM, Weeks JC (2012). A microfluidic device for whole-animal drug screening using electrophysiological measures in the nematode *C. elegans*. *Lab Chip* 12: 2211–2220.
- [48] Whitesides GM, Ostuni E, Takayama S, Jiang X, Ingber DE (2000) Soft lithography in biology and biochemistry. *Annu Rev Biomed Eng* 3: 335-373.
- [49] McDonald JC, Duffy DC, Anderson JR, Chiu DT, Wu H, Schueller OJ, Whitesides GM (2000) Fabrication of microfluidic systems in poly-(dimethylsiloxane). *Electroph* 21: 27-40.
- [50] Unger MA, Chou H, Thorsen T, Scherer A, Quake SR (2000) Monolithic microfabricated valves and pumps by multilayer soft lithography. *Science* 288: 113–116.
- [51] Thorsen T, Maerkl SJ, Quake SR (2002) Microfluidic large-scale integration. *Science* 298: 580–584.
- [52] Hua ZS, Xia YM, Srivannavit O, Rouillard JM, Zhou X, Gao X, Gulari E (2006) A versatile microreactor platform featuring a chemical-resistant microvalve array for addressable multiplex syntheses and assays. *J Micromech Microeng* 16: 1433-1443.
- [53] Melin J, Quake SR (2007) Microfluidic large-scale integration: the evolution of design rules for biological automation. *Annu Rev Biophys Biomol Struct* 36: 213–231.
- [54] Wang J, Sui G, Mocharla VP, Lin RJ, Phelps ME, Kolb HC, Tseng HR (2006) Integrated microfluidics for parallel screening of an in situ click chemistry library. *Angew Chem Int Ed Engl* 118: 5402–5407.
- [55] Gómez-Sjöberg R, Leyrat AA, Pirone DM, Chen CS, Quake SR (2007) Versatile, fully automated, microfluidic cell culture system. *Anal Chem* 79: 8557-8563.
- [56] Singhal A, Haynes C, Hansen CL (2010) Microfluidic measurement of antibody-antigen binding kinetics from low abundance samples and single cells. *Anal Chem* 82: 8671-8679.

- [57] Kirby B (2010) *Micro- and Nanoscale Fluid Mechanics: Transport in Microfluidic Devices*. New York, NY: Cambridge University Press. pp. 60-75.
- [58] Nguyen NT, Wereley ST (2002) *Fundamentals and Applications of Microfluidics*. Boston, MA: Artech House. pp. 35-37.
- [59] Lee PJ, Ghorashian N, Gaige TA, Hung PJ (2007) Microfluidic system for automated cell-based assays. *JALA Charlottesville Va* 12:363-367.
- [60] Conant CG, Schwartz MA, Beecher JE, Rudoff RC, Ionescu-Zanetti C, Nevill JT (2011) Well plate microfluidic system for investigation of dynamic platelet behavior under variable shear loads. *Biotechnol Bioeng*. 108: 2978-87.
- [61] Perry MD, Stuart BC, Banks PS, Feit MD, Yanovsky Y, Rubenchik AM (1999) Ultrashort-pulse laser machining of dielectric materials. *Appl Phys* 85: 6803.
- [62] Berns MW, Wright WH, Steubing RW (1991) *Laser Microbeam as a Tool in Cell Biology*. K.W. Cytology, Academic Press. pp. 1-44.
- [63] Vogel A, Noack J, Hüttman G, Paltauf G (2005) Mechanisms of femtosecond laser nanosurgery of cells and tissues. *App Phys B* 81: 1015-1047.
- [64] Allen PB, Sgro AE, Chao DL, Doepker BE, Edgar JS, Shen K, and Chiu DT (2008) Single-synapse ablation and long-term imaging in live *C. elegans*. *J Neuro Methods* 173: 20-26.
- [65] Coates JC, de Bono M (2002) Antagonistic pathways in neurons exposed to body fluid regulate social feeding in *Caenorhabditis elegans*. *Nature* 419: 925-9.
- [66] Bargmann CI, (2006) Chemosensation in *C. elegans*. *WormBook: the online review of C. elegans biology*. pp. 1-29.
- [67] Hilliard MA, Bargmann CI (2006) Wnt signals and frizzled activity orient anterior-posterior axon outgrowth in *C. elegans*. *Develop Cell* 10: 379–90.
- [68] Kirszenblat L, Pattabiraman D, Hilliard MA (2011) LIN-44/Wnt directs dendrite outgrowth through LIN-17/Frizzled in *C. elegans* neurons. *PLoS Bio* 9: e1001157.
- [69] Johnson TE, Wood WB (1982) Genetic analysis of lifespan in *Caenorhabditis elegans*. *Proc Natl Acad Sci USA* 79: 6603–6607.

- [70] Hardy BS, Uechi K, Zhen J, Pirouz-Kavehpour H (2009) The deformation of flexible PDMS microchannels under a pressure driven flow. *Lab Chip* 9: 935–938.
- [71] Chia-Wen T, DeVoe DL (2009) Bonding of thermoplastic polymer microfluidics. *Microfluid Nanofluid* 6: 1-16.
- [72] Lee SW, Lee SS (2008) Shrinkage ratio of PDMS and its alignment method for the wafer level process. *Microsys Technol* 14: 205-208.